INFORMATION TO USERS

This manuscript has been reproduced from the microfilm master. UMI films the text directly from the original or copy submitted. Thus, some thesis and dissertation copies are in typewriter face, while others may be from any type of computer printer.

The quality of this reproduction is dependent upon the quality of the copy submitted. Broken or indistinct print, colored or poor quality illustrations and photographs, print bleedthrough, substandard margins, and improper alignment can adversely affect reproduction.

In the unlikely event that the author did not send UMI a complete manuscript and there are missing pages, these will be noted. Also, if unauthorized copyright material had to be removed, a note will indicate the deletion.

Oversize materials (e.g., maps, drawings, charts) are reproduced by sectioning the original, beginning at the upper left-hand corner and continuing from left to right in equal sections with small overlaps. Each original is also photographed in one exposure and is included in reduced form at the back of the book.

Photographs included in the original manuscript have been reproduced xerographically in this copy. Higher quality 6" x 9" black and white photographic prints are available for any photographs or illustrations appearing in this copy for an additional charge. Contact UMI directly to order.

UMI

A Bell & Howell Information Company
300 North Zeeb Road, Ann Arbor, MI 48106-1346 USA
313/761-4700 800/521-0600

Reproduced with permission of the copyright owner. Further reproduction prohibited without permission.

MOLECULAR, IONIC AND ELECTRONIC TRANSPORT IN SOLID OXIDE MEMBRANES AND FUEL CELLS

by

HUIMING DENG

A dissertation submitted to the Graduate Faculty in Physics in partial fulfillment of the requirements for the degree of Doctor of Philosophy, The City University of New York

1995

UMI Number: 9605589

UMI Microform 9605589

UMI
300 North Zeeb Road
Ann Arbor, MI 48103

This manuscript has been read and accepted for the Graduate Faculty in Physics in satisfaction of the dissertation requirement for the degree of Doctor of Philosophy.

9/14/95
Date

L. A. Ferrari
Professor L. A. Ferrari
Chair of Examining Committee

9/15/95
Date

Joseph B. Krieger
Professor J. Krieger
Executive Officer

Benjamin Abeles
Dr. B. Abeles

N. Garcia
Professor N. Garcia

Fred H. Pollak
Professor F. H. Pollak

Professor S. A. Schwarz

Supervisory Committee

THE CITY UNIVERSITY OF NEW YORK

Abstract

MOLECULAR, IONIC AND ELECTRONIC TRANSPORT IN SOLID OXIDE MEMBRANES AND FUEL CELLS

by

Huiming Deng

Adviser: Dr. Benjamin Abeles

We solve the transport equations for diffusion-reaction in solid oxide membranes and fuel cells which have a basic structure that consists of a mixed ionic electronic conductor (MIEC) porous anode and cathode separated by a thin dense layer. The large surface area of the porous electrodes enhances the chemical reaction and correspondingly gives rise to an enhanced ionic current. The purpose of the dense layer is to block the direct passage of gas molecules between the electrodes. In the case of a fuel cell this dense layer is an ionic conductor which allows only the passage of oxygen ions while in the case of a membrane the dense layer is a mixed ionic electronic conductor (MIEC) which allows the passage of electrons as well as ions. In an oxygen membrane with electrodes having surface area 100 m^2/gm, an ion current of over two orders of magnitude over that of membrane without porous electrodes, is theoretically achievable. In the case of the fuel cell the corresponding increase in the short circuit current is a factor of 30.

We synthesize thin dense blocking layers, in the range 0.05-1 µm, and nano-scale particles 50-100 Å for the porous electrodes, by pulsed laser deposition of the ionic conductor yttrium stabilized zirconia and the MIEC $SrCo_{0.8}Fe_{0.2}O_{3-\delta}$. X-ray, SEM and TEM microscopy, electrical conductivity and optical transmission measurements were used to characterize the materials. The YSZ electrode interfacial impedance has the constant phase angle form. The conductivity of $SrCo_{0.8}Fe_{0.2}O_{3-\delta}$, is interpreted by a charge transfer conduction process and it has an activation energy of 0.17 eV. The optical absorption spectrum of $SrCo_{0.8}Fe_{0.2}O_{3-\delta}$ is interpreted in terms of an effective one-electron band structure diagram.

Acknowledgment

I wish to acknowledge many people who have helped and encouraged me during my thesis research at Exxon Corporate Research Labs and my graduate course studies at Queens College of the City University of New York.

I owe a great deal of my successful completion of this thesis to my thesis adviser Dr. Benjamin Abeles, a senior research associate at Exxon Research & Engineering Company. I Thank him for the excellent advice and direction he provided me. I have been fortunate to benefit from his many years of experience in research and his physical insight. He worked hard to help me in every aspect of my research work. He is always supportive and encouraging.

Thanks to professor Lawrence A. Ferrari for his supporting my graduate work and research while I was pursuing my degree. He is a demanding teacher and at same time he is always ready to help students with their work.

Thanks to Minyao Zhou and Cheayao Zhang for their help and encouragement in my thesis research.

Thanks to the professors N. Garcia, F. H. Pollak and S. A. Schwarz who served on my supervisory committee. Thanks to all the professors who have taught me, given me advices and help at Queens College of the City University of New York.

Special thanks to my family for their love, care and encouragement.

I wish to acknowledge the financial support from Queens College of the City University of New York and Exxon Research & Engineering Company.

Annandale, NJ
September 1995

TABLE OF CONTENTS

LIST OF FIGURES

Introduction

Oxygen permeating membranes made of mixed ionic electronic conducting oxides (MIEC) are of considerable technological interest in membranes for oxygen separation, for catalytic membrane processes and for fuel cells [1,2]. Oxygen permeation involves a complex interplay between oxygen gas activation at the gas-solid interface and bulk transport of oxygen ions and electrons. The physical and electrochemical mechanism underlying the permeation process are in general not well understood. Figure 1 depicts the basic mechanisms involved in the permeation process for the case of a dense MIEC membrane. Oxygen molecules are electrocatalytically activated and ionized at the high pressure side of the gas-solid interface to doubly charged negative O^{2-} ions:

$$\frac{1}{2}O_2 + 2e \Leftrightarrow O^{2-} .$$

In the process two electrons are extracted from the conduction band producing two positive holes, which together with the ion form a neutral ambipolar pair. The ambipolar pairs, hopping via oxygen vacancies, diffuse to the low pressure side of the membrane. There the reverse process takes place, two electrons are released for each ion and two oxygen atoms recombine at the interface to form a O_2 molecule.

In the application of membranes [3] as chemical reactors or for separation of gases, a critical question is the upper limit of ion current that can be achieved for a given pressure drop across the membrane. The ion current in a dense membrane can be increased by reducing the thickness of the membrane until its thickness is less than L_d, where:

$$L_d = \frac{D_a}{K},$$

D_a is the coefficient for bulk ambipolar diffusion of oxygen anions and holes [4] and K is the coefficient for surface reaction of oxygen gas [5]. The length scale L_d determines the transition from diffusion limited ($L \gg L_d$) to surface reaction rate limited ($L \ll L_d$) transport of oxygen ions, where L is the thickness of the membrane. Experimental results on MIEC materials suggest that L_d be in the range 50-1000 μm [5,6]. Making the membrane thinner than L_d can increase the flux only if the reaction rate can be increased at the same time. One way the reaction rate can be increased is by adding regions of highly porous catalytic materials on both sides of the thin, dense membrane. These porous regions provide a large effective area for reaction. This is illustrated in Fig.2a for the case of an oxygen separation membrane where the three regions are shown. On the left is a porous, oxygen-activation region that converts gas phase oxygen into solid-state oxygen anions, in the middle is a dense region that transports the oxygen anions, but blocks gas molecules, and on the right hand side is another porous region in which oxygen anions recombine to oxygen molecules. In the case of a fuel cell or a membrane reactor a chemical reaction occurs, such as oxidation of methane, or of hydrogen. Figure 2b shows schematically the diffusion-reaction process in pores.

The fuel cell in Fig.3 differs from the membrane in Fig.2 in that the dense layer, while still being a good ionic conductor, must be an electronic insulator to block the passage of electrons. Electric leads attached to electrodes are used to return electrons from the anode to the cathode, producing electric power in an external load. The other considerations enumerated in the above paragraph for membranes apply equally to fuel cells.

As mentioned above, to fabricate membranes with high throughput requires thin dense MIEC blocking layer and MIEC porous electrodes with large surface area. MIEC are materials which have both ionic and electronic conductivity. Commonly the MIEC have a perovskite-like structure. The materials can be proton conductors or oxygen ion conductors. The oxygen conductivity results from hopping of an oxygen ion from an occupied site to a neighboring oxygen vacancy. Apart from their application in membranes and fuel cells, some of the MIEC perovskites can also exhibit high temperature superconductivity. Thus the field of MIEC perovskite is of considerable technical and scientific interest.

The interest of MIEC in thin film forms comes from the fact that they have unique properties with scientific as well as practical applications which cannot be realized in conventional bulk sintered materials. The relatively low temperatures used in vapor deposition of thin films, i.e. with substrates at or below 800 ^{o}C, may open up new chemical reaction pathways not accessible at high temperatures

(1200 °C) used in conventional solid state chemistry reactions. The high crystalline quality of thin films makes them an attractive vehicle for fundamental characterization studies. On the practical side, thin films are ideal for membranes because of their very high permeabilities.

Our work is divided into two parts. In Chapter 1, we use models of varying degrees of complexity to describe the diffusion-reaction processes in porous MIEC electrodes in oxygen membranes and fuel cells. Analytical solutions for oxygen flux in membranes and electric power output in fuel cells are given for the case when the chemical potential drop on a membrane is small compared to RT. Numerical solutions and scaling relations are obtained for the more general cases. In Chapter 2, we develop experimental techniques towards making thin film membranes and fuel cells. Thin film blocking layers are made by pulsed laser deposition of the MIEC $SrCo_{0.8}Fe_{0.2}O_{3-\delta}$ and the ionic conductor yttrium stabilized zirconia (ZrO_2 at 5.7 and 9.5 mol% of Y_2O_3). Porous electrodes are made by vapor condensation of nano-scale particles which are then consolidated into porous continuous network.

Chapter 1

Diffusion-Reaction in Solid Oxide Membranes and Fuel Cells

1. Introduction

Previous work on porous gas electrodes has been primarily confined to the so called flooded electrodes [7,8]. In this case the pores of the electrode are partially filled with liquid electrolyte, with gas molecules dissolved in the electrolyte. Gas molecules diffuse to pore walls where the electrocatalytic reaction occurs. The rate limiting step is the supply of the reactant since the diffusion coefficient of gas molecules is much smaller than that of ions. In the case of porous MIEC electrodes the situation is normally reversed, the diffusion coefficient for ions in the MIEC is orders of magnitude smaller than that of the gas in pores. Another important distinction from the electrolytes in the previous work is that transport in MIEC is ambipolar entailing both ions and electrons. Our objective is to derive general relations between the ion current and the pore structure, based on length scales that govern diffusion-reaction in porous membranes. We assume an oxygen ion conducting membrane. The model applies equally well to proton membranes by replacing the negatively charged divalent oxygen ion with a positively charged monovalent proton ion. The performance of the membrane, i.e. the magnitude of the oxygen flux is fully determined by specifying the partial oxygen pressures $p'>p''$ at the high pressure and low pressure sides of the membrane. In this way the model can describe both oxygen membranes as well as chemical reactors, in so much that chemical reactions are related to specific oxygen partial pressures.

There are two important basic concepts in the treatment of diffusion-reaction in mixed ionic electronic conductors. One is the concept of ambipolar transport of ion-hole pairs in the bulk, which is treated in Section 2. The other is the chemical reaction at the solid-gas interface, discussed in Section 3. In Section 4, we treat the case of a dense MIEC membrane. In Section 5, we introduce the general concepts of pore structure in porous materials and apply them specifically to a model of simple cubic array of spherical grains. We then extend the treatment to membranes with porous electrodes in Section 6. We first treat the case where the chemical potential drop on the membrane is small compared to RT and derive explicit expressions for the ion current and the width of the chemical reaction region. Next we solve the diffusion-reaction equations numerically for the case where the chemical potential drop across the membrane can be large and finally we derive scaling relations for the ion current and the width of the chemical reaction zone. In Section 7, we solve diffusion-reaction equations, for the special case of small chemical potential drop across the membrane and constant gas pressure in porous electrodes, for both ions and electrons without invoking the assumption of space charge neutrality in the membrane. We provide proof that the ambipolar concept is an excellent approximation for the case of pure membrane. The ambipolar approximation does not work for fuel cells because space charge neutrality is no longer preserved in that case.

2. Ambipolar diffusion

The ion and electron current densities I_i and I_e in the MIEC membrane shown in Fig.1 are given by:

$$I_i = -\frac{D_i c_i}{RT}\left(\frac{d\mu_i}{dx} + 2FE\right) , \tag{1}$$

$$I_e = -\frac{D_e n_e}{RT}\left(\frac{d\mu_e}{dx} + FE\right) , \tag{2}$$

where D_i and D_e are the diffusion coefficients, c_i and n_e are the ionic and electronic concentrations, μ_i and μ_e are the chemical potentials of ions and electrons, E is the electric field and F is the Faraday constant. Eliminating E between Eqs. (1) and (2) we obtain:

$$\frac{I_i}{D_i c_i} - \frac{I_e}{D_e n_e} = -\frac{1}{RT}\frac{d\mu}{dx} . \tag{3}$$

From considerations of charge conservation we require that:

$$2I_i + I_e = 0 . \tag{4}$$

From Eqs. (3) and (4) we have:

$$I_i = -\frac{D_a c_i}{RT}\frac{d\mu}{dx}\ , \tag{5}$$

with $$D_a = \frac{D_i}{1+\sigma_i/\sigma_e}\ , \tag{6}$$

and $$\mu = \mu_i - 2\mu_e\ , \tag{7}$$

where D_a is defined as the ambipolar diffusion coefficient, μ is the chemical potential of ambipolar pairs, σ_i and σ_e are the ionic and electronic conductivities and we have made use of the Nernst-Einstein relations $D_i c_i = \sigma_i RT/4F^2$ and $D_e n_e = \sigma_e RT/F^2$.

For the case of a dense membrane I_i is constant and integration of Eq. (5) results in:

$$I_i = -\frac{D_a c_i}{RT}\frac{\mu'' - \mu'}{L}\ , \tag{8}$$

where μ' and μ'' are the chemical potentials at the interfaces of the membrane and L is the thickness of the membrane.

3. Chemical reaction current

The chemical reaction at the electrode-gas interfaces for O_2 molecules is given by:

$$\frac{1}{2}O_2 + 2e \Leftrightarrow O^{2-}\ . \tag{9}$$

From Eq. (9) it follows that at thermal equilibrium:

$$\frac{1}{2}\mu_g = \mu \ , \tag{10}$$

where $\mu_g = RT\ln(p/p_o)$ is the chemical potential of the gas, p is the pressure of the gas, p_o is the standard pressure. The chemical reaction at the interface gives rise to an exchange current i_{in} from the gas phase to the solid and i_{out} from the solid to the gas:

$$i_{in} = c_{go}K_g(p/p_o)^n = c_{go}K_g e^{n\mu_g/RT} \ , \tag{11}$$

$$i_{out} = Kc_i \ , \tag{12}$$

where c_{go} is the gas concentration at standard pressure, n is the order of reaction, K_g is the forward surface chemical reaction coefficient assumed to be independent of pressure, and, K is the surface chemical reaction coefficient. The reaction coefficients have the dimension of velocity. Equation (12) is the usual form [6] assumed for the reverse current. At thermal equilibrium:

$$i_{in} = i_{out} \ . \tag{13}$$

At $p=p_o$ it follows from Eqs. (11)-(13) that:

$$c_{go}K_g = c_{io}K_o \ , \tag{14}$$

where the subscripts "o" refer to quantities at $p=p_o$. At thermal equilibrium, using Eqs. (10)-(14), we can express i_{out} in the form:

$$i_{out}=c_{io}K_o e^{2n\mu/RT} . \tag{15}$$

Now assume that the chemical potential of the gas is raised to a value μ_g' while the chemical potential of the solid is kept at μ. The resulting chemical potential drop across the interface will then give rise to a net chemical reaction current $i=i_{in}-i_{out}$:

$$i=c_i K_o (e^{n\mu_g'/RT}-e^{2n\mu/RT}) . \tag{16}$$

We have made the approximation $c_{io}=c_i$ based on the fact that in the practical oxygen pressure range c_i varies little with oxygen pressure in most MIEC materials.

4. Dense membrane

We next consider a dense membrane with a pressure differential across it. In general there will be a chemical potential drop across gas-solid interfaces and across the bulk of the membrane as shown schematically in Fig.1. The chemical potential drop across the interface will result in a net chemical reaction current given by Eq. (16):

$$i_1 = c_i K_o \left(e^{n\mu'_g / RT} - e^{2n\mu' / RT}\right), \tag{17}$$

$$i_2 = c_i K_o \left(e^{2n\mu'' / RT} - e^{n\mu''_g / RT}\right), \tag{18}$$

where the indices (') and ('') refer to inlet and outlet gas-solid interfaces.

The chemical potential drop across the bulk of the membrane gives rise to the diffusion current I_i given by Eq. (8).

From the requirement of continuity of current it follows that:

$$i_1 = I_i = i_2 \,. \tag{19}$$

Eliminating μ' and μ'' between Eqs. (8) and (17)-(19) we obtain the relation:

$$I_i / c_i K_o = \frac{L_d}{2nL} \ln \frac{e^{n\mu'_g / RT} - I_i / c_i K_o}{e^{n\mu''_g / RT} + I_i / c_i K_o} \,. \tag{20}$$

There are two limiting cases. For $L \gg L_d$ transport is diffusion limited and Eq. (20) reduces to:

$$I_i = \frac{1}{2} \frac{c_i D_a}{RT} (\mu'_g - \mu''_g) / L \,, \tag{21}$$

while for L<<Ld transport is surface reaction limited and Eq. (20) becomes:

$$I_i = (c_i K_o / 2)[(p' / p_0)^n - (p'' / p_0)^n)] \,. \tag{22}$$

Figure 4 shows the plot of Ii normalized by Eq. (22) versus L/Ld for the case of n=1/2 and p'=1 atm and p"=0 atm.

The value of n=1/2 is consistent with the model of surface exchange reaction given by:

$$O_2 + 2V_s \Leftrightarrow 2O_s \tag{23}$$

$$O_s + 2e + V_o \Leftrightarrow O_o \tag{24}$$

where V_s is a vacant surface adsorption site, O_s is an oxygen atom in a surface adsorption site, V_o is a bulk oxygen vacancy, and, O_o is an oxygen ion in an oxygen lattice site. The forward and reverse exchange currents are determined by Eq. (24). If the rate limiting step is Eq. (23) then $O_s \propto V_s \sqrt{O_2}$. Under most conditions V_s is a slowly varying function of oxygen pressure and $O_s << V_s$. Thus, to a good approximation $O_s \propto \sqrt{O_2}$. Since $I_i \propto O_s$ then in that case n=1/2.

5. Transport in porous media

Porous electrodes can have different micro structures and morphologies. There are basically two types of pore systems [9]. One is that of straight pores running from one side of the electrode to the other side and with constant pore diameter or with conical pores. Straight pore geometry with large internal surface area is difficult to achieve in practice. The other consists of a percolation system of pores with a more or less regular shape or with a spongy structure, which results from packing of particles. The percolation system can have large internal surface area and porosity. The pore structure is characterized by the volume fraction of the pore ϕ, pore wall surface area per unit volume S or pore wall surface area per unit weight S/ρ (ρ is the density of porous material), and tortuosities of the solid phase τ_S and the pore space τ.

We model porous electrodes by a simple cubic array of consolidated spherical grains of radius r, with length of $2(r-\delta)$ for the unit cell, as illustrated in Fig.5.

From simple geometrical considerations, the volume fraction of the solid phase is given by:

$$1-\phi=\frac{4\pi r^3/3-6\pi\delta^2(r-\delta/3)}{8(r-\delta)^3}, \tag{25}$$

and the surface area per unit volume S is given by:

$$S=\frac{4\pi r^2-12\pi r\delta}{8r^3(1-\delta/r)^3}, \tag{26}$$

where we use the fact that the volume and area of the truncated caps of the sphere are $\pi\delta^2(r-\delta/3)$ and $2\pi r\delta$ respectively. From Eq. (25) we have:

$$1-\phi=\frac{3}{4}\pi\left[\frac{2}{9}-q^2\left(1-\frac{q}{3}\right)\right]/(1-q)^3\ , \tag{27}$$

where the ratio δ/r=q characterizes the degree of consolidation of grains.

We write S in the form:

$$S=3b(1-\phi)/r\ . \tag{28}$$

From Eqs. (26) and (28) we have the coefficient b:

$$b=(1-3q)/\left[1-\frac{9}{2}q^2\left(1-\frac{q}{3}\right)\right]\ . \tag{29}$$

The tortuosity τ_S is derived from the definition of the formation factor:

$$\sigma_{eff}=\frac{(1-\phi)}{\tau_s}\sigma\ , \tag{30}$$

where σ_{eff} is the effective medium conductivity and σ is the conductivity of the solid phase. The factor $(1-\phi)/\tau_S$ in Eq. (30) is analogous to the formation factor used for electrical conductivity and flow of fluid in pores [10,11].

σ_{eff} is related to the resistance R of the truncated sphere measured along the z axis:

$$R=\frac{1}{\sigma_{eff}}\frac{2(r-\delta)}{[2(r-\delta)]^2}\ , \tag{31}$$

and R is approximately given by:

$$R \approx \frac{2}{\sigma} \int_{0}^{r-\delta} \frac{dz}{s(z)} , \qquad (32)$$

where s(z) is the area of the cross section of the truncated sphere. In the integration we neglected to discard the four truncated caps whose axes are normal to z.

From Eqs. (30), (31) and (32) we have the result for τ_S:

$$\tau_s = \frac{2}{\pi}(1-\phi)(1-q) ln(\frac{2}{q}-1) . \qquad (33)$$

Since the conductivity is proportional to the diffusion coefficient we also have:

$$D_{eff} = \frac{(1-\phi)}{\tau_s} D \qquad (34)$$

where D_{eff} and D are the diffusion coefficients of effective medium and solid phase respectively.

For diffusion coefficient of the gas in pores D_g we use the relation:

$$D_g = \frac{1}{3} v_{th} \lambda , \qquad (35)$$

derived from kinetic theory of gases, where v_{th} is the thermal velocity of molecules and λ is the mean free path. When the thermal mean free path λ_{th} is much larger than a characteristic pore dimension λ_p, then Eq. (35) reduces to Knudsen equation with $\lambda=\lambda_p$. In the case of large pores, $\lambda_p>>\lambda_{th}$, then $\lambda=\lambda_{th}$. In the transition region we use the approximation:

$$\frac{1}{\lambda}=\frac{1}{\lambda_{th}}+\frac{1}{\lambda_p} . \qquad (36)$$

We take λ_p to be the diameter of a sphere whose volume is equal to that of the pore space in the unit cell. For the case of $\delta/r=0.1$ it follows that $\lambda_p=1.5r$.

Assuming $\delta/r=0.1$, which corresponds to a well consolidated grain structure, the simple cubic model yields $S=2.2(1-\phi)/r$, $1-\phi=0.69$, $\tau_s=1.16$. The above form for S is expected to applicable to a more general array of non-spherical grains if distribution of sizes is narrow, where r is then defined as the average effective grain radius.

The tortuosity of the solid phase on the other hand, is a very sensitive function of δ/r since it depends critically on the connectivity of grains. As $\delta \to 0$, τ_s diverges logarithmically. Real granular structures have a distribution in δ that gives rise to a percolation conductivity, which is taken into account by τ_s. For the purpose of the present calculation we assume the simple cubic model with $\delta/r=0.1$.

6. Membrane with porous electrodes in ambipolar approximation

We use the following assumptions to model the membrane:

1) The membrane consists of a porous MIEC cathode and anode, separated by a thin dense MIEC layer whose thickness is small enough so that the drop in chemical potential across it can be neglected.

2) As a result of the chemical reaction given by Eq. (9) the surface reaction current of ions, i. at the gas-pore wall interface is given by Eq. (16):

$$i = c_i K_o (e^{n\mu_g / RT} - e^{2n\mu / RT}) , \qquad (37)$$

where we denote $\mu_{g'}$ as μ_g. The corresponding chemical reaction current of electrons is -2i.

3) The pore structure is characterized by the volume fraction of the solid, (1-ϕ), pore wall surface area per unit volume, S, and tortuosity of the solid phase, τ_s, as we discussed in Section 5.

4) Pore dimensions are much smaller than the thickness L of the membrane. This allows us to treat the porous membrane as an effective medium and to neglect variations in chemical potential in the plane of the membrane. Transport equations are then one-dimensional with gas molecule, ion and electron currents flowing parallel to the direction of the pressure gradient. The ion and electron current densities I_i and I_e can then be expressed as:

$$I_i = -\frac{1-\phi}{\tau_s}\frac{D_i c_i}{RT}\left(\frac{d\mu_i}{dx}+2FE\right) , \tag{38}$$

$$I_e = -\frac{1-\phi}{\tau_s}\frac{D_e n_e}{RT}\left(\frac{d\mu_e}{dx}+FE\right) . \tag{39}$$

The spatial dependence of I_i and I_e is assumed to determined by the surface reaction current i according to:

$$\frac{dI_i}{dx} = iS , \tag{40}$$

$$\frac{dI_e}{dx} = -2iS . \tag{41}$$

In Eqs. (40) and (41) it is implicitly assumed that charge conservation is maintained because the injection of an O^{2-} ion, accompanied by the extraction of two electrons (injection of two holes), results in increases in ionic and electronic currents. Accordingly the ion and two holes diffuse together as an ambipolar pair [12] and space charge neutrality is preserved on a microscopic scale.

Similar to the derivation of Eq. (5) in Section 2, from Eqs. (38)-(41) we obtain the ion current in porous electrodes:

$$I_i = -\frac{1-\phi}{\tau_s}\frac{D_a c_i}{RT}\frac{d\mu}{dx} . \tag{42}$$

A. Membrane with small chemical potential drop

In the case when the chemical potential drop across the membrane is small compared to RT, we can neglect the variation of material parameters with chemical potential and linearize the surface exchange current, We write Eq. (37) in the form:

$$i = c_i K_o e^{n\mu_g / RT} (1 - e^{n(2\mu - \mu_g)/RT}) . \tag{43}$$

For $n(2\mu - \mu_g) << RT$ the exponential term in bracket can be linearized and we have:

$$i = K c_i (\frac{1}{2}\mu_g - \mu) / RT , \tag{44}$$

where $K = K_o e^{n\mu_g / RT}$ and we took n=1/2 (see Section 4).

Substituting Eqs. (42) and (44) in Eq. (40), and neglecting the second order term $(d\mu/dx)(dc_i/dx)$ (see Appendix B), yields a linear second order differential equation for μ:

$$\frac{d^2\mu}{dx^2} = \frac{1}{L_p^2}(\mu - \frac{1}{2}\mu_g) , \tag{45}$$

where the length scale L_p is given by:

$$L_p = \sqrt{\frac{L_d(1-\phi)}{S\tau_s}} . \tag{46}$$

The variation in the chemical potential of the gas in pores is determined by the gas diffusion equation:

$$I_g = -\frac{\phi}{\tau}\frac{D_g c_g}{RT}\frac{d\mu_g}{dx} , \tag{47}$$

$$\frac{dI_g}{dx} = -\frac{1}{2} iS , \tag{48}$$

where τ is the tortuosity of the pore space. We note that the right hand side of Eq. (48) is multiplied by -1/2. The negative sign results from the fact that molecules are consumed at the high pressure side (and generated at the low pressure side). The factor 1/2 is due to the fact that there are two atoms for each molecule. Equations (47) and (48) result in:

$$-\frac{\phi}{\tau}\frac{D_g c_g}{RT}\frac{d^2\mu_g}{dx^2} = -\frac{1}{2} iS , \tag{49}$$

we have again neglected the second order term. Substituting Eq. (44) in Eq. (49) and rearranging we have:

$$\frac{d^2\mu_g}{dx^2} = \frac{1}{L_g^{\,2}}(\mu_g - 2\mu) , \tag{50}$$

where the length scale L_g is given by:

$$L_g = 2L_p \sqrt{\frac{\tau_s}{\tau} \frac{\phi}{1-\phi} \frac{D_g c_g}{D_a c_i}} \,. \tag{51}$$

Equations (45) and (50) represent simultaneous linear second order differential equations. The general solutions in the region 0<x<L/2, obtained by diagonalizing the above equations, (see Appendix A), are given by:

$$\mu - \mu_o = (g_{11} e^{-x/L_m} + g_{12} e^{x/L_m}) \Psi_{11} + (g_{21} x + g_{22}) \Psi_{12} - \Delta\mu_g \,, \tag{52}$$

$$\mu_g - \mu_g'' = (g_{11} e^{-x/L_m} + g_{12} e^{x/L_m}) \Psi_{21} + (g_{21} x + g_{22}) \Psi_{22} \,, \tag{53}$$

where μ_o is the value of μ at x=0, $\Delta\mu_g=(\mu_g'-\mu_g'')/4$ and μ_g' and μ_g'' are chemical potentials of the gas on the high (x=-L/2) and low pressure side (x=L/2) of the membrane respectively, L_m is given by the relation:

$$\frac{1}{L_m^2} = \frac{1}{L_p^2} + \frac{1}{L_g^2} \,. \tag{54}$$

Ψ_{11}, Ψ_{12}, Ψ_{21} and Ψ_{22} are components of the eigenvectors ensuing from the diagonalization of Eqs. (45) and (50). g_{11}, g_{12}, g_{21}, g_{22} are integration constants determined by applying boundary conditions:

$$\mu = \mu_o \,, \qquad x=0 \tag{55}$$

$$-\frac{1-\phi}{\tau_s}\frac{D_a c_i}{RT}\frac{d\mu}{dx}=(1-\phi)\frac{Kc_i}{RT}(\mu-\frac{1}{2}\mu_g^{\prime\prime}) \,, \quad x=L/2 \tag{56}$$

$$\frac{d\mu_g}{dx}=0 \,, \qquad x=0 \tag{57}$$

$$\mu_g=\mu_g^{\prime\prime} \,. \qquad x=L/2 \tag{58}$$

Equation (56) equates the ion current I_i to the chemical reaction current i at the x=L/2 electrode-gas interface. Equation (57) expresses the condition that the dense layer at center of the membrane blocks the gas flow. As a consequence of the symmetry of the membrane, the solution in the range $-L/2<x<0$ is given by: $\mu(-x)-\mu_o=-\mu(x)+\mu_o$ and $\mu_g(-x)-\mu_{go}=-\mu_g(x)+\mu_{go}$, where $\mu_{go}=(\mu_g'+\mu_g'')/2$. The eigenvectors and the coefficients in Eqs. (52) and (53) are listed in Appendix A.

To calculate the enhancement of the ion current in the membrane with porous electrodes we normalize Eq. (42) by the maximum achievable ion current in a membrane without porous electrodes, $I_i^{(s)}$, where:

$$I_i^{(s)}=Kc_i\frac{\Delta\mu_g}{RT} \,, \tag{59}$$

$$\frac{I_i(x)}{I_i^{(s)}}=-\frac{1-\phi}{\tau_s}\frac{L_d}{\Delta\mu_g}\frac{d\mu}{dx} \,. \tag{60}$$

In the case where $L_g/L_p >> 1$ the chemical potential of the gas in pores is nearly constant and the linear term in Eq. (52) becomes negligible as long as L is not much larger than $3L_p$.

By solving Eq. (45) with boundary conditions (55) and (56), we have results for the constant chemical potential of the gas in pores:

$$\frac{I_i(x)}{I_i^{(s)}} = \sqrt{\frac{L_d S(1-\phi)}{\tau_s}}\,\frac{ae^{(L-x)/L_p} - e^{x/L_p}}{ae^{L/L_p}+1} + \phi \ , \tag{61}$$

$$\mu = \Delta\mu_g\left(\frac{ae^{(L-x)/L_p} + e^{x/L_p}}{ae^{L/L_p}+1} - 1\right) , \tag{62}$$

where

$$a = \left(1 + \sqrt{\frac{\tau_s(1-\phi)}{SL_d}}\right) / \left(1 - \sqrt{\frac{\tau_s(1-\phi)}{SL_d}}\right) . \tag{63}$$

B. Membrane with arbitrary chemical potential drop

In Section 6A we neglected second order term in derivation of Eqs. (45) and (50) that govern the chemical potentials of ambipolar pairs in solid and gas in pores. We also linearized the surface exchange current at solid-gas interface. In this section we treat the case without the restriction on drop of the chemical potential of the gas across the membrane by solving Eqs. (40), (42), (47) and (48) with boundary conditions the same as that in Section 5B. We use the non linear surface exchange current Eq. (37) with n=1/2. Since the transport equations do not have analytical solutions, we solve them numerically by fitting boundary conditions Eqs. (55)-(58). The results of this section are discussed in Section 8.

C. Scaling relations

We now derive on the basis of a simple physical argument scaling relations for the ion current and the width of the chemical reaction region, valid for the case where the pressure drop on porous electrodes is small, i.e., most of the pressure drop is across the dense layer.

Consider the membrane in Fig.2a. There are two limiting cases: When L is very small, the chemical potential drop due to diffusion can be neglected, transport is surface reaction limited and the ionic current is given by Eq. (22):

$$I_i = \frac{c_i K_o SL}{4}[(p^{'} / p_0)^n - (p^{''} / p_0)^n)] \tag{64}$$

where we have multiplied Eq. (22) by the factor SL/2 to take into account the increase in surface area due to electrodes. As L is increased and approaches the width of the chemical reaction region L_p the chemical potential drop due to diffusion becomes of importance and the currents computed from Eqs. (64) and (21) will be of the same magnitude. Equating Eqs. (64) and (21) we obtain the relation:

$$\frac{K_o S L_p}{4}[(p^{'}/p_0)^n-(p^{''}/p_0)^n)]=\frac{1}{2}\frac{1-\phi}{\tau_s}\frac{D_a}{RTL_p}(\mu_g^{'}-\mu_g^{''}) . \qquad (65)$$

where we have multiplied Eq. (21) by the factor $(1-\phi)/\tau_S$. From Eq. (65) we obtain the width of the reaction region L_P:

$$L_p=\sqrt{\frac{2L_d(1-\phi)}{S\tau_s}\frac{(\mu_g^{'}-\mu_g^{''})/RT}{(p^{'}/p_0)^n-(p^{''}/p_0)^n}} , \qquad (66)$$

and the enhanced current is given by:

$$I_i=c_iK_o\sqrt{\frac{L_dS}{8}\frac{1-\phi}{\tau_s}[(\frac{p^{'}}{p_0})^n-(\frac{p^{''}}{p_0})^n](\mu_g^{'}-\mu_g^{''})/RT} . \qquad (67)$$

In the limit of low gas pressure drop, i.e. $\Delta\mu_g \ll RT$, the width of the reaction region of Eq. (66) and the current enhancement calculated from Eqs. (22) and (67) reduce to $2\sqrt{L_d(1-\phi)/S\tau_s}$ and $\sqrt{L_dS(1-\phi)/\tau_s}$ respectively.

7. Membranes and fuel cells with space charge distribution

In Section 6A we solved diffusion-reaction equations for MIEC membranes in ambipolar approximation in which the electric potential is eliminated and space charge neutrality is assumed. In this section we solve diffusion-reaction equations for ions and electrons separately without invoking the assumption of space charge neutrality in the membrane. The electric potential is governed by Poisson equation.

We use the model defined in Section 6. The fuel cells differs from the membrane in that the dense layer, while being a good ionic conductor, must be an electronic insulator to block the passage of electrons. The electric leads attached to electrodes are used to return electrons from the anode to the cathode, producing electric power in an external load. For simplicity we assume the chemical potential of the gas in pores of electrodes is constant. This assumption, which follows from the fact that the diffusion coefficient for gas molecules in pores is many orders of magnitude larger than that for the ions in the solid, is valid as long as the gas pressure is not too low (see Section 6A).

The ion, electron current densities I_i, I_e and the interface reaction current i are given by the same equations as in Section 5, Eqs. (38), (39) and (44). The electric potential V satisfies the one dimensional Poisson equation:

$$\frac{d^2V}{dx^2}=-\frac{4\pi}{\varepsilon}\rho \ . \tag{68}$$

Where the charge density $\rho=-e[2(c_i-c_{io})+(n_e-n_{eo})]$ and the subscripts "o" refer to quantities at $p=p_o$. We use the relations:

$$\alpha=RT\frac{d(lnc_i)}{d\mu_i} \ , \tag{69}$$

$$\beta = RT\frac{d(\ln n_e)}{d\mu_e} . \tag{70}$$

The quantity α^{-1} is referred to in the literature as thermodynamic factor [13]. Substituting Eqs. (69) and (70) in Eq. (68) yields:

$$\frac{d^2V}{dx^2} = \frac{4\pi e}{\varepsilon RT}[2c_i\alpha(\mu_i - \mu_{io}) + n_e\beta(\mu_e - \mu_{eo})] , \tag{71}$$

where μ_{io} and μ_{eo} are the reference values of μ_i and μ_e at $x=0$. Substituting Eqs. (71), (38) and (39) in Eqs. (40) and (41) results:

$$\frac{d^2\overline{\mu_i}}{dx^2} = G\overline{\mu_i} + H\overline{\mu_e} + M , \tag{72}$$

$$\frac{d^2\overline{\mu_e}}{dx^2} = \overline{\mathrm{G}}\,\overline{\mu_i} + \overline{\mathrm{H}}\,\overline{\mu_e} + \overline{\mathrm{M}} , \tag{73}$$

where $\overline{\mu_i}=(\mu_i-\mu_{io})/RT$, $\overline{\mu_e}=(\mu_e-\mu_{eo})/RT$ and

$$G = \frac{16\pi e^2\alpha c_i}{\varepsilon RT} + \frac{S\tau_s}{1-\phi}\frac{K}{D_i} , \tag{74a}$$

$$H = \frac{8\pi e^2\beta n_e}{\varepsilon RT} - \frac{2S\tau_s}{1-\phi}\frac{K}{D_i} , \tag{74b}$$

$$\overline{G} = \frac{8\pi e^2\alpha c_i}{\varepsilon RT} - \frac{2S\tau_s}{1-\phi}\frac{K}{D_e}\frac{c_i}{n_e} , \tag{74c}$$

$$\overline{H}=\frac{4\pi e^{2}\beta n_e}{\varepsilon RT}+\frac{4S\tau_s}{1-\phi}\frac{K}{D_e}\frac{c_i}{n_e}\,, \tag{74d}$$

$$M=\frac{S\tau_s}{1-\phi}\frac{K}{D_i}\frac{\Delta\mu_g}{RT}\,, \tag{74e}$$

$$\overline{M}=-\frac{2S\tau_s}{1-\phi}\frac{K}{D_e}\frac{c_i}{n_e}\frac{\Delta\mu_g}{RT}\,. \tag{74f}$$

The general solutions to Eqs. (72) and (73) are:

$$\overline{\mu}_i=(g_{11}e^{-x/L_1}+g_{12}e^{x/L_1})\Psi_{11}+(g_{21}e^{-x/L_2}+g_{22}e^{x/L_2})\Psi_{12}+H_1\,, \tag{75}$$

$$\overline{\mu}_e=(g_{11}e^{-x/L_1}+g_{12}e^{x/L_1})\Psi_{21}+(g_{21}e^{-x/L_2}+g_{22}e^{x/L_2})\Psi_{22}+H_2\,, \tag{76}$$

where $L_1=1/\sqrt{(G+\overline{H})/2+\sqrt{(G+\overline{H})^2/4-(G\overline{H}-H\overline{G})}}\approx L_D/\sqrt{2\alpha+\beta n_e/2c_i}$ is the length scale which characterizes the electric charge distribution in the MIEC membranes and $L_D=\sqrt{\varepsilon RT/8\pi e^2 c_i}$ is the Debye length. $L_2=1/\sqrt{(G+\overline{H})/2-\sqrt{(G+\overline{H})^2/4-(G\overline{H}-H\overline{G})}}\approx L_p$ is the length scale which characterizes the distribution of the chemical potential of ions in the solid. The components of the eigenvectors $\Psi 11$, $\Psi 12$, $\Psi 21$ and $\Psi 22$, the coefficients g11, g12, g21 and g22, constants L1, L2, H1 and H2 in Eqs. (75) and (76) are listed in Appendix C.

A. Membranes

In the case of MIEC membrane coefficients g_{11}, g_{12}, g_{21} and g_{22} in Eqs. (75) and (76) are determined by boundary conditions:

$$\mu_i(0)=\mu_{io} , \qquad x=0 \qquad (77)$$

$$\mu_e(0)=\mu_{eo} , \qquad x=0 \qquad (78)$$

$$-\frac{1-\phi}{\tau_s} D_i c_i \frac{d\overline{\mu}_i}{dx} = (1-\phi)\frac{Kc_i}{RT}(\mu_i - 2\mu_e - \frac{1}{2}\mu_g^{''}) , \qquad x=L/2. \qquad (79)$$

$$\frac{1-\phi}{\tau_s} D_e n_e \frac{d\overline{\mu}_e}{dx} = -2\frac{1-\phi}{\tau_s} D_i c_i \frac{d\overline{\mu}_i}{dx} . \qquad x=L/2 \qquad (80)$$

Equation (79) equates the ion current I_i to the chemical reaction current i at the x=L/2 electrode-gas interface and Eq. (80) expresses that one ion releases two electrons at the x=L/2 electrode-gas interface.

B. Fuel cells

The solid oxide fuel cell is a high temperature, ceramic, electrochemical reactor that converts directly chemical energy into electrical energy [14,15]. The basic unit of the fuel cell consists of two porous electrodes separated by a dense oxygen ion conducting electrolyte and electrical contacts attached to the porous electrodes to allow electrons flow from anode to cathode through an external load. The dense layer in the fuel cells blocks the direct passage of gas molecules as well as electrons between the electrodes.

The general solutions to chemical potentials of ions and electrons are given by same set of equations as in the membrane case, i.e. Eqs. (75) and (76). The solution to the electric potential is:

$$V=\frac{4\pi e}{\varepsilon}[(2c_i\alpha\Psi_{11}+n_e\beta\Psi_{21})L_1^{2}(g_{11}e^{-x/L_1}+g_{12}e^{x/L_1})+V_1x$$

$$+(2c_i\alpha\Psi_{12}+n_e\beta\Psi_{22})L_2^{2}(g_{21}e^{-x/L_2}+g_{22}e^{x/L_2})+V_o]\ , \qquad (81)$$

where L_1, L_2, Ψ_{11}, Ψ_{12}, Ψ_{21}, Ψ_{22}, H_1 and H_2, are given by Eqs. (5C), (6C) and (9Cc). Coefficients g_{11}, g_{12}, g_{21}, g_{22} and constants V_1 and V_0 are determined by boundary conditions:

$$I_e=0\ , \qquad x=0 \qquad (82)$$

$$V=0\ , \qquad x=0 \qquad (83)$$

$$\overline{\mu_i}=0\ , \qquad x=0 \qquad (84)$$

$$I_i=(1-\phi)i\ , \qquad x=L/2 \qquad (85)$$

$$V(-L/2)-V(L/2)=2eI_i(0)r\ , \qquad (86)$$

$$I_e(L/2)=2[I_i(0)-I_i(L/2)]\ , \qquad (87)$$

where r is the external load resistor. Equation (82) expresses the condition that the dense layer at the center of the membrane blocks the flow of electronic current. Equations (83) and (84) express that both electric potential and chemical potential of ions are continuous at the center of the membrane. Equation (85) equates the ion current I_i to the chemical reaction current i at the x=L/2 electrode-gas interface and Eq. (86) is the consequence of ohm's law. Equation (87) expresses the continuity of current.

We first use boundary condition (82) to determine constant V_1. For I_e=0 at x=0, this means:

$$\frac{d\overline{\mu_e}}{dx}-\frac{F}{RT}\frac{dV}{dx}=0\ . \tag{88}$$

Substituting Eq. (76) and (81) in Eq. (88) we have:

$$V_1=[A_1(g_{11}-g_{12})+A_2(g_{21}-g_{22})]\frac{RT}{F}\ , \tag{89}$$

where

$$A_1=-\frac{\Psi_{21}}{L_1}+\frac{4\pi F^2L_1}{\varepsilon RT}A_3\ , \tag{90a}$$

$$A_2=-\frac{\Psi_{22}}{L_2}+\frac{4\pi F^2L_2}{\varepsilon RT}A_4\ , \tag{90b}$$

$$A_3=2c_i\alpha\Psi_{11}+n_e\beta\Psi_{21}\ , \tag{90c}$$

$$A_4 = 2c_i \alpha \Psi_{12} + n_e \beta \Psi_{22} , \tag{90d}$$

$$A_5 = \frac{\Psi_{11}}{L_1} - \frac{8\pi F^2 L_1}{\varepsilon RT} A_3 , \tag{90e}$$

$$A_6 = \frac{\Psi_{12}}{L_2} - \frac{8\pi F^2 L_2}{\varepsilon RT} A_4 . \tag{90f}$$

V_0 is determined by boundary condition (83):

$$V_o = -[A_3 L_1^2 (g_{11} + g_{12}) + A_4 L_2^2 (g_{21} + g_{22})] . \tag{91}$$

Substituting Eqs. (75), (76) and (81) in boundary conditions (84)-(87) yields four linear equations for the four integration constants:

$$\Psi_{11} g_{11} + \Psi_{11} g_{12} + \Psi_{12} g_{21} + \Psi_{12} g_{22} = -H_1 , \tag{92}$$

$$K_1 g_{11} + K_2 g_{12} + K_3 g_{21} + K_4 g_{22} = 0 , \tag{93}$$

$$K_5 g_{11} + K_6 g_{12} + K_7 g_{21} + K_8 g_{22} = 0 , \tag{94}$$

$$K_9 g_{11} + K_{10} g_{12} + K_{11} g_{21} + K_{12} g_{22} = 0 , \tag{95}$$

where constants K_1-K_{12} and coefficients g_{11}, g_{12}, g_{21}, g_{22} in Eqs. (92)-(95) are listed in Appendix C.

When the load resistor r approaches infinity:

$$\Delta V = V(-L/2) - V(L/2) \approx \frac{\mu_g^{'} - \mu_g^{''}}{4F} \frac{2}{1 + \frac{4c_i\alpha}{n_e\beta}} \, . \tag{96}$$

At open circuit condition, that is at thermal equilibrium, Eq. (10) holds. By differentiating Eq. (10) and Assuming μ_g is constant we have:

$$2d\mu_e = d\mu_i \, . \tag{97}$$

From Eqs. (69) and (70):

$$dc_i / c_i = \alpha d\mu_i / RT \ ,$$

$$dn_e / n_e = \beta d\mu_e / RT \ ,$$

and the charge conservation condition:

$$2|dc_i| = |dn_e| \ , \tag{98}$$

Equations (69), (70), (97) and (98) result in:

$$\frac{4c_i\alpha}{n_e\beta} = 1 \, . \tag{99}$$

Substituting Eq. (99) in (96) we have:

$$\Delta V = V(-L/2) - V(L/2) \approx \frac{\mu_g^{'} - \mu_g^{''}}{4F} = V_N \,, \qquad (100)$$

where V_N is the Nernst open circuit voltage.

8. Discussion

A. Membranes

By specifying the material parameters of the bulk MIEC, L_d, and D_a, and the parameters characterizing the porous structure, D_g, S, τ, τ_s and ϕ, and the gas pressure p, we can evaluate numerically the chemical potentials and ion current derived in the previous sections.

For a wide variety of MIEC perovskites in the temperature range 700-900 ^oC, L_d lies in the range 50 to 1000 μm. In the following we use a representative value L_d=100 μm. For D_a we use the value 5×10^{-7} cm^2/sec which is the upper bound for the observed oxygen diffusion coefficients in perovskites and we take $c_i=5\times10^{22}$ cm^{-3}. At 10^3 K we have $v_{th}=8.1\times10^4$ cm/sec, $c_g=7.3\times10^{18}P/P_o$ cm^{-3}, and $\lambda_{th}=0.24P_o/P$ μm where P_o=1 atm. For D_g we use Eq. (35) and take τ=1.93 [10].

We first discuss the linear solutions in section 6A, i.e., the chemical potential drop across the membrane is small compared to RT. In Fig.6 we plot the spatial dependence of the chemical potentials of ambipolar pairs μ and of gas μ_g for different gas pressures calculated from Eqs. (52) and (53) for a membrane with

$L=4$ μm, $S=10^6$ cm^{-1}. We note the striking effect the ratio L_p/L_g has on the behavior of μ and μ_g. When $P=1$ atm and $L_g/L_p>>1$ most of the drop in μ_g is across the dense layer. We note that since the total ion current is proportional to the area between μ_g and μ most of the contribution to the ion flux comes from the region $3L_p$ at the center of the membrane. This is well demonstrated in Fig.7 which shows the normalized ion current $I_i(x)/I_i^{(s)}$, given by Eq. (60), peaking near the center of the membrane. On the other hand for $P=0.01$ and 0.001 atm, $L_g/L_p<1$, there is an appreciable drop in μ_g over the porous electrodes and most of the contribution to the ion flux comes from regions L_m wide near the outer interfaces of the electrodes. Figure 7 shows that for these values of P the ion current rises steeply near the boundaries $\pm L/2$ and is flat in the central region of the membrane.

The total normalized ion current through the membrane, given by $I_i(0)/I_i^{(s)}$, is plotted in Fig.8 as a function of membrane thickness L for different values of S and P. The current peaks as a function of L because at small L the effective surface area of the electrodes is small, while at large values of L, the loss in chemical potential due to pressure drop in the electrodes becomes significant. The current is maximum at a thickness $L\approx3L_m$. For a given value of S the current is reduced as the pressure P is decreased because the gas pressure drop in the electrodes becomes more significant, as can be seen in Fig.6. For very thick films, $L>>L_m$, the current can actually decrease with increasing S. This is because the increase in current due to increased surface area of the catalyst is more than compensated by the decrease in current due to the large pressure drop in the electrodes resulting from the decrease in pore size.

In Fig.9 we plot the peak values of $I_i(0)/I_i^{(s)}$ from Fig.8 as a function of S for different values of P. We note that at high pressure (P=1 atm) $I_i(0)/I_i^{(s)}$ increases as $\sqrt{S}$ while at low pressure it saturates rapidly with increasing S. In Fig.10 we plot $I_i(0)/I_i^{(s)}$ for $L=3L_m$ as a function of L_d for different values of L_g/L_p with $S=10^6$ cm^{-1}. For over most of the range of L_d and L_g/L_p we note that $I_i(0)/I_i^{(s)} \propto \sqrt{L_d}$.

Now we turn to the membrane with arbitrary gas pressure drop calculated in section 6B. In Fig.11 we plot the spatial dependence of the chemical potentials of ambipolar pairs μ and of gas μ_g for inlet pressure p'=1 atm and different outlet pressures p" calculated for a membrane with n=1/2, L=4 μm and surface area $S=10^6$ cm^{-1}. We note that the spatial dependence of μ is practically independent of outlet pressure while μ_g in the low pressure electrode exhibits a strong dependence on outlet pressure. The spatial dependence of the current $I_i(x)$ is shown in Fig.12 and in Fig.13 we show the dependence of $I_i(0)$, which is equal to the total flux through the membrane, on outlet pressure p". $I_i(0)$ reaches saturation at low values of p". Figure 14 shows the current enhancement given by the ratio of $I_i(0)$ to the current for the dense membrane given by Eq. (22). The enhancement only weakly depends on p" and for the given set of parameters its value is about 80.

When the outlet pressure p" is close to inlet pressure p', the chemical potentials of ambipolar pairs μ and of gas μ_g are anti symmetric as that in the linear case (Fig.6a). When the outlet pressure p" is low the chemical potential of the gas, with p'=1 atm on the left side of the membrane, is a combination of that of the linear cases: on inlet high pressure side it behaves the linear case for the high gas pressure situation (Fig.6a) and on outlet side there is an appreciable drop in μ_g near the outer interface of the porous electrode (Fig.6c). We note that the concepts developed for the linear transport equations in Section 6A provided guidance for the more complex case of the membrane with arbitrary gas pressure drop in Section 6B.

By using scaling relation of Eqs. (66) and (67) in the limit of $\Delta\mu_g << RT$, we plot in Fig.8a the current enhancement at L=Lp. The results (circles) of the scaling relations fit well to that of the detailed calculation.

To calculate the chemical potentials of ambipolar pairs and the flux enhancement for the membrane with space charge distribution in Section 7A, we require additional material parameters characterizing the bulk MIEC. These are α, β, ε, σ_i/σ_e, and n_e. We assume $\sigma_i/\sigma_e=0.01$ [16] and $\alpha=0.01$ [17] which are representative values for MIEC, and $\varepsilon=10$ a typical value for oxide of heavy metals. Since $\sigma_i/\sigma_e<<1$, we have good approximation $D_i \approx D_a$ and we take $D_a=10^{-7}$ cm^2/sec. Moreover, $D_e=4c_iD_i\sigma_e/(n_e\sigma_i)$ which follows from the Nernst-Einstein relations. To calculate β from Eq. (70) we assume that the chemical potential of electrons μ_e is given by the mean fermi energy of the free electron gas model:

$$\mu_e = \frac{3h^2}{40m_e}\left(\frac{3n_e}{\pi}\right)^{2/3}, \qquad (101)$$

where h is Plank constant and m_e is the mass of the electron.

From Eqs. (70) and (101) we obtain:

$$\beta = \frac{5}{3}\frac{4\pi m_e RT}{h^2}\left(\frac{3}{\pi}\right)^{1/3} n_e^{-2/3}. \qquad (102)$$

For the given set of parameters, Equations (99) and (102) yielded $n_e=4.2\times10^{22}$ cm^{-3} and $\beta=0.048$ at 1000 K.

Using the above parameters, we calculate the chemical potential of ambipolar pairs and the enhancement of ion current. Comparing the results of this calculation with that of ambipolar approximation given by Eqs. (61) and (62) of Section 5A, see Fig.15 for chemical potential and Fig.16 for enhancement, we find the agreement is excellent. We also varied σ_i/σ_e in the range of 10^{-2} to 10^4 in the calculation of the chemical potential and the enhancement, the ambipolar approximation gives the same results as that of the membrane with space charge distribution for the given set of parameters.

B. Fuel cells

We use the same set of parameters as in the membrane with space charge distribution to calculate the output voltage and current for the fuel cell.

In Fig.17 we plot the spatial dependence of the ion current $I_i(x)$ and electronic current $I_e(x)$ calculated from Eqs. (38) and (39) for a membrane with L=10 μm, r=1 Ω, $S=10^6$ cm^{-1}, $L_d=100$ μm. The ion current peaks near the center of the membrane while electronic current is zero at the center and reaches maximum at outer surfaces of the membrane. The maximum of the electron flux is twice that of the ion flux, this reflects the fact of the charge conservation condition in the system. The spatial dependence of the chemical potentials of ions and electrons are plotted in Fig.18, we note that the chemical potential of ions is continuous while there is a discontinuity for the chemical potential of electrons since the blocking layer at the center of the membrane is transparent to ions and it blocks electrons.

Figure 19 shows the voltage distribution in the membrane and Fig.20 is the normalized charge distribution ρ/c_i. Negative oxygen ions accumulate at high oxygen pressure (left) side because the oxygen molecules which take electrons from metal contact diffuse into the left surface of the membrane, at the low oxygen pressure (right) side oxygen ions go out of the membrane and release electrons to the metal contact leaving behind the positive charged area. Near the center of the membrane oxygen ions diffuse from the left to the right side of the membrane making left side positive charged while the right side negative charged.

There are two length scales that characterize the fuel cell. $L_1 \propto L_D$ that governs the physical process at the metal-electrode and electrode-blocking layer interfaces, $L_2 \approx L_p$ that governs the physical process inside porous electrodes. The electrochemical potential of ions $\eta_i=\mu_i-2eV$ is continuous in the membrane while the electrochemical potential of electrons $\eta_e=\mu_e-eV$ is only continuous in the electrodes, see Fig.21 and Fig.22. The derivatives of the electrochemical potentials are proportional to the driving forces, so that the driving forces of the ions and electrons are continuous inside porous electrodes.

Figure 23 shows the output voltage versus the current for different values of S. For a given S the voltage decreases linearly as the current increases because of internal energy dissipation. The short circuit current increases as square root of the surface area S.

Summary

The goal of chapter 1 was to determine the maximum theoretically achievable ion flux in an electrocatalytic membrane and a fuel cell. For this purpose we have kept the model as simple as possible. In practice we need to take into account several possible additional factors. Electrodes might not be symmetrical, the blocking layer might not be sufficiently thin to neglect the drop in chemical potential, and there can be an activation energy for the ion-hole pair to transfer from the electrode to the blocking layer. To take these factors into account requires additional boundary conditions and correspondingly more complexity in the solution, although its basic form remains essentially the same as that given by Eqs. (52) and (53). The condition for the blocking layer of thickness L_b to have negligible effect is $L_b \ll L_m$.

Diffusion-Reaction transport equations in MIEC membranes were solved by using the concept of ambipolar ion-hole pairs. The surface exchange current depends on the oxygen pressure at the gas-solid interface. Based on an effective medium model of an oxygen membrane, consisting of two porous MIEC electrodes separated by a thin dense MIEC, the transport equations for the gas molecules in the pores, and for the ion-hole pairs in the solid, are characterized by the length scales $L_g = 2L_p\sqrt{[\tau_s\phi / \tau(1-\phi)][D_g c_g / D_{IE} c_i]}$ and $L_p = \sqrt{L_d(1-\phi)/S\tau_s}$ respectively, where $L_d=D_a/K$, K is the surface reaction coefficient, D_a and D_g are the diffusion coefficients of the ion-hole pairs in the solid and of the molecules in the pores, c_i and c_g are the concentrations of ions in the solid and molecules in pores, S the pore surface area per unit volume, ϕ the porosity and τ_s and τ the tortuosities of the solid and pore phases respectively. In the linear solution case when $L_g>L_p$ the chemically active region of the electrodes is near the center of the membrane $\approx 3L_p$ wide, which is also close to the optimum thickness of the membrane. The gas pressures in the two electrodes are then essentially constant and equal to the inlet and outlet pressures respectively and the enhancement in the ionic current, over the membrane without porous electrodes, is given by $\sqrt{L_d S(1-\phi)/\tau_s} + \phi$. With $L_d=100$ µm, which is a representative value for perovskites in the temperature range 700-900 °C, and a surface area of $S=10^6$ cm^{-1}, the ion current increases by 77 over that of the dense membrane, and $L_p= 0.77$ µm. When $L_g \approx L_p$, then the chemically active regions, $\approx L_m$ wide, are both at the center and at the outer interfaces of the membrane, where the length scale $L_m^{-2}=L_g^{-2}+L_p^{-2}$. Finally when $L_g<<L_p$ the

chemically active regions, $\approx L_g$ wide, move out almost entirely to the outer interfaces of electrodes, and the theoretical enhancement is substantially reduced because of mass transport limitations in porous electrodes.

In the case of membranes with arbitrary gas pressure drop, when the outlet pressure p" is close to inlet pressure p', the chemical potentials of the ambipolar pairs μ and of the gas μ_g are anti symmetric as that of linear case. When the outlet pressure p" is low, the chemical potential of the gas, with p'=1 atm on the inlet side of the membrane, is a combination of that of the linear cases: on the inlet high pressure side it behaves the linear case for the high gas pressure situation (Fig.6a) and on outlet side there is an appreciable drop in μ_g on the outer interface of the porous electrode (Fig.6c). The enhancement only weakly depends on outlet pressure p" and its value is about 80 for a membrane with inlet pressure p'=1 atm, n=1/2, L=4 μm and surface area S=10^6 cm^{-1}.

The linearized transport equations for oxygen ions and electrons in a fuel cell, consisting of two porous MIEC electrodes separated by a thin dense ionic conductor, are solved. The electric potential satisfies Poisson equation. The spatial distribution of the electric potential, normalized charge density, the chemical potentials of ions and electrons changes abruptly at the metal-electrode and electrode-blocking layer interfaces, that is characterized by the length scale $L_1 \approx L_D / \sqrt{2\alpha + \beta n_e / 2c_i}$, where $L_D = \sqrt{\varepsilon RT / 8\pi e^2 c_i}$ is the Debye length. The spatial distribution of the ionic and electronic fluxes is characterized by the length scale $L_2 \approx L_p = \sqrt{L_d (1-\phi) / S\tau_s}$. For a given surface area S the voltage decreases linearly as the current increases because of the internal energy dissipation. The short circuit current increases as square root of the surface area S.

Chapter 2

Solid oxide thin films and nano-scale particles of ionic and MIEC materials

In Chapter 1 we determined the optimal dimensions required to achieve large enhancement in oxygen flux in thin film membranes and fuel cells. The requirements are two fold: high surface area electrodes to enhance the chemical reactions at the electrodes and a thin dense layer to block the molecules while enabling the passage of ions without significant loss in chemical potential. In this chapter we describe experimental techniques we developed for fabrication of dense thin solid oxide films in the thickness range 0.05-1 µm and porous electrodes consisting of oxide particles as small as 50-100 Å having surface areas 20 m^2/gm. The thin films and nano-scale particles were prepared by laser ablation of appropriate solid oxide targets. X-ray, SEM and TEM microscopy, electrical conductivity and optical transmission measurements were used to characterize the materials. We focus on the ionic conductor yttrium stabilized zirconia (YSZ) and the MIEC $SrCo_{0.8}Fe_{0.2}O_{3-\delta}$.

Yttrium stabilized cubic ZrO_2 of fluorite crystal structure is an oxygen ion conductor with important uses as an electrolyte in solid oxide fuel cell or oxygen sensor, Fig.24 shows the unit cell of cubic ZrO_2. The oxygen ions hop via oxygen vacancies. Vacancy generation is due to replacement of the host (Zr^{4+}) lattice point by alliovalent

Y^{3+} doping. Since an oxide vacancy has an effective charge of +2, so two Y^{3+} ions produce one oxygen ion vacancy.

The ABO_3 perovskites, with the structure shown in Fig.25, exhibit a variety of interesting properties such as ferromagnetism, ferroelectricity, pyro and piezoelectricity, superconductivity, large thermal conductivity, fluorescence and catalytic activity. The A site is a large cation, usually a rare earth, and B site is a small cation, usually a transition metal. Oxygen ion deficiency can be achieved by alliovalent doping, which can result in a large ionic and electronic conductivities. Such materials, referred to as mixed ionic electronic conductors, are used as active elements in membranes and fuel cells. The perovskite $SrCo_{0.8}Fe_{0.2}O_{3-\delta}$ has received a great deal of attention [18,19] because of its high oxygen ion diffusion coefficient. However detailed knowledge and understanding of the transport and optical properties of these materials is very limited. For fundamental understanding as well as device application it is desirable to study this material in thin film form. Thin films can be prepared with near ideal density, highly oriented and with high crystalline perfection and they are well suited for spectroscopic studies.

1. Pulsed laser deposition of thin films and nano-scale particles

Pulsed laser deposition (PLD) is a deposition technique that has been used in growth thin films of a wide variety of compounds such as semiconductor, insulators, metals and alloys [20,21]. It enables rapid fabrication of materials with high crystalline quality over a wide range of composition. An important attribute of PLD is that the stoichiometry of the target is maintained in the deposited film and the deposition rates are high. Film growth can be carried out in a reactive environment containing any kind of gas. This attribute is particularly important for the case of the complex MIEC oxides where maintaining stoichiometry can be problem such as in the case of sputtering or conventional evaporation.

The laser-target interaction [21] is a very complex physical phenomenon. When the laser radiation is absorbed by a solid surface, electromagnetic energy is converted into thermal, chemical, and even mechanical energy to cause evaporation, ablation, excitation, plasma formation and exfoliation.

The experimental setup of PLD system is depicted in Fig.26. We use a 246 nm excimer laser, Lambda Physics LPX300i. The laser beam, focused by a quartz lens, is incident on the target through a quartz window at a 45^o angle of incidence. The laser power density incident on the target was around 1 to 3 J/cm^2 over an area of 2x6 mm^2, the pulse width was 30 ns and repetition rate was from 1 to 50 Hz. The target holder was rotated at 2 rev/sec and the substrate holder can be heated up to 900 ^oC. Silica or single crystal MgO substrates were cemented with silver paste on the substrate holder which was 3.5 inch from the target surface.

The MIEC laser targets, 1 inch in diameter and 1/4 inch thick, were made by sintering $SrCo_{0.8}Fe_{0.2}O_{3-\delta}$ powder [22]. Two different targets were made: target 1 was heated at 1 $^oC/min$ to 1100 ^oC, held there for 12 hours and cooled at 1 $^oC/min$; target 2 was heated at 1 $^oC/min$ to 1160 ^oC, held there for 60 hours and cooled at 1 °C/min. The targets were mounted in a vacuum system with base pressure 10^{-6} torr. The pressure during deposition was maintained at 70 mtorr of oxygen. The films were deposited at 600 °C in the thickness range 0.05-1 µm. The deposition rates depended on the sintering conditions of the targets. Target 1 yielded a deposition rate of 0.06 Å/pulse while target 2 yielded a deposition rate, under the same deposition conditions, of 0.02 Å/pulse. This difference in deposition rates between the two targets is likely due to a higher density of the target 2.

The $(ZrO_2)_{1-x}(Y_2O_3)_x$ laser targets, two sintered pellets with x=0.057 and 0.095 and one single crystal disc with x=0.095, were provided by Cerac Company. The films were deposited as a function of substrate temperature, 22-800 °C, laser energy and ambient oxygen pressure. Figure 27 shows the deposition rates versus laser energy and distance between the target and substrate. For different distances between the target and the substrate, the deposition rates increase linearly as the laser energy increases.

A simple technique of fabrication of nano-scale particles is by evaporating the source material in He or other gas at pressures of several torr or higher. As a result of the rapid cooling by the ambient gas atmosphere, the vapor near the evaporation source becomes supersaturated and condenses into small particles. The particles are then collected on a cold surface. The final size of the particles depends on the width of the formation zone near the evaporation source. At high gas pressure and fast evaporation rate the particles become larger. So far in the literature [23,24] only elemental metals and the simple oxides, such as SiO_2 and TiO_2, have been reported. We have now extended the technique to the more complex oxides YSZ (yttrium stabilized zirconia, ZrO_2 with 9.5 mol% of Y_2O_3) and $SrCo_{0.8}Fe_{0.2}O_{3-\delta}$. YSZ is an ionic conductor used as the electrolyte in solid oxide fuel cells and $SrCo_{0.8}Fe_{0.2}O_{3-\delta}$ belongs to a class of mixed ionic electronic conductors (MIEC) that are used as the dense layer as well as the catalyst electrodes in membrane reactors. Figure 28 shows the schematic diagram of our experimental setup for making nano-scale particles. The ambient gas was mixture of 4:1 of He and O_2 at the pressure of 350 torr. The cold surface on which the particles were collected was a copper disc 3 inch in diameter positioned 2 inch above the target and maintained at 100 K. The particles were removed from the collector disc by dispersing in water or methanol. The liquid was subsequently evaporated and the particles consolidated into a porous network by annealing.

2. Electrical conductivity measurement

Impedance measurements were made in air ambient in the temperature range 22-800 ^oC by using a dynamic signal analyzer Hewlett-Packard 3562A in the frequency range 0.1 Hz to 100 kHz. The output signal of 50 mV was applied to the sample in series with a standard resistor R_s. The voltage V_1 was across the sample Z and R_s, the voltage V_2 across R_s. The sample impedance was derived from the ratio V_1/V_2 measured with the analyzer: $V_1/V_2=(R_s+Z)/R_s$.

For thin film, measurements were made in the plane of the samples. Platinum or gold current electrodes, separated by a gap

100-1000 μm, were deposited on the films by RF sputtering or evaporation. The sample was heated up to 800 °C at a rate of 6 °C/min and held at that temperature for 30 minutes before taking the data. Then it was cooled at the rate of 6 °C/min to the next lower temperature, and data was taken after waiting for 30 minutes for equilibrium.

Measurements were also made on YSZ single crystal disc to compare with thin films deposited by PLD. Current contacts to the YSZ single crystal disc were made by RF sputtering platinum electrodes on both sides of the disc. Platinum electrical leads were cemented to the electrodes with silver paste.

3. Structure and electrical conductivity of YSZ

The impedance spectrum shown in Fig.29 is typical of an ionic conductor sandwiched between two blocking electrodes. The sample of $(ZrO_2)_{1-x}(Y_2O_3)_x$ used in our experiment was 1/2 inch in diameter, 1/64 inch thick and with 9.5 mol% Of Y_2O_3. 1000 Å platinum electrodes was sputtered on the disc.

The observed impedance is represented by two terms: the impedance Z_i is due to the electrode-electrolyte interfaces and Z_b is due to the bulk impedance, $Z=Z_i+Z_b$. The interface term Z_i has the constant phase angle (CPA) form [25]:

$$Z_i = \frac{A}{(j\omega)^n}\ , \tag{103}$$

where A and n are constants, $0<n<1$, $j=(-1)^{1/2}$ and $\omega=2\pi f$, f is the frequency of the applied voltage. The bulk impedance is given by:

$$Z_b = \frac{1}{\frac{1}{r} + j\omega C}, \tag{104}$$

where r is the resistance of the sample and C is the frequency dependent capacitance. $r=l/\sigma s$, where σ is the ionic conductivity, l is the sample thickness and s is the area of the electrodes. $C=s\varepsilon_o\varepsilon/l$, where ε_o is the vacuum permittivity and $\varepsilon=\varepsilon'-j\varepsilon''$ is the permittivity of the solid. We use Cole-Cole function [26] for ε in Z_b:

$$\varepsilon = \varepsilon_\infty + \frac{(\varepsilon_s - \varepsilon_\infty)}{1+(j\omega\tau)^{1-\alpha}}. \tag{105}$$

In Fig.30 we plot the negative imaginary part versus real part of the impedance, i.e. the Cole-Cole plot, where open circles are the measurements and the solid line is the result of our fitting. The values of $A=5.85\times10^4$, $n=0.92$, $r=6.08\times10^5\ \Omega$, $\varepsilon_\infty=24.8$ (high-frequency dielectric constant), $\varepsilon_s=115$ (static dielectric constant), $\tau=2\times10^{-4}$ sec (relaxation time) and $\alpha=0.5$ were determined by fitting $Z=Z_i+Z_b$ to the observed impedance spectrum at 250 ^oC.

Figure 31 shows the Cole-Cole plots measured at 400 ^oC and 800 ^oC on a 1 μm thick YSZ film. The Cole-Cole plots of polycrystalline materials are interpreted in the simplest form on the basis of the grain-boundary model depicted in Fig.32. The equivalent circuit for this model is shown in (b), where R_i in parallel with C_i represents the impedance of the grain interior and R_b in parallel with C_b represents the impedance of the grain boundary and the CPA impedance represents the blocking contacts of the film. The Cole-Cole plot in (c), computed for typical values of the equivalent circuit parameters given in the figure, shows a high frequency arc corresponding to the grain interior, a low frequency arc corresponding to the grain boundaries and a low frequency "spur" corresponding to the CPA. The experimental data does not reproduce all the features of the model. This is in part due to the fact that the very low (<0.1 Hz) and very high (>100 KHz) frequency regions of the Cole-Cole plot are outside the frequency range of our analyzer and also in part due to the fact that the model in Fig.32 may be oversimplified. This introduces an uncertainty in extracting the bulk conductivity from the data. We have chosen as a representative value for the resistance of the film the intercept of the large arc with the x-axis as indicated by the arrows in Fig. 31. The conductivity determined in this way for several films deposited from different targets are compared with the conductivity of the single crystal disc in Fig 33. We note that the thin film conductivities exhibit the same activation energy as the single crystal but the values are an order of magnitude lower. This is probably due to the resistance of grain-boundaries.

4. $SrCo_{0.8}Fe_{0.2}O_{3-\delta}$

A. Structure of $SrCo_{0.8}Fe_{0.2}O_{3-\delta}$

The composition of the $SrCo_{0.8}Fe_{0.2}O_{3-\delta}$ films determined by energy dispersive X-ray (EDX) was found to be unchanged from that of the target. In Fig.34, SEM shows that the average grain size is 700 Å in a 500 Å thick film (top) and increases to about 1500 Å for films 3000 Å thick (bottom). The X-ray diffraction spectrum in Fig.35 shows that the films are highly oriented. The highest peak is in (110) orientation. The lattice constant derived from the X-ray diffraction spectrum is 3.9 Å. No difference was found in the structure of films made from targets 1 and 2.

B. Electrical conductivity of $SrCo_{0.8}Fe_{0.2}O_{3-\delta}$

The temperature dependence of σ of two films 3000 Å thick, on MgO substrates, deposited from targets 1 and 2, is shown in Fig.36. The conductivities of the two films do not differ significantly from one another. Over the entire temperature range the ac conductivity was frequency independent and equal to the dc conductivity, indicating that the conductivity is primarily electronic. The measured conductivity is thermally activated in the temperature range 22-500 ^{o}C, with an activation energy of 0.17 eV and from 500-800 ^{o}C it becomes essentially temperature independent.

We first discuss the mechanism for electronic and ionic transport in perovskites. In general the cations can appear in the valence states $A^{1+}B^{5+}O_3$, $A^{2+}B^{4+}O_3$ and $A^{3+}B^{3+}O_3$. Defects can be introduced by alliovalent doping. By substituting on the A site the divalent Sr, oxygen vacancies are created simultaneously for charge compensation so that a fraction of the B ions, cobalt this case, are in the tetravalent states i.e. $Sr^{2+}Co^{3+}(Co^{4+})O_{3-\delta}$. This results in p-type electronic conductivity, while the oxide ion conduction is via oxygen vacancies. The larger the δ, the larger the ionic conductivity will be. A small amount of Fe is added to $SrCoO_{3-\delta}$ in order to stabilize the cubic structure [27]. The Fe^{3+} ion stabilizes the lattice because it has a larger ionic radius than Co^{3+}. The ionization energy to produce Fe^{4+} is 3.5 eV larger than that for Co^{4+} [28] so Fe ions are mainly in their Fe^{3+} valence states.

Because the electrical conductivity of $SrCo_{0.8}Fe_{0.2}O_{3-\delta}$ is thermally activated, it falls into the category of charge transfer perovskites [29]. The holes are localized on the B^{4+} sites and hop via oxygen 2p states to the neighboring B^{3+}:

$$B^{4+} - O^{2+} - B^{3+} \; . \tag{106}$$

In order to satisfy the charge neutrality condition when there are δ oxygen vacancies per unit cell, there must be (2δ) B^{3+} ions and $(1-2\delta)$ B^{4+} ions. In the limit of small vacancy concentration ($\delta<<3$), the conductivity σ is proportional to the product of the probabilities of the valences B^{4+} and B^{3+} and the concentration of O^{2-}:

$$\sigma = C(1-2\delta)(3-\delta)2\delta e^{-E_a/KT} , \tag{107}$$

where E_a is the activation energy for the transfer process and C is a constant.

We associate the observed activation energy in Fig.36 with the hopping process given by Eq. (106). We fit Eq. (107) to measurements, by using experimental values δ [16,22], with E_a=0.17 eV and C=673 $(\Omega cm)^{-1}$ as best fit parameters.

C. Optical properties of $SrCo_{0.8}Fe_{0.2}O_{3-\delta}$

Optical transmission measurements were made on a Cary spectrophotometer in the range 0.5 eV to 6.5 eV. In Fig.37 we show the optical density for three films with different thicknesses deposited on silica, all made with target 2. All three films exhibit similar features, a steep rise between 2-3 eV, a shoulder between 3-4 eV and a peak near 6 eV. The optical absorption coefficient plotted in Fig.38 was derived from the difference in the optical densities OD of the 1400 Å and the 1000 Å films:

$$\alpha = (OD_1 - OD_2)/\Delta , \tag{108}$$

where Δ is the difference in the thickness of the two films. This procedure eliminates, to a good approximation, the effect of reflection from the air-film and film-substrate interfaces.

In order to interpret qualitatively the optical spectra we consider the band structure of $SrCo_{0.8}Fe_{0.2}O_{3-\delta}$. The 3d electrons of the transition metals, which are in octahedral coordination, are strongly localized and form narrow bands. Because of the crystalline field of the oxygen ion octahedron, the 3d states split into two levels. A high energy band e_g corresponding to d_{z^2}, $d_{x^2-y^2}$ electron orbits and low energy band t_{2g} corresponding to d_{xy}, d_{xz}, d_{yz}. Outer s and p electrons form extended bands and can be treated by means of one-electron theory.

An effective one-electron density of state diagram is show in Fig.39. The partially filled $3d^5$ band corresponds to t_{2g}. The empty $3d^{5*}$ band is due to the e_g states and the multiplet splitting of d levels. The 2p electrons of the oxygen form an extended filled band and the 4s electrons of the transition-metal form an extended empty band.

We associate the steep rise in the absorption in the range 2-3 eV with the strong allowed electric dipole transition from the filled 2p band to the empty $3d^{5*}$ band. The rise in absorption between 4-6 eV we associate with the transition 2p-4s and $3d^5$-4s. The later transition may be suppressed somewhat because of the forbidden nature of 3d-4s electric dipole transition, but covalence of the s electrons with the anion 2p wave function overcomes the selection rule to a large extent [30]. The $3d^5$-$3d^{5*}$ and 2p-$3d^5$ transitions are expected to be weak. In Fig.38 we show schematically the different contributions to the absorption. The absorption at low energy is due to the water absorption peak centered at 0.4 eV [31].

5. Nano-scale particles

A. YSZ

The TEM in Fig.40 shows that the particles are in the range 30-100 Å and that they exhibit facets and images of lattice planes, indicating that they are crystalline. The lower magnification TEM in Fig.41 shows that the particles aggregate in clusters of different sizes. The X-ray diffraction pattern in Fig.42 agrees well with the standard powder pattern of YSZ. The broadening of the peaks (top) is consistent with the small size of the particles. On annealing at 800 ^{o}C for 24 hours the peaks (bottom) narrow appreciably.

B. $SrCo_{0.8}Fe_{0.2}O_{3-\delta}$

The TEM in Fig.43 shows that the particles are in the range 100-250 Å. The X-ray diffraction pattern in Fig.44 shows peaks other than the standard powder pattern of $SrCo_{0.8}Fe_{0.2}O_{3-\delta}$. On annealing at 700 ^{o}C for 7 hours the cubic $SrCo_{0.8}Fe_{0.2}O_{3-\delta}$ peaks increase appreciably, but there still remains some other peaks. This problem needs yet to be solved.

C. Membrane fabrication

In order to fabricate the membrane shown in Fig.2a it is necessary to consolidate the particles into a porous mechanically stable film. Preliminary experiments indicate that annealing at 800

°C for 24 hours forms a rigid film that adheres well to the substrate. To form the left porous electrode in Fig.2a the particles are precipitated from solution on the porous alumina substrate and consolidated by annealing. A thin dense film is then deposited on top of the electrode to form the blocking layer and finally a second porous electrode is formed on right of the dense film. Annealing conditions for optimum consolidation, i.e. high porosity combined with sufficient mechanical strength and good adherence to the underlying surface, need yet to be determined.

Summary

We describe experimental techniques we developed for fabrication of dense thin solid oxide films in the thickness range 0.05-1 µm and porous electrodes consisting of oxide particles as small as 50-100 Å having surface areas 20 m^2/gm. Thin films and nano-scale particles of complex oxides YSZ (yttrium stabilized zirconia, ZrO_2 at 5.7 and 9.5 mol% of Y_2O_3) and $SrCo_{0.8}Fe_{0.2}O_{3-\delta}$ were fabricated by pulsed laser deposition (PLD). X-ray, SEM and TEM microscopy, electrical conductivity and optical transmission measurements were used to characterize the materials. The YSZ electrode interfacial impedance has the constant phase angle form. The conductivity of $SrCo_{0.8}Fe_{0.2}O_{3-\delta}$, which is due to a charge transfer conduction process, is temperature activated with an activation energy of 0.17 eV. The optical absorption spectra of $SrCo_{0.8}Fe_{0.2}O_{3-\delta}$ are interpreted in terms of an effective one-electron band structure theory.

For nano-scale materials of $SrCo_{0.8}Fe_{0.2}O_{3-\delta}$, the conditions of making the pure cubic structure and having high porosity combined with sufficient mechanical strength and good adherence to the underlying surface need yet to be determined.

Appendix A

It is convenient to express Eqs. (45) and (50) in vector notation:

$$\frac{d^2\bar{\mu}}{dx^2} = \tilde{M}\bar{\mu} \ , \tag{1A}$$

where the matrix $\tilde{M}$ and the vector $\bar{\mu}$ are defined by:

$$\tilde{M} = \begin{pmatrix} \frac{1}{Lp^2} & -\frac{1}{2Lp^2} \\ -\frac{2}{Lg^2} & \frac{1}{Lg^2} \end{pmatrix} ,$$

$$\bar{\mu} = \begin{pmatrix} \mu \\ \mu_g \end{pmatrix} .$$

To solve Eq. (1A) we perform the transformation:

$$\bar{\mu} = \tilde{\Psi}\bar{v} + \bar{h} \ , \tag{2A}$$

where

$$\bar{v} = \begin{pmatrix} v_1(x) \\ v_2(x) \end{pmatrix} ,$$

$$\bar{h}=\begin{pmatrix}\frac{1}{2}\mu''_g\\ \mu''_g\end{pmatrix},$$

and the elements of the matrix $\tilde{\Psi}$ are components of the eigenvectors $\overline{\Psi}_i$ defined by:

$$\tilde{M}\,\overline{\Psi}_i=\lambda_i\tilde{I}\ , \tag{3A}$$

$\tilde{I}$ is the unit matrix and λ_i are the eigenvalues determined from the secular equation:

$$|\tilde{M}-\lambda_i\tilde{I}|=0\ . \tag{4A}$$

The two roots of Eq. (4A) are:

$$\lambda_1=\frac{1}{L_m^{\ 2}}=\frac{1}{L_p^{\ 2}}+\frac{1}{L_g^{\ 2}}\ , \tag{5Aa}$$

$$\lambda_2=0\ , \tag{5Ab}$$

and the normalized eigenvectors $\overline{\Psi}_i$ and the matrix $\tilde{\Psi}$ are given by:

$$\overline{\Psi}_1=1/\sqrt{1+4\frac{L_p^{\ 4}}{L_g^{\ 4}}}\begin{pmatrix}1\\ -2L_p^{\ 2}/L_g^{\ 2}\end{pmatrix}, \tag{6Aa}$$

$$\overline{\Psi}_2=1/\sqrt{5}\begin{pmatrix}1\\ 2\end{pmatrix}, \tag{6Ab}$$

$$\tilde{\Psi}=\begin{pmatrix} 1/\sqrt{1+4\frac{L_p^4}{L_g^4}} & 1/\sqrt{5} \\ (-2\frac{L_p^2}{L_g^2})/\sqrt{1+4\frac{L_p^4}{L_g^4}} & 2/\sqrt{5} \end{pmatrix} . \tag{6Ac}$$

Substitution of Eq. (2A) in Eq. (1A) results:

$$\frac{d^2 v_1(x)}{dx^2}-\lambda_1 v_1(x)=0 , \tag{7Aa}$$

$$\frac{d^2 v_2(x)}{dx^2}=0 . \tag{7Ab}$$

The solutions to Eqs. (7A) are:

$$v_1(x)=g_{11}e^{-x/L_m}+g_{12}e^{x/L_m} , \tag{8Aa}$$

$$v_2(x)=g_{21}x+g_{22} , \tag{8Ab}$$

where g_{11}, g_{12}, g_{21} and g_{22} are integration constants.

Substituting Eqs. (8A) into Eq. (2A) yields the general solution given by Eqs. (52) and (53).

Substituting Eqs. (52) and (53) in Eqs. (55)-(58) yields four linear equations for the four integration constants:

$$\Psi_{11}g_{11}+\Psi_{11}g_{12}+\Psi_{12}g_{22}=\Delta\mu_g , \tag{9A}$$

$$\begin{aligned}&\frac{\Psi_{11}}{L_m}e^{-L/(2L_m)}(\tau_s L_m/L_d-1)g_{11}+\frac{\Psi_{11}}{L_m}e^{L/(2L_m)}(\tau_s L_m/L_d+1)g_{12}\\&+\Psi_{12}(\tau_s L/(2L_d)+1)g_{21}+\Psi_{12}(\tau_s/L_d)g_{22}=0\ ,\end{aligned}\tag{10A}$$

$$-\frac{\Psi_{21}}{L_m}g_{11}+\frac{\Psi_{21}}{L_m}g_{12}+\Psi_{22}g_{21}=0\ ,\tag{11A}$$

$$\Psi_{21}e^{-L/(2L_m)}g_{11}+\Psi_{21}e^{L/(2L_m)}g_{12}+(\Psi_{22}L/2)g_{21}+\Psi_{22}g_{22}=0.\tag{12A}$$

The solutions to the Eqs. (9A)-(12A) are:

$$g_{11}=\frac{\Delta\mu_g}{5}\frac{4}{\sqrt{1+4\frac{L_p^4}{L_g^4}}}\frac{1}{L_m}\{\frac{L_p^2}{L_g^2}+(1+\tau_s\frac{L_m}{L_d}+\tau_s\frac{L_m}{L_d}\frac{L_p^2}{L_g^2})e^{L/(2L_m)}\}/\Delta,\tag{13Aa}$$

$$g_{12}=-\frac{\Delta\mu_g}{5}\frac{4}{\sqrt{1+4\frac{L_p^4}{L_g^4}}}\frac{1}{L_m}\{(-1+\tau_s\frac{L_m}{L_d}+\tau_s\frac{L_m}{L_d}\frac{L_p^2}{L_g^2})e^{-L/(2L_m)}-\frac{L_p^2}{L_g^2}\}/\Delta,\tag{13Ab}$$

$$g_{21} = -\frac{\Delta\mu_g}{5}\frac{4\frac{L_p^2}{Lg^2}}{1+4\frac{L_p^4}{L_g^4}}\frac{1}{L_m^2}\{\tau_s\frac{L_m}{L_d}\frac{L_p^2}{L_g^2}(e^{L/(2L_m)}+e^{-L/(2L_m)})$$

$$[(1+\tau_s\frac{L_m}{L_d})e^{L/(2L_m)}+(-1+\tau_s\frac{L_m}{L_d})e^{-L/(2L_m)}]\}/\Delta, \qquad (13\text{Ac})$$

$$g_{22} = \frac{\Delta\mu_g}{5}\frac{4\frac{L_p^2}{Lg^2}}{1+4\frac{L_p^4}{L_g^4}}\frac{1}{L_m}\{(e^{L/(2L_m)}+e^{-L/(2L_m)})[(1+\tau_s\frac{L}{2L_d})\frac{L_p^2}{L_g^2}$$

$$-e^{-L/(2L_m)}(-1+\tau_s\frac{L_m}{L_d})]+[(1+\tau_s\frac{L_m}{L_d})e^{L/(2L_m)}$$

$$+(-1+\tau_s\frac{L_m}{L_d})e^{-L/(2L_m)}](\frac{L}{2L_m}+e^{-L/(2L_m)})\}/\Delta, \qquad (13\text{Ad})$$

where

$$\Delta = \frac{4}{5}\frac{1}{1+4\frac{L_p^4}{L_g^4}}\frac{1}{L_m}\{(e^{L/(2L_m)}+e^{-L/(2L_m)})\frac{L_p^2}{L_g^2}[(1+\tau_s\frac{L}{2L_d})\frac{L_p^2}{L_g^2}$$

$$+\tau_s\frac{L_m}{L_d}-(-1+\tau_s\frac{L_m}{L_d})\,e^{-L/(2L_m)})]+[e^{L/(2L_m)}(1+\tau_s\frac{L_m}{L_d})+e^{-L/(2L_m)}$$

$$(-1+\tau_s \frac{L_m}{L_d})][\frac{L}{2L_m}\frac{L_p{}^2}{L_g{}^2} + e^{-L/(2L_m)}\frac{L_p{}^2}{L_g{}^2}+1] - \tau_s \frac{L_m}{L_d}\frac{L_p{}^2}{L_g{}^2}$$

$$(\frac{L}{L_m} + 2e^{-L/(2L_m)}) + 2(1+\tau_s\frac{L}{2L_d}) + 2(1-\tau_s\frac{L_m}{L_d})e^{-L/(2L_m)}]\} \ . \tag{14A}$$

Appendix B

The ion and electron current densities I_i and I_e can be expressed as Eqs. (38) and (39). Assuming D_i and D_e do not depend on concentrations of c_i and n_e. Substituting Eqs. (38) and (39) in Eqs. (40) and (41) results:

$$\frac{1}{RT}\frac{d^2\mu_i}{dx^2}+\alpha\frac{1}{(RT)^2}(\frac{d\mu_i}{dx})^2+2\frac{d}{dx}(FE)=-\frac{\tau_s}{1-\phi}\frac{iS}{D_i c_i}\ , \tag{1B}$$

$$\frac{1}{RT}\frac{d^2\mu_e}{dx^2}+\beta\frac{1}{(RT)^2}(\frac{d\mu_e}{dx})^2+\frac{d}{dx}(FE)=\frac{\tau_s}{1-\phi}\frac{2iS}{D_e n_e}\ , \tag{2B}$$

where we have used Eqs. (69) and (70).

Eliminating d(FE)/dx in Eqs. (1B) and (2B), and assuming charge conservation condition $dn_e=-2dc_i$, we have:

$$\frac{d^2\mu_i}{dx^2}+\frac{\lambda_n}{RT}(\frac{d\mu_i}{dx})^2=\frac{1}{L_p^2}(\mu_i-\mu_{io}+\Delta\mu_g/\xi)\ , \tag{3B}$$

where the coefficient of second order term $(d\mu_i/dx)^2$ is:

$$\lambda_n=\alpha(1+\frac{4c_i}{n_e})/(1+\frac{4\alpha c_i}{\beta n_e})\ , \tag{4B}$$

and

$$\xi = (1+\frac{4\alpha c_i}{\beta n_e}) \ . \tag{5B}$$

Let $\tilde{\mu} = \frac{1}{RT}(\mu_i - \mu_{io} + \Delta\mu_g / \xi)$, Eq. (3B) can be rewritten in the form:

$$\frac{d^2\tilde{\mu}}{dx^2} + \lambda_n (\frac{d\tilde{\mu}}{dx})^2 = \frac{\tilde{\mu}}{L_p^2} \ . \tag{6B}$$

We can expand $\tilde{\mu}$ in term of λ_n, which is a small parameter of around 10^{-2}:

$$\tilde{\mu} = \tilde{\mu}^{(0)} + \lambda_n \tilde{\mu}^{(1)} + \lambda_n{}^2 \tilde{\mu}^{(2)} + \ \dots \ . \tag{7B}$$

Equation (6B) is then separated into a set of equations:

$$\frac{d^2\tilde{\mu}^{(0)}}{dx^2} = \frac{\tilde{\mu}^{(0)}}{L_p^2} \ , \qquad \text{for } o(\lambda_n{}^0) \tag{8B}$$

$$\frac{d^2\tilde{\mu}^{(1)}}{dx^2} + (\frac{d\tilde{\mu}^{(0)}}{dx})^2 = \frac{\tilde{\mu}^{(1)}}{L_p^2} \ , \qquad \text{for } o(\lambda_n{}^1) \tag{9B}$$

....

the boundary conditions are separated as:

$$\tilde{\mu}^{(0)} = \Delta\mu_g / \xi \ , \qquad x=0 \tag{10B}$$

$$\frac{d\tilde{\mu}^{(0)}}{dx} = -\frac{\tau_s}{L_d}\tilde{\mu}^{(0)} , \qquad x=L/2 \qquad (11B)$$

$$\tilde{\mu}^{(1)} = 0 , \qquad x=0 \qquad (12B)$$

$$\frac{d\tilde{\mu}^{(1)}}{dx} = 0 . \qquad x=L/2 \qquad (13B)$$

The solution of Eq. (8B) is:

$$\tilde{\mu}^{(0)} = Ae^{-x/L_p} + Be^{x/L_p} , \qquad (14B)$$

where A and B are determined by boundary conditions Eqs. (10B) and (11B):

$$A = \frac{\Delta\mu_g}{\xi}\frac{ae^{L/L_p}}{1+ae^{L/L_p}} , \qquad (15B)$$

$$B = \frac{\Delta\mu_g}{\xi}\frac{1}{1+ae^{L/L_p}} . \qquad (16B)$$

Substituting Eq. (14B) in Eq. (9B), we have:

$$\frac{d^2\tilde{\mu}^{(1)}}{dx^2} = \frac{\tilde{\mu}^{(1)}}{L_p^{\,2}} - \frac{1}{L_p^{\,2}}(A^2e^{-2x/L_p} + B^2e^{x/L_p} - 2AB) . \qquad (17B)$$

The solution of Eq. (17B) is:

$$\tilde{\mu}^{(1)} = P_0 + P_1 e^{-2x/L_p} + P_2 e^{2x/L_p} + P_3 e^{-x/L_p} + P_4 e^{x/L_p} , \qquad (18B)$$

where

$$P_0 = -2AB , \qquad P_1 = -A^2/3 , \qquad P_2 = -B^2/3 .$$

P_3 and P_4 are determined by boundary conditions Eqs. (12B) and (13B):

$$P_3 = \frac{P_0 + P_1(1-2e^{-L/2L_p}) + P_2(1+2e^{-3L/2L_p})}{1+e^{L/L_p}} - P_0 - P_1 - P_2 , \qquad (19B)$$

$$P_4 = -\frac{P_0 + P_1(1-2e^{-L/2L_p}) + P_2(1+2e^{-3L/2L_p})}{1+e^{L/L_p}} . \qquad (20B)$$

For the case of $L \gg L_p$:

$$\left.\frac{d\tilde{\mu}}{dx}\right|_{x=0} \approx \left[\frac{d\tilde{\mu}^{(0)}}{dx} + \lambda_n \frac{d\tilde{\mu}^{(1)}}{dx}\right]_{x=0} = -\frac{A}{L_p}(1-\frac{\lambda_n A}{3}) , \qquad (21B)$$

where A/L_p is the linear contribution to the flux and $(A/L_p)(\lambda_n A/3)$ is that of $(\lambda_n/RT)(d\mu_i/dx)^2$ term:

$$\frac{1}{3}\lambda_n A = \frac{1}{3}\alpha\frac{\Delta\mu_g}{\xi}\frac{(1+\frac{4c_i}{n_e})}{(1+\frac{4\alpha c_i}{\beta n_e})} << 1 \; . \tag{22B}$$

So that the contribution of second order term $(\lambda_n/RT)(d\mu_i/dx)^2$ to the flux is negligible.

Appendix C

We express Eqs. (72) and (73) in vector notation:

$$\frac{d^2\bar{\mu}}{dx^2} = \tilde{M}\bar{\mu} + \bar{m} \ , \qquad (1C)$$

where the matrix $\tilde{M}$, vectors $\bar{\mu}$ and $\bar{m}$ are defined by:

$$\tilde{M} = \begin{pmatrix} G & H \\ \bar{G} & \bar{H} \end{pmatrix} ,$$

$$\bar{\mu} = \begin{pmatrix} \bar{\mu}_i \\ \bar{\mu}_e \end{pmatrix} ,$$

$$\bar{m} = \begin{pmatrix} M \\ \bar{M} \end{pmatrix} .$$

To solve Eq. (1C) we perform the transformation:

$$\bar{\mu} = \tilde{\Psi}\,\bar{v} + \bar{h} \ , \qquad (2C)$$

where

$$\bar{v} = \begin{pmatrix} v_1(x) \\ v_2(x) \end{pmatrix} ,$$

$$\bar{h} = \begin{pmatrix} H_1 \\ H_2 \end{pmatrix} ,$$

and the elements of the matrix $\tilde{\Psi}$ are components of the eigenvectors $\overline{\Psi}_i$ defined by:

$$\tilde{M}\,\overline{\Psi}_i = \lambda_i \tilde{I} \ , \tag{3C}$$

where $\tilde{I}$ is the unit matrix and λ_i are the eigenvalues determined from the secular equation:

$$|\tilde{M} - \lambda_i \tilde{I}| = 0 \ . \tag{4C}$$

The two roots of Eq. (4C) are:

$$\lambda_1 = \frac{1}{L_1^2} = \frac{G+\overline{H}}{2} + \sqrt{\left(\frac{G+\overline{H}}{2}\right)^2 - (G\overline{H} - H\overline{G})} \ , \tag{5Ca}$$

$$\lambda_2 = \frac{1}{L_2^2} = \frac{G+\overline{H}}{2} - \sqrt{\left(\frac{G+\overline{H}}{2}\right)^2 - (G\overline{H} - H\overline{G})} \ , \tag{5Cb}$$

and the normalized eigenvectors $\overline{\Psi}_i$ and the matrix $\tilde{\Psi}$ are given by:

$$\Psi_{11} = H / \sqrt{H^2 + (\lambda_1 - G)^2} \ , \tag{6Ca}$$

$$\Psi_{12} = (\lambda_1 - G) / \sqrt{H^2 + (\lambda_1 - G)^2} \ , \tag{6Cb}$$

$$\Psi_{21} = H / \sqrt{H^2 + (\lambda_2 - G)^2} \ , \tag{6Cc}$$

$$\Psi_{22} = (\lambda_2 - G) / \sqrt{H^2 + (\lambda_2 - G)^2} \ , \qquad \text{(6Cd)}$$

$$\tilde{\Psi} = \begin{pmatrix} \Psi_{11} & \Psi_{12} \\ \Psi_{21} & \Psi_{22} \end{pmatrix} . \qquad \text{(7C)}$$

Substitution of Eq. (2C) in Eq. (1C) results:

$$\frac{d^2 v_1(x)}{dx^2} - \lambda_1 v_1(x) = 0 \ , \qquad \text{(8Ca)}$$

$$\frac{d^2 v_2(x)}{dx^2} - \lambda_2 v_2(x) = 0 \ , \qquad \text{(8Cb)}$$

$$\tilde{M}\bar{h} - \bar{m} = 0 \ . \qquad \text{(8Cc)}$$

The solutions to Eqs. (8C) are:

$$v_1(x) = g_{11} e^{-x/L_1} + g_{12} e^{x/L_1} \ , \qquad \text{(9Ca)}$$

$$v_2(x) = g_{21} e^{-x/L_2} + g_{22} e^{x/L_2} \ , \qquad \text{(9Cb)}$$

$$\begin{pmatrix} H_1 \\ H_2 \end{pmatrix} = \frac{1}{(H\bar{G} - G\bar{H})} \begin{pmatrix} \bar{H}M - H\bar{M} \\ G\bar{M} - \bar{G}M \end{pmatrix} , \qquad \text{(9Cc)}$$

where g_{11}, g_{12}, g_{21} and g_{22} are integration constants.

Substituting Eqs. (9C) in Eq. (2C) yields the general solution given by Eqs. (75) and (76).

Substituting Eqs. (75) and (76) in Eqs. (77)-(80) yields four linear equations for the four integration constants:

$$\Psi_{11}g_{11} + \Psi_{11}g_{12} + \Psi_{12}g_{21} + \Psi_{12}g_{22} = -H_1 , \tag{10C}$$

$$\Psi_{21}g_{11} + \Psi_{21}g_{12} + \Psi_{22}g_{21} + \Psi_{22}g_{22} = -H_2 , \tag{11C}$$

$$K_1 g_{11} + K_2 g_{12} + K_3 g_{21} + K_4 g_{22} = 0 , \tag{12C}$$

$$K_5 g_{11} + K_6 g_{12} + K_7 g_{21} + K_8 g_{22} = 0 , \tag{13C}$$

where

$$K_1 = e^{-L/(2L_1)}(D_i \Psi_{11} / L_1 - K\Psi_{11} + 2K\Psi_{21}) ,$$

$$K_2 = e^{L/(2L_1)}(-D_i \Psi_{11} / L_1 - K\Psi_{11} + 2K\Psi_{21}) ,$$

$$K_3 = e^{-L/(2L_2)}(D_i \Psi_{12} / L_2 - K\Psi_{12} + 2K\Psi_{22}) ,$$

$$K_4 = e^{L/(2L_2)}(-D_i \Psi_{12} / L_2 - K\Psi_{12} + 2K\Psi_{22}) ,$$

$$K_5 = e^{-L/(2L_1)}(D_i c_i \Psi_{11} + D_e n_e \Psi_{21} / 2) / L_1 ,$$

$$K_6 = -e^{L/(2L_1)}(D_i c_i \Psi_{11} + D_e n_e \Psi_{21} / 2) / L_1 ,$$

$$K_7 = e^{-L/(2L_2)}(D_i c_i \Psi_{12} + D_e n_e \Psi_{22}/2)/L_2 \,,$$

$$K_8 = -e^{L/(2L_2)}(D_i c_i \Psi_{12} + D_e n_e \Psi_{22}/2)/L_2 \,.$$

The solutions to the Eqs. (10C)-(13C) are:

$$\begin{aligned} g_{11} = \{ & -(K_4 - K_3)[(\Psi_{22}K_6 - \Psi_{21}K_7)H_1 + (\Psi_{11}K_7 - \Psi_{12}K_6)H_2] \\ & +(K_8 - K_7)[(\Psi_{22}K_2 - \Psi_{21}K_3)H_1 + (\Psi_{11}K_3 - \Psi_{12}K_2)H_2 \\ & +(\Psi_{11}\Psi_{22} - \Psi_{12}\Psi_{21})H_3]\}/\Delta \,, \end{aligned} \tag{15Ca}$$

$$\begin{aligned} g_{12} = \{ & -(K_4 - K_3)[(\Psi_{21}K_7 - \Psi_{22}K_5)H_1 + (\Psi_{12}K_5 - \Psi_{11}K_7)H_2] \\ & +(K_8 - K_7)[(\Psi_{21}K_3 - \Psi_{22}K_1)H_1 + (\Psi_{12}K_1 - \Psi_{11}K_3)H_2 \\ & -(\Psi_{11}\Psi_{22} - \Psi_{12}\Psi_{21})H_3]\}/\Delta \,, \end{aligned} \tag{15Cb}$$

$$\begin{aligned} g_{21} = \{ & -(K_2 - K_1)[(\Psi_{21}K_8 - \Psi_{22}K_5)H_1 + (\Psi_{12}K_5 - \Psi_{11}K_8)H_2] \\ & +(K_6 - K_5)[(\Psi_{21}K_4 - \Psi_{22}K_1)H_1 + (\Psi_{12}K_1 - \Psi_{11}K_4)H_2 \\ & -(\Psi_{11}\Psi_{22} - \Psi_{12}\Psi_{21})H_3]\}/\Delta \,, \end{aligned} \tag{15Cc}$$

$$g_{22} = \{-(K_2 - K_1)[(\Psi_{22}K_5 - \Psi_{21}K_7)H_1 + (\Psi_{11}K_7 - \Psi_{12}K_5)H_2]$$

$$+(K_6-K_5)[(\Psi_{22}K_1-\Psi_{21}K_3)H_1+(\Psi_{11}K_3-\Psi_{12}K_1)H_2$$

$$+(\Psi_{11}\Psi_{22}-\Psi_{12}\Psi_{21})H_3]\}/\Delta\ , \tag{15Cd}$$

where

$$\Delta=(\Psi_{12}\Psi_{21}-\Psi_{11}\Psi_{22})[(K_2-K_1)(K_8-K_7)-(K_4-K_3)(K_6-K_5)]\ . \tag{16C}$$

The constants K_1-K_{12} in Eqs. (93)-(95) are:

$$K_1=e^{-L/(2L_1)}[K(\Psi_{11}-2\Psi_{21})-D_i(\frac{\Psi_{11}}{L_1}-\frac{8\pi F^2L_1}{\varepsilon RT}A_3)]-2D_iA_1\ ,$$

$$K_2=e^{L/(2L_1)}[K(\Psi_{11}-2\Psi_{21})+D_i(\frac{\Psi_{11}}{L_1}-\frac{8\pi F^2L_1}{\varepsilon RT}A_3)]+2D_iA_1\ ,$$

$$K_3=e^{-L/(2L_2)}[K(\Psi_{12}-2\Psi_{22})-D_i(\frac{\Psi_{11}}{L_2}-\frac{8\pi F^2L_2}{\varepsilon RT}A_4)]-2D_iA_2\ ,$$

$$K_4=e^{L/(2L_2)}[K(\Psi_{12}-2\Psi_{22})+D_i(\frac{\Psi_{11}}{L_2}-\frac{8\pi F^2L_2}{\varepsilon RT}A_4)]+2D_iA_2\ ,$$

$$K_5=\frac{4\pi FL_1{}^2}{\varepsilon}A_3(1-e^{-L/(2L_1)})-Fr(1-\phi)D_ic_i(2A_1+A_5)-\frac{L}{2}\frac{RT}{F}A_1\ ,$$

$$K_6=\frac{4\pi FL_1{}^2}{\varepsilon}A_3(1-e^{L/(2L_1)})+Fr(1-\phi)D_ic_i(2A_1+A_5)+\frac{L}{2}\frac{RT}{F}A_1\ ,$$

$$K_7 = \frac{4\pi F {L_2}^2}{\varepsilon} A_4 (1 - e^{-L/(2L_2)}) - Fr(1-\phi) D_i c_i (2A_2 + A_6) - \frac{L}{2}\frac{RT}{F} A_2 ,$$

$$K_7 = \frac{4\pi F {L_2}^2}{\varepsilon} A_4 (1 - e^{L/(2L_2)}) + Fr(1-\phi) D_i c_i (2A_2 + A_6) + \frac{L}{2}\frac{RT}{F} A_2 ,$$

$$K_9 = (D_e n_e A_1 - 2 D_i c_i A_5)(1 - e^{-L/(2L_1)}) ,$$

$$K_{10} = -(D_e n_e A_1 - 2 D_i c_i A_5)(1 - e^{L/(2L_1)}) ,$$

$$K_{11} = (D_e n_e A_2 - 2 D_i c_i A_6)(1 - e^{-L/(2L_2)}) ,$$

$$K_{12} = -(D_e n_e A_2 - 2 D_i c_i A_6)(1 - e^{L/(2L_2)}) .$$

The solutions of the coefficients g_{11}, g_{12}, g_{21}, g_{22} to the Eqs. (92)-(95) are:

$$g_{11} = H_1[(K_7 - K_8)(K_{10}K_3 - K_{11}K_2) + (K_{11} - K_{12})(K_2K_7 - K_3K_6)$$

$$+(K_3 - K_4)(K_{11}K_6 - K_7K_{10})]/\Delta , \qquad (17Ca)$$

$$g_{12} = H_1[(K_8 - K_7)(K_9K_3 - K_{11}K_1) + (K_{12} - K_{11})(K_1K_7 - K_3K_5)$$

$$+(K_4 - K_3)(K_{11}K_5 - K_7K_9)]/\Delta , \qquad (17Cb)$$

$$g_{21} = H_1[(K_9 - K_{10})(K_4K_5 - K_1K_8) + (K_1 - K_2)(K_9K_8 - K_{12}K_5)$$

$$+(K_5-K_6)(K_1K_{12}-K_4K_9)]/\Delta\ , \tag{17Cc}$$

$$g_{22}=H_1[(K_{10}-K_9)(K_3K_5-K_1K_7)+(K_2-K_1)(K_9K_7-K_{11}K_5)$$

$$+(K_6-K_5)(K_1K_{11}-K_3K_9)]/\Delta\ , \tag{17Cd}$$

where

$$\Delta=[(K_{10}-K_9)(K_8-K_7)-(K_{12}-K_{11})(K_6-K_5)](\Psi_{11}K_3-\Psi_{12}K_1)$$

$$+[(K_2-K_1)(K_{12}-K_{11})-(K_4-K_3)(K_{10}-K_9)](\Psi_{11}K_7-\Psi_{12}K_5)$$

$$+[(K_4-K_3)(K_6-K_5)-(K_2-K_1)(K_8-K_7)](\Psi_{11}K_{11}-\Psi_{12}K_9)\ . \tag{18C}$$

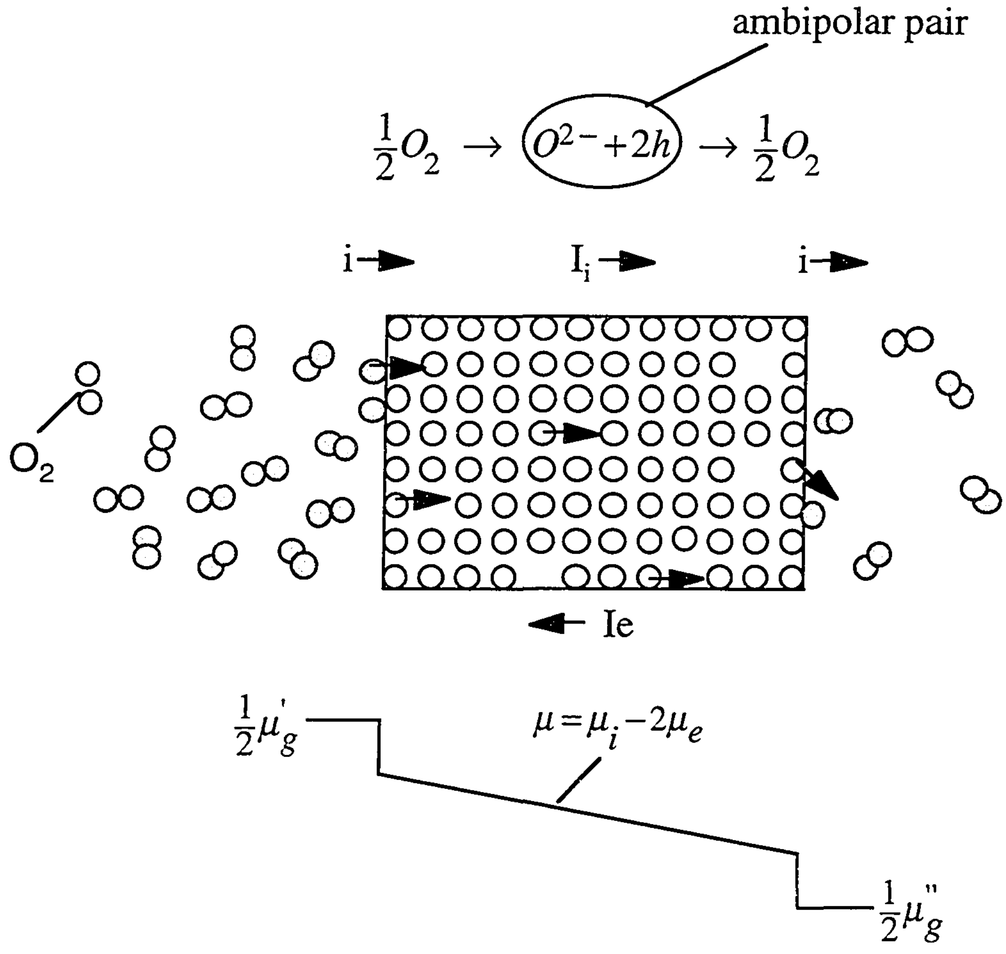
ambipolar pair
$\frac{1}{2}O_2 \rightarrow (O^{2-}+2h) \rightarrow \frac{1}{2}O_2$
i
I_i
i
O_2
Ie
$\frac{1}{2}\mu_g'$
$\mu=\mu_i-2\mu_e$
$\frac{1}{2}\mu_g''$

Figure 1

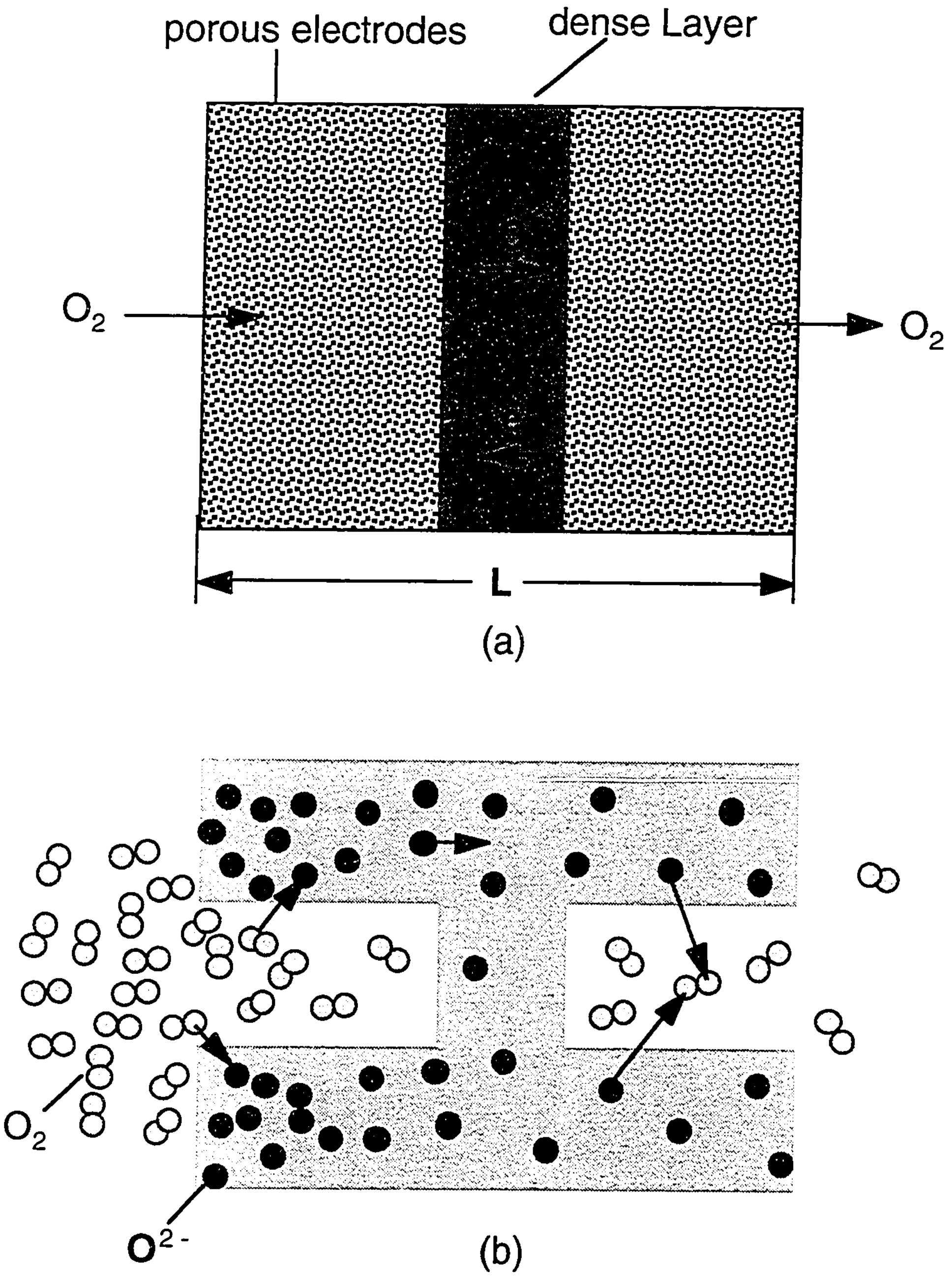

(a)

(b)

Figure 2

Solid Oxide Fuel Cell

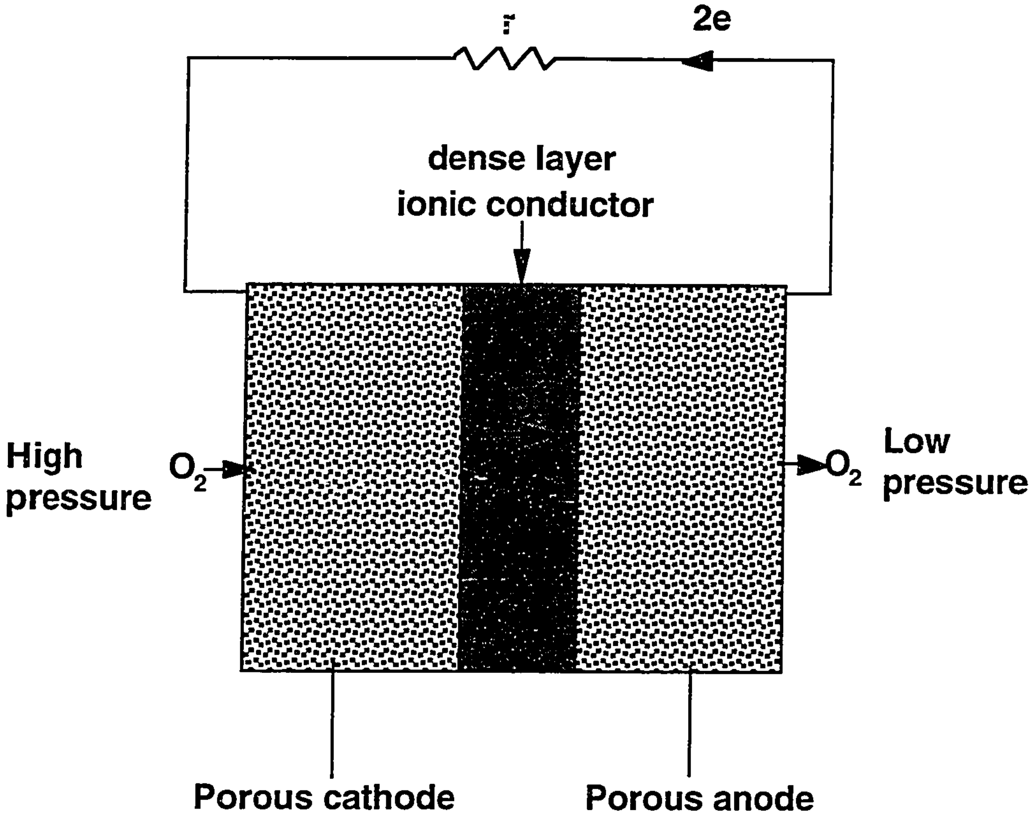

Figure 3

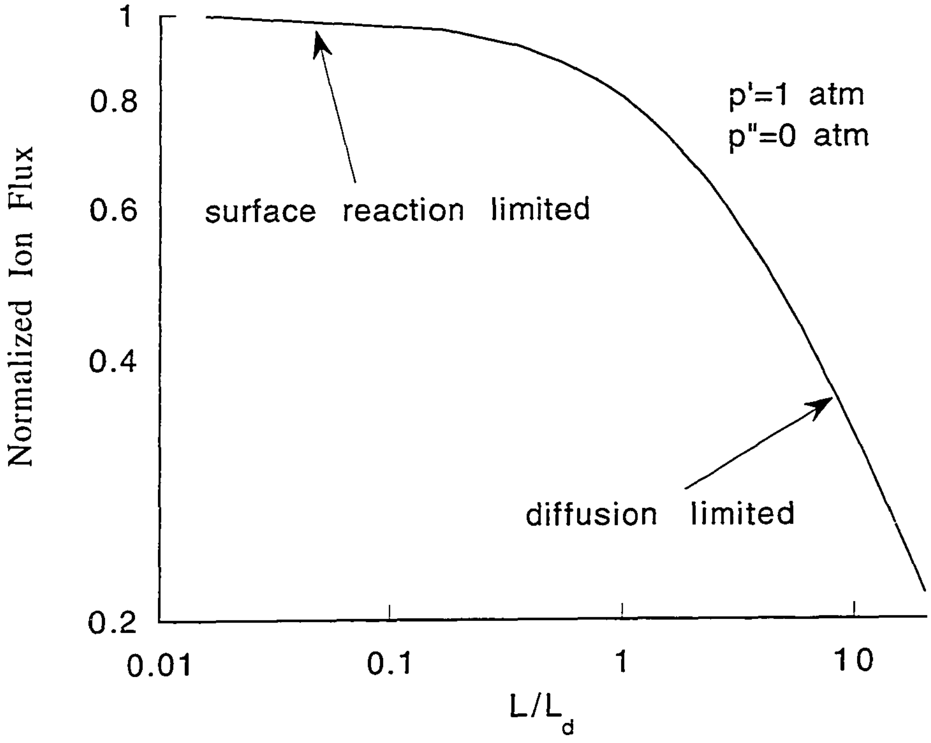
Normalized Ion Flux
1
0.8
0.6
0.4
0.2
0.01
0.1
1
10
L/L$_d$
p'=1 atm
p"=0 atm
surface reaction limited
diffusion limited

Figure 4

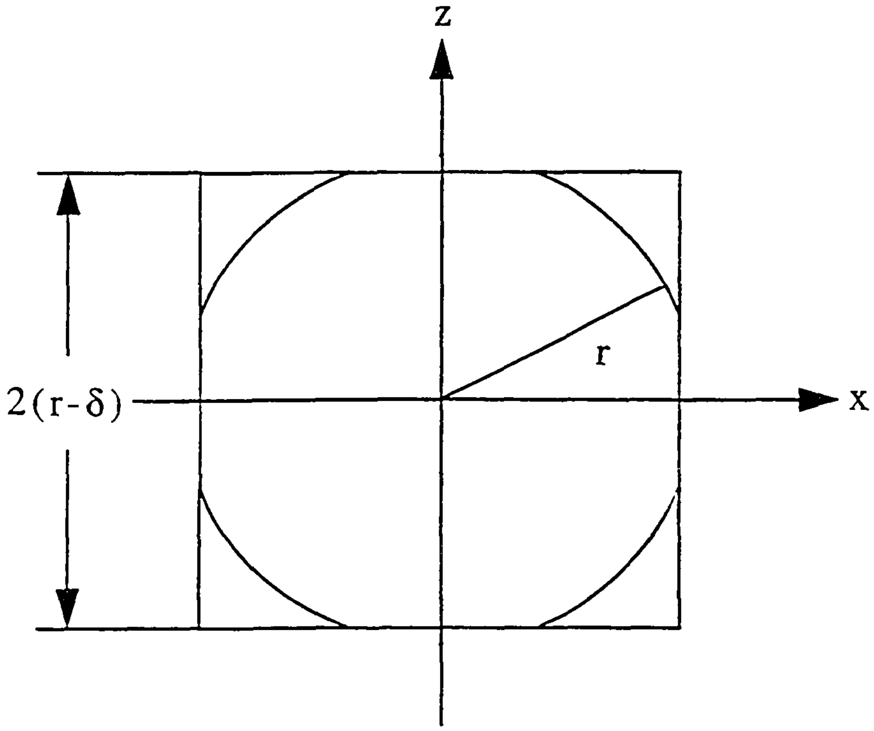

Figure 5

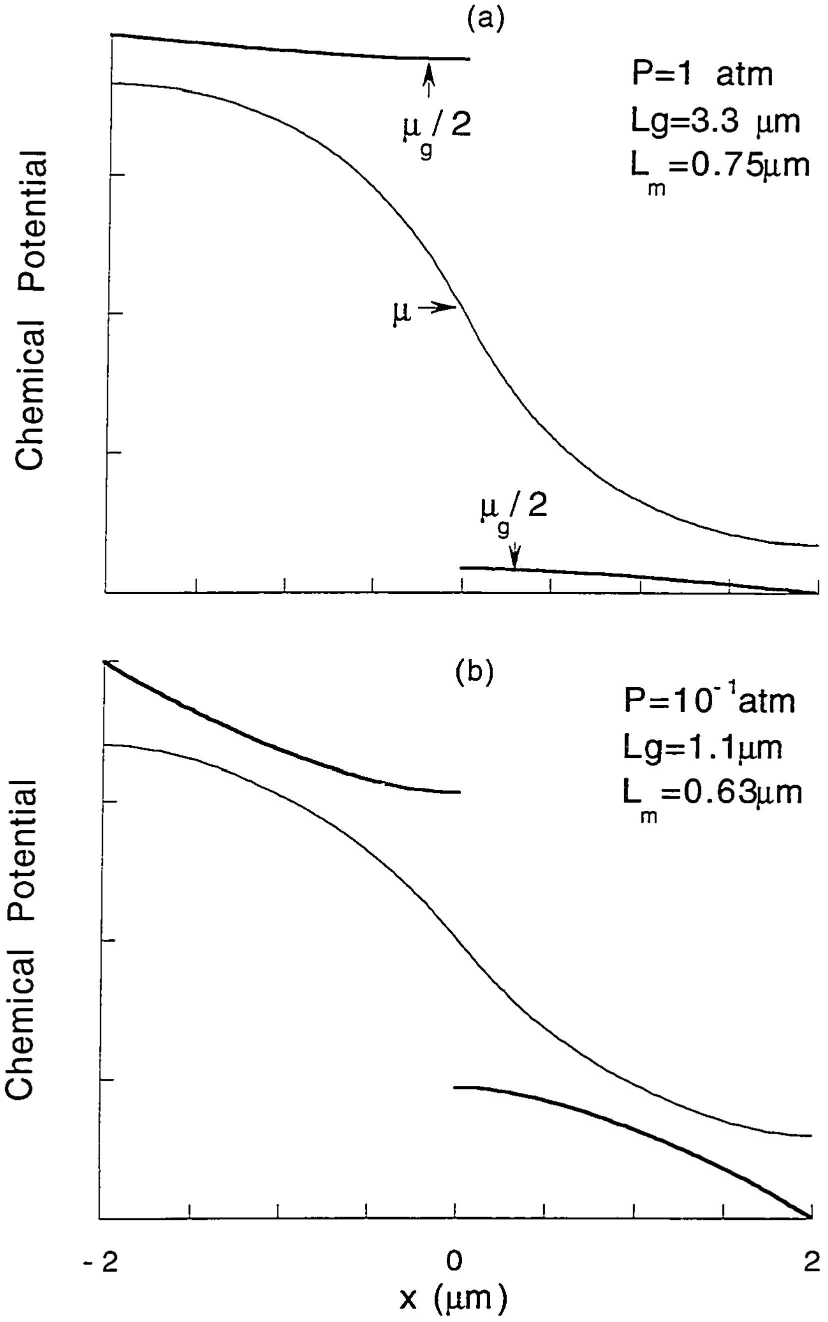
(a)
P=1 atm
Lg=3.3 μm
L_m=0.75μm
μ_g/2
μ
μ_g/2
Chemical Potential
(b)
P=10^-1atm
Lg=1.1μm
L_m=0.63μm
Chemical Potential
-2
0
2
x (μm)

Figure 6ab

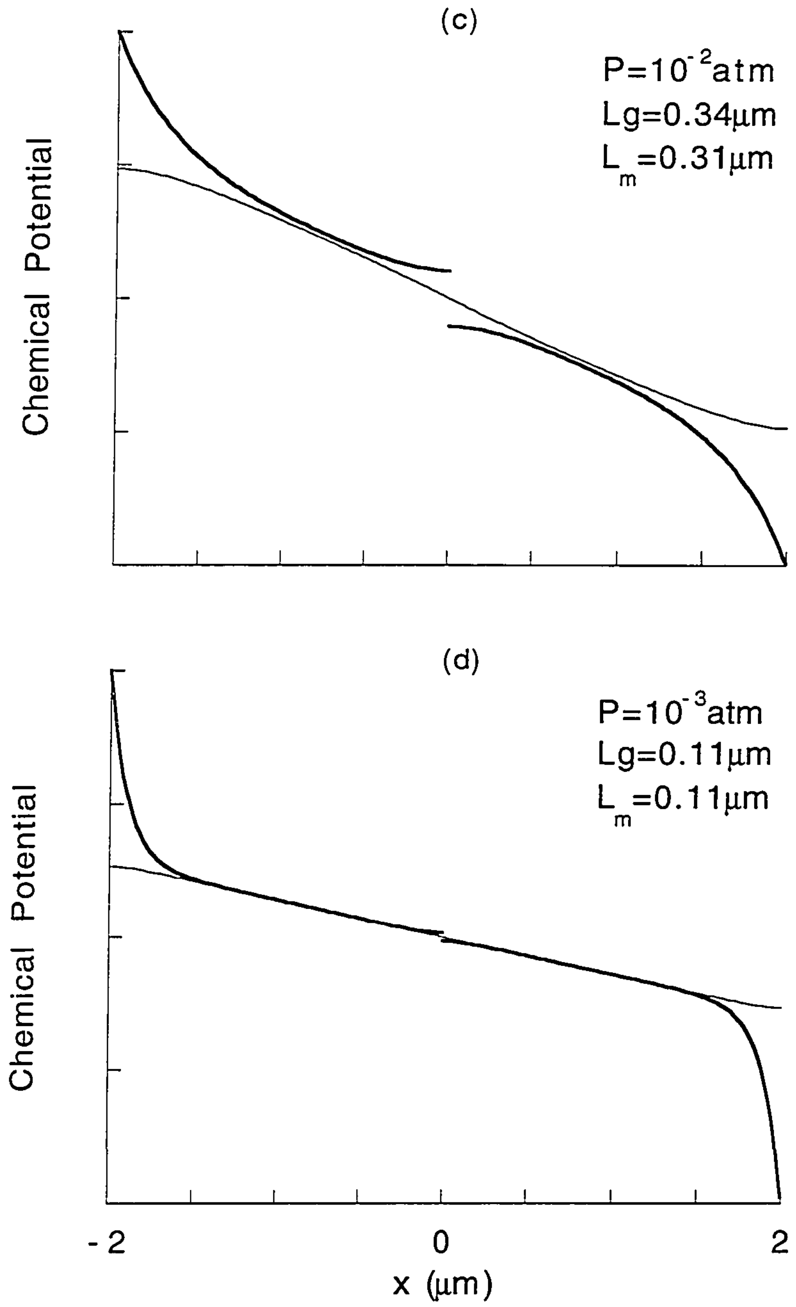
(c)
P=10⁻²atm
Lg=0.34µm
Lm=0.31µm
Chemical Potential
(d)
P=10⁻³atm
Lg=0.11µm
Lm=0.11µm
Chemical Potential
-2
0
2
x (µm)

Figure 6cd

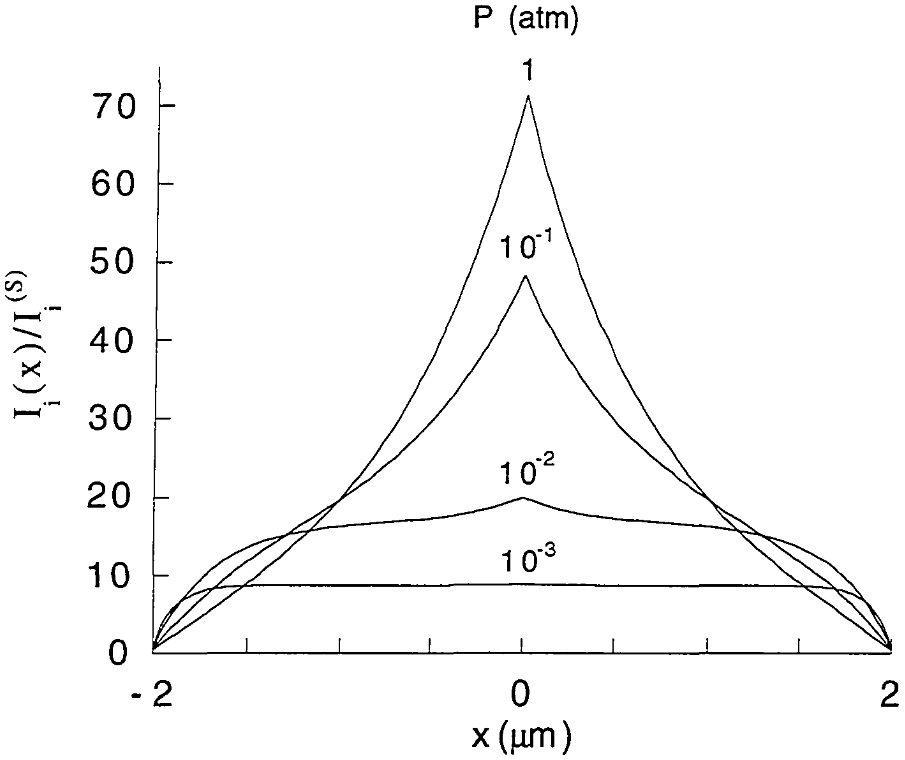

Figure 7

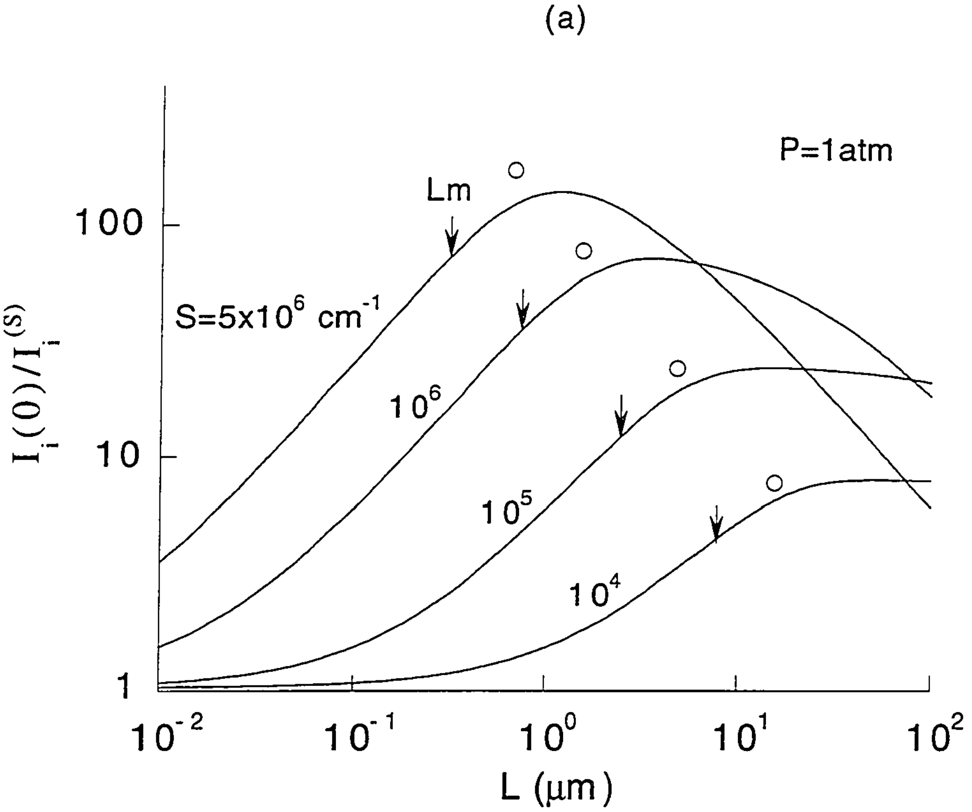
(a)
P=1atm
Lm
S=5x10^6 cm^{-1}
10^6
10^5
10^4
100
10
1
$I_i(0)/I_i^{(S)}$
10^{-2}
10^{-1}
10^0
10^1
10^2
L (μm)

Figure 8a

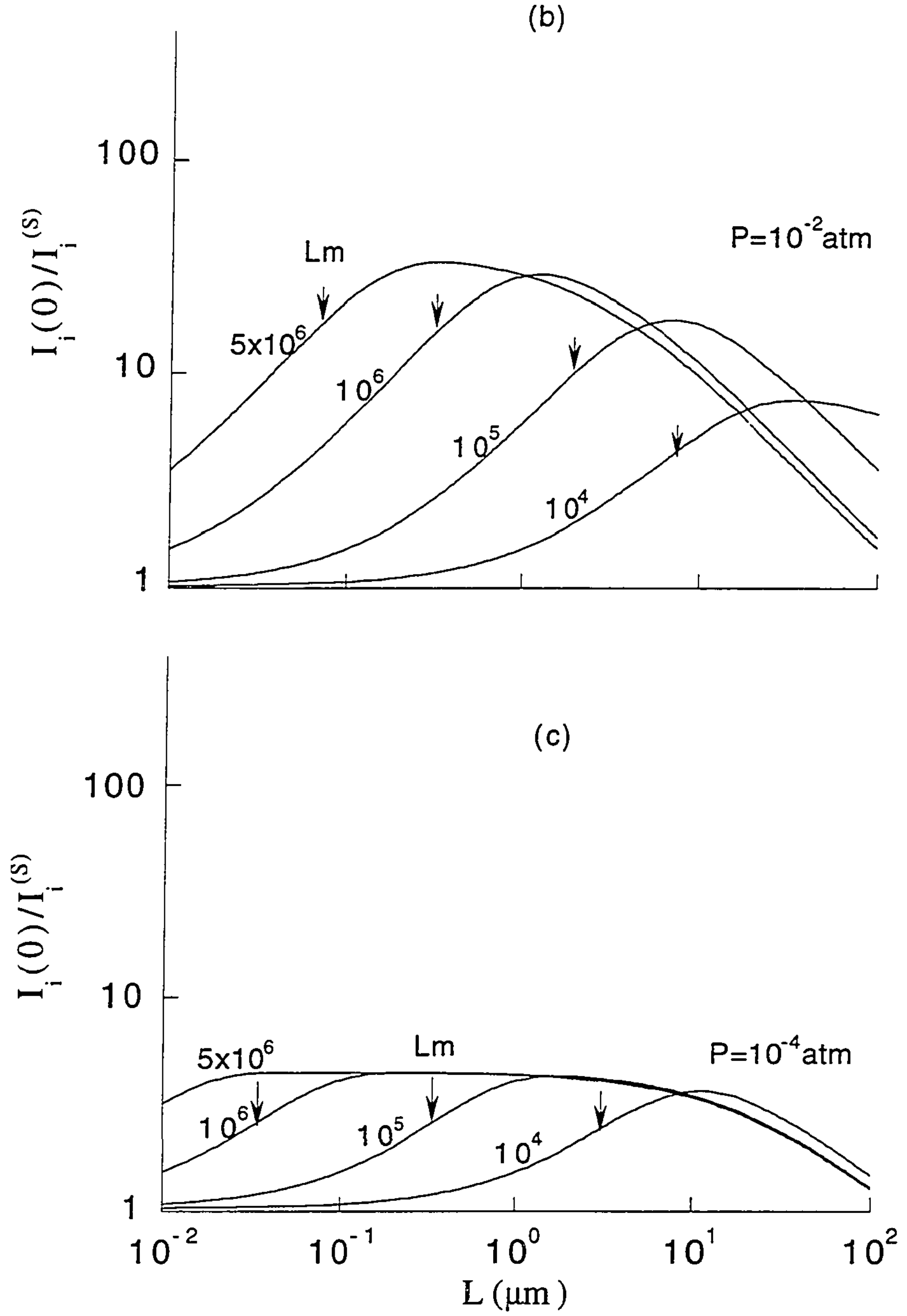
(b)
100
10
1
$I_i(0)/I_i^{(S)}$
Lm
5x10^6
10^6
10^5
10^4
P=10^{-2}atm
(c)
100
10
1
$I_i(0)/I_i^{(S)}$
5x10^6
Lm
10^6
10^5
10^4
P=10^{-4}atm
10^{-2}
10^{-1}
10^0
10^1
10^2
L (μm)

Figure 8bc

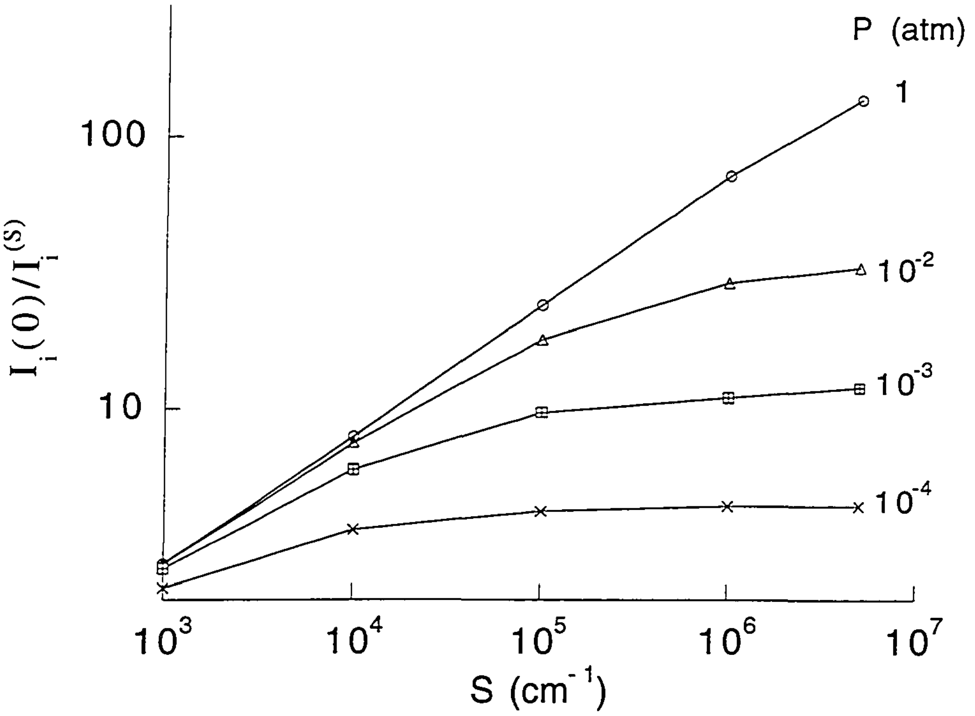

Figure 9

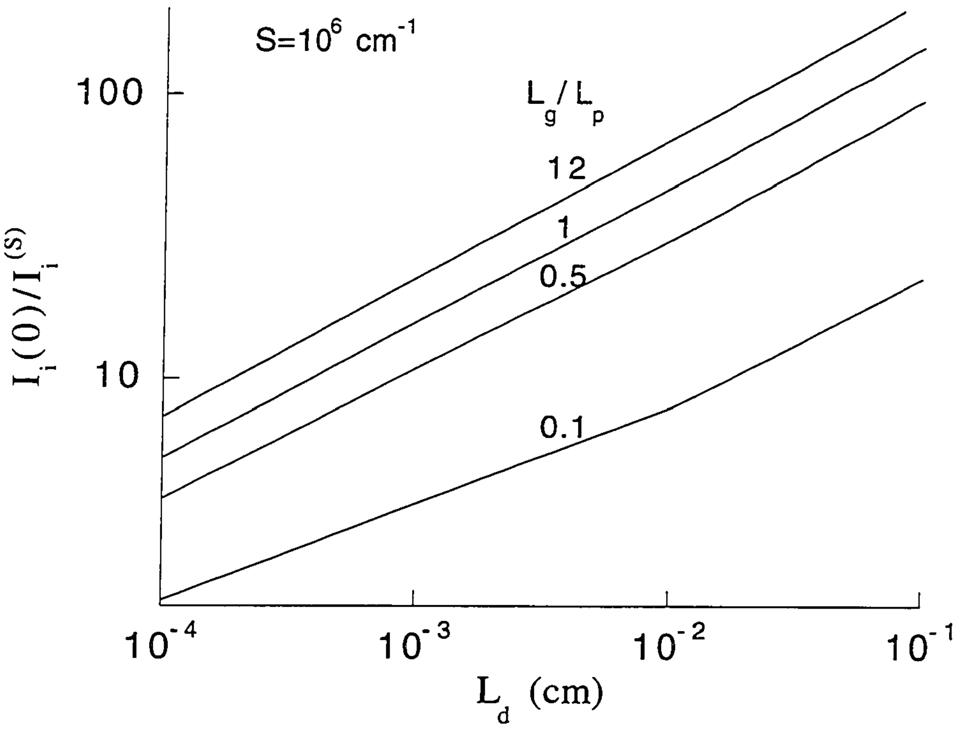

Figure 10

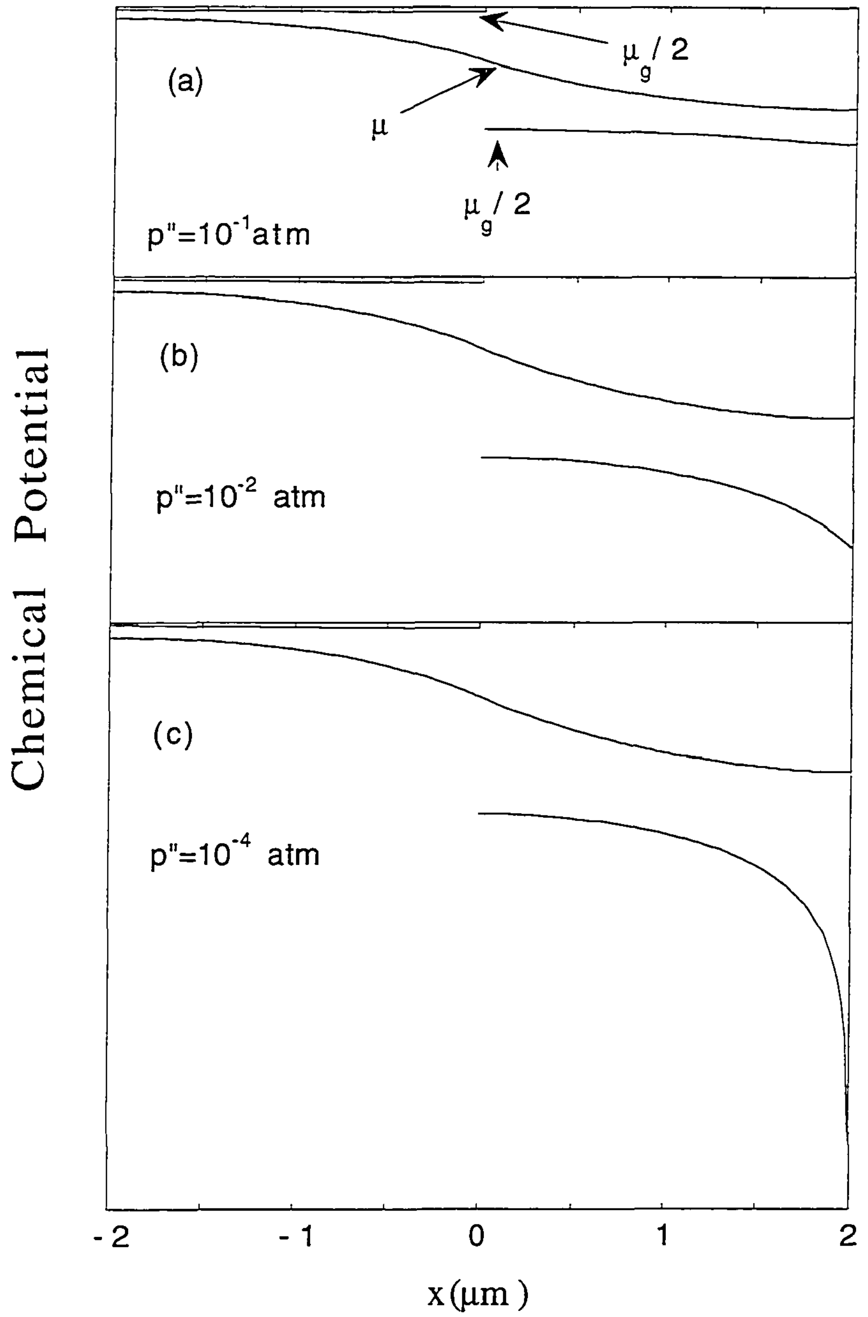
(a)
$\mu_g/2$
μ
$\mu_g/2$
p"=10^{-1}atm
(b)
p"=10^{-2} atm
(c)
p"=10^{-4} atm
Chemical Potential
-2
-1
0
1
2
x(μm)

Figure 11

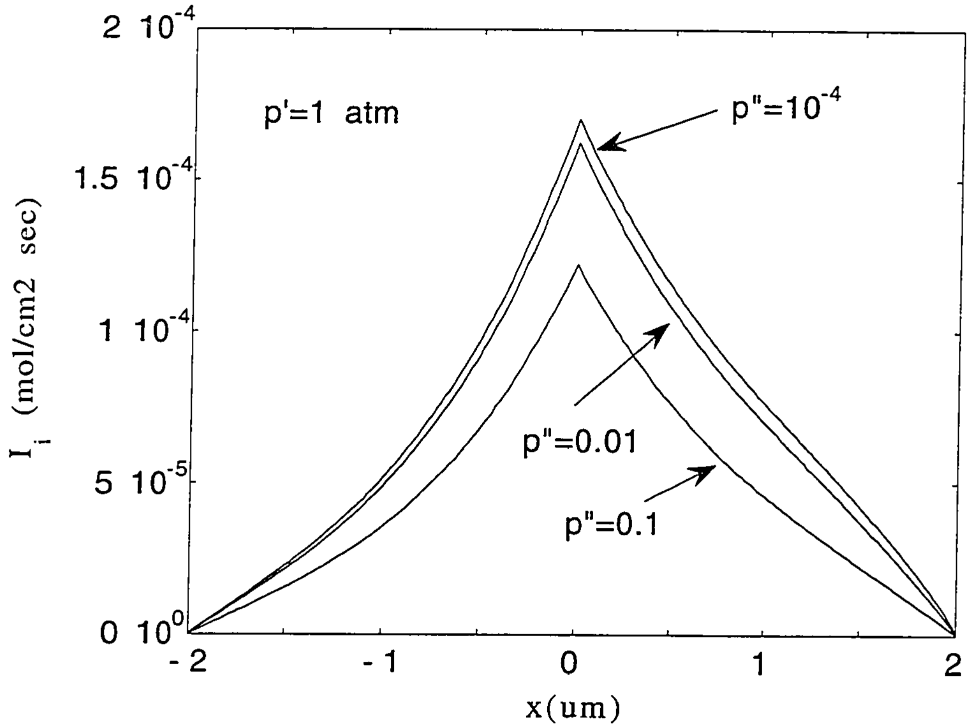

2 10^-4
1.5 10^-4
1 10^-4
5 10^-5
0 10^0
I_i (mol/cm2 sec)
-2
-1
0
1
2
x(um)
p'=1 atm
p"=10^-4
p"=0.01
p"=0.1

Figure 12

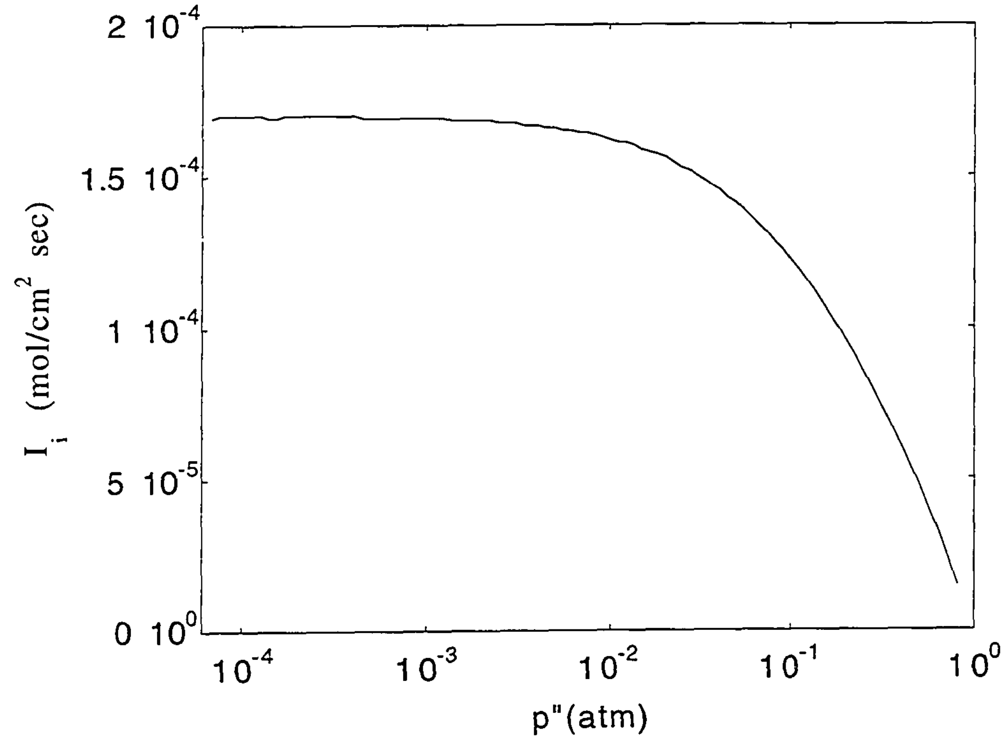
2 10^-4
1.5 10^-4
1 10^-4
5 10^-5
0 10^0
I_i (mol/cm^2 sec)
10^-4
10^-3
10^-2
10^-1
10^0
p"(atm)

Figure 13

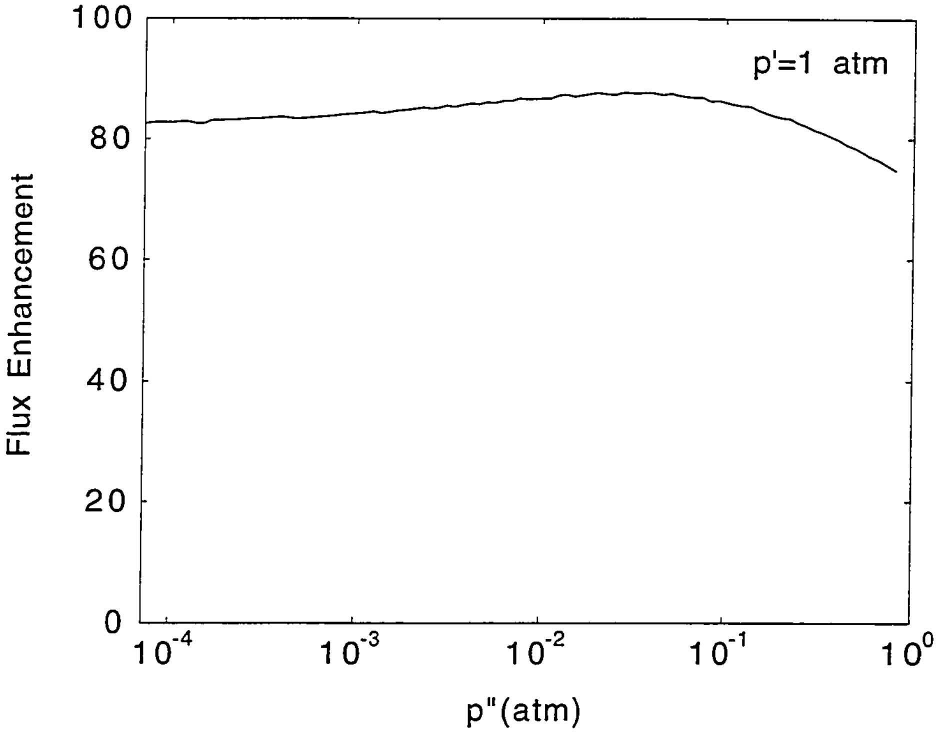
100
80
60
40
20
0
Flux Enhancement
p'=1 atm
10^{-4}
10^{-3}
10^{-2}
10^{-1}
10^{0}
p"(atm)

Figure 14

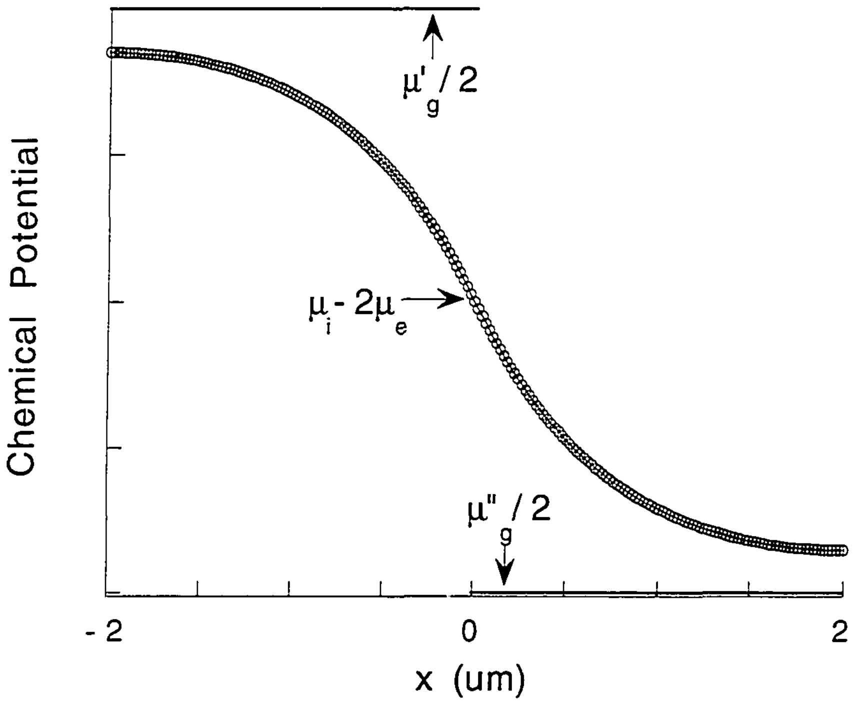

Figure 15

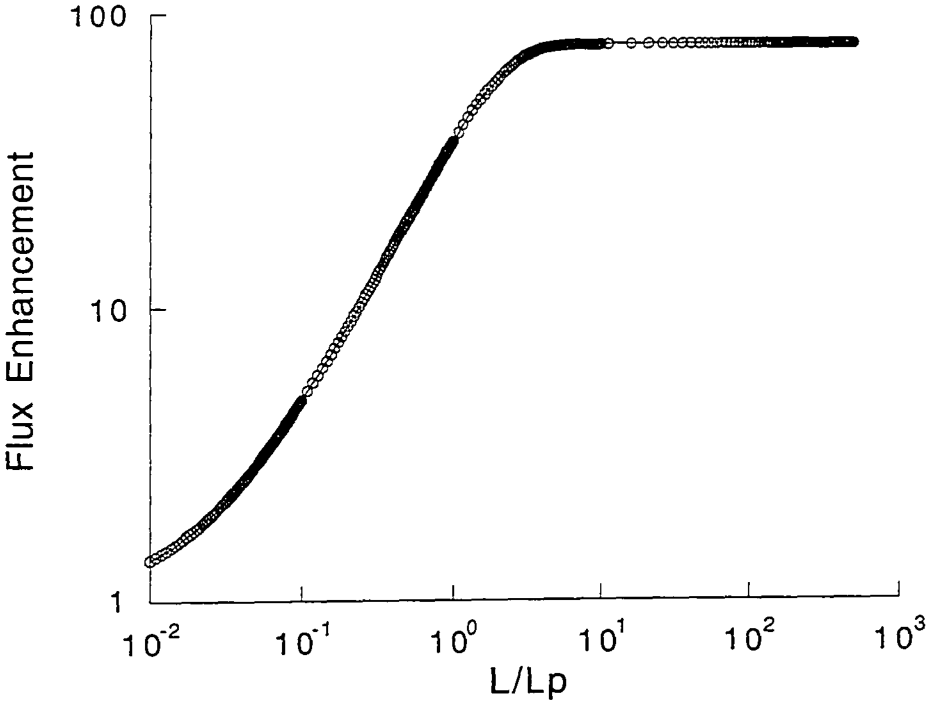

Figure 16

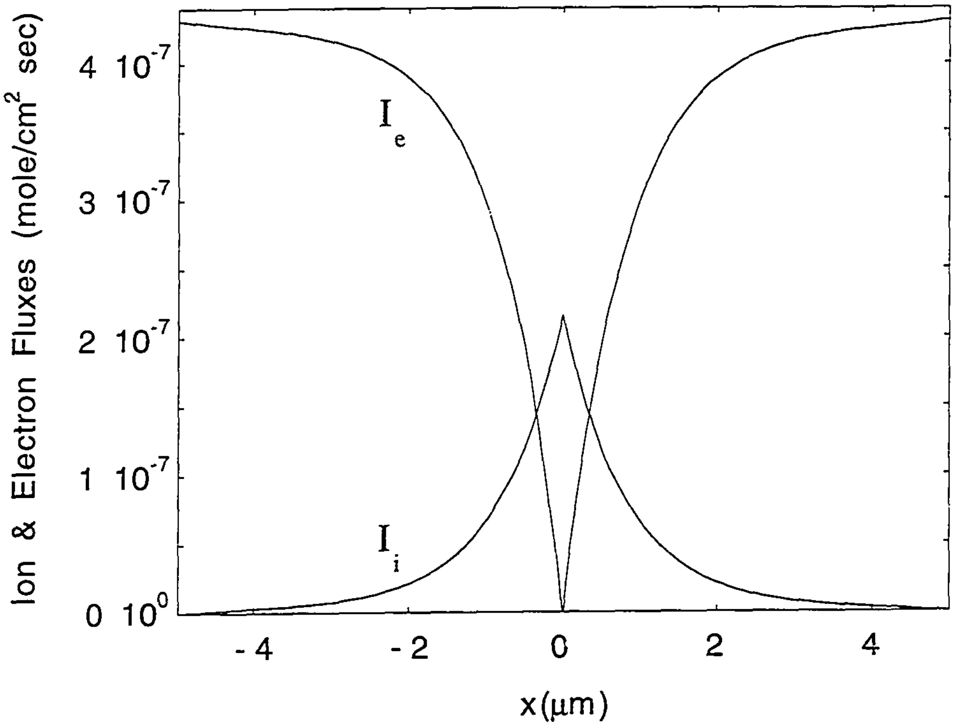
Ion & Electron Fluxes (mole/cm^2 sec)
4 10^{-7}
3 10^{-7}
2 10^{-7}
1 10^{-7}
0 10^0
I_e
I_i
-4
-2
0
2
4
x(μm)

Figure 17

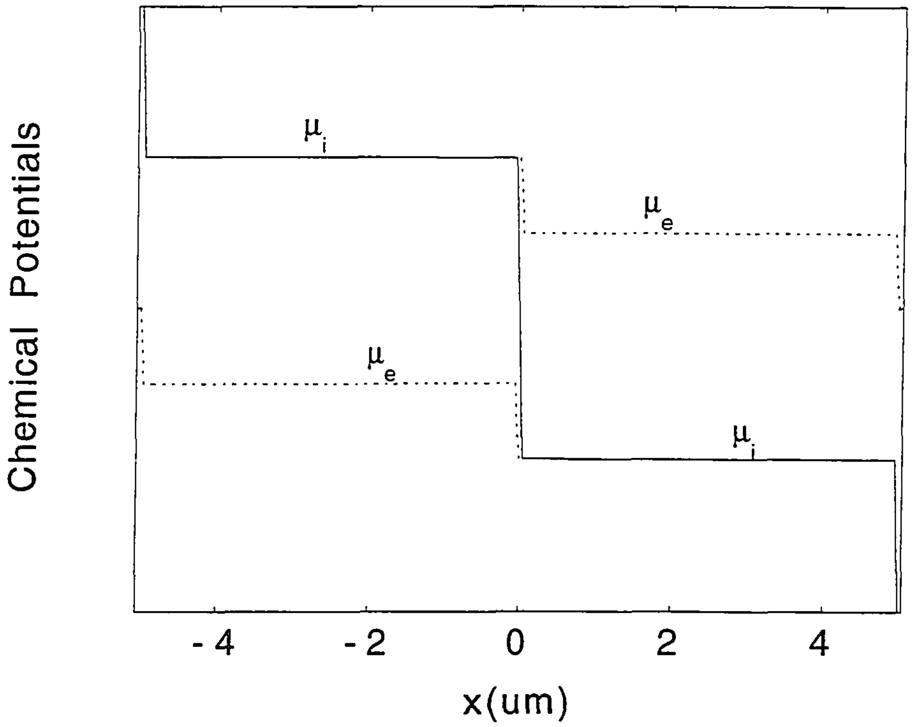

Figure 18

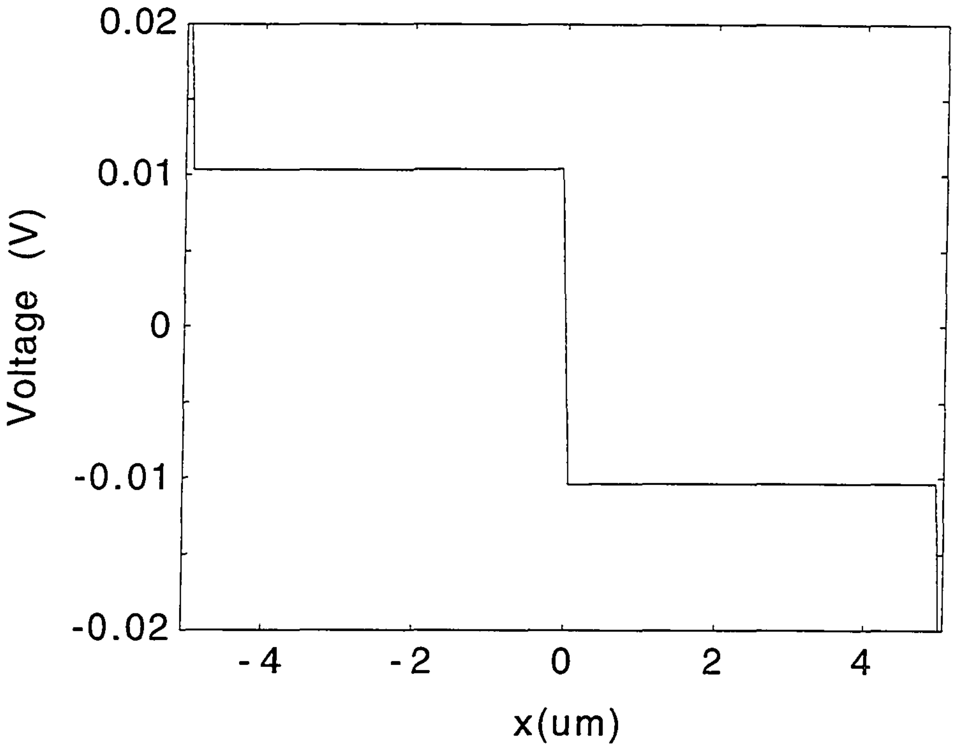

Figure 19

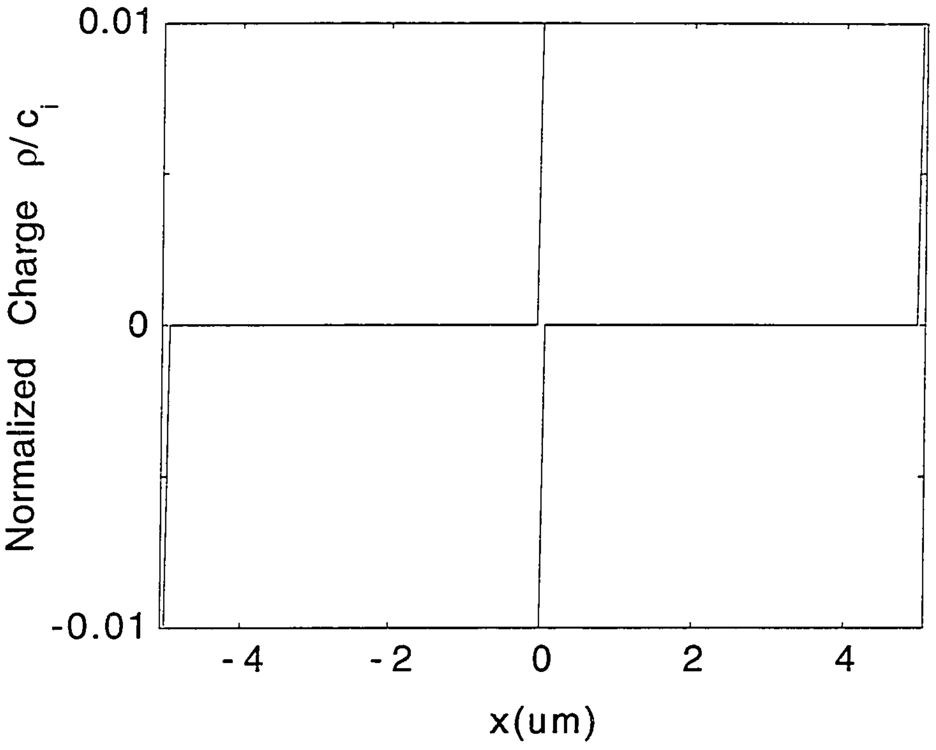

Figure 20

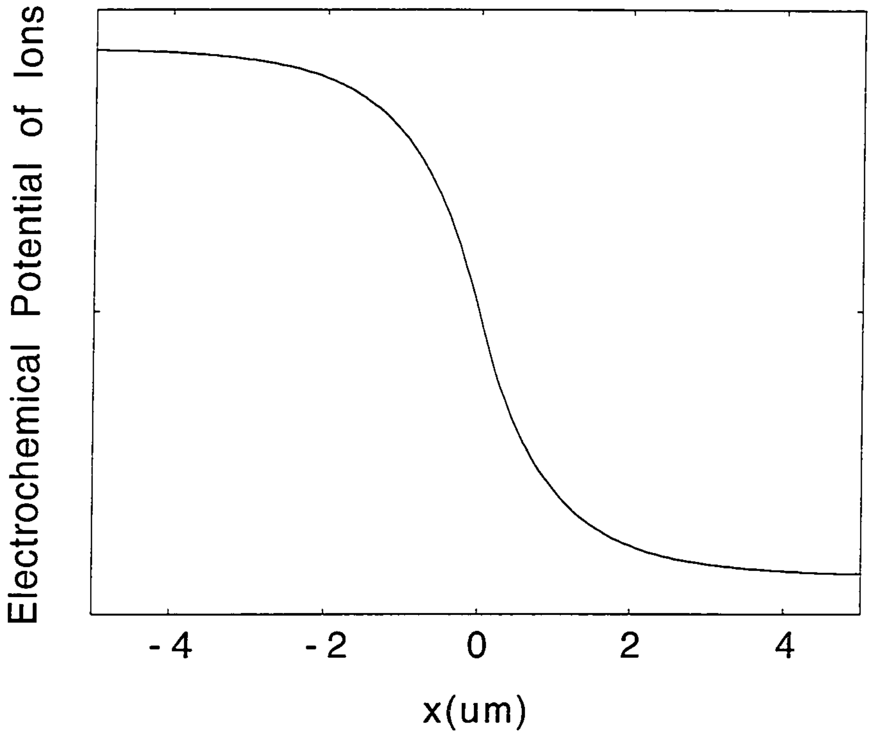

Figure 21

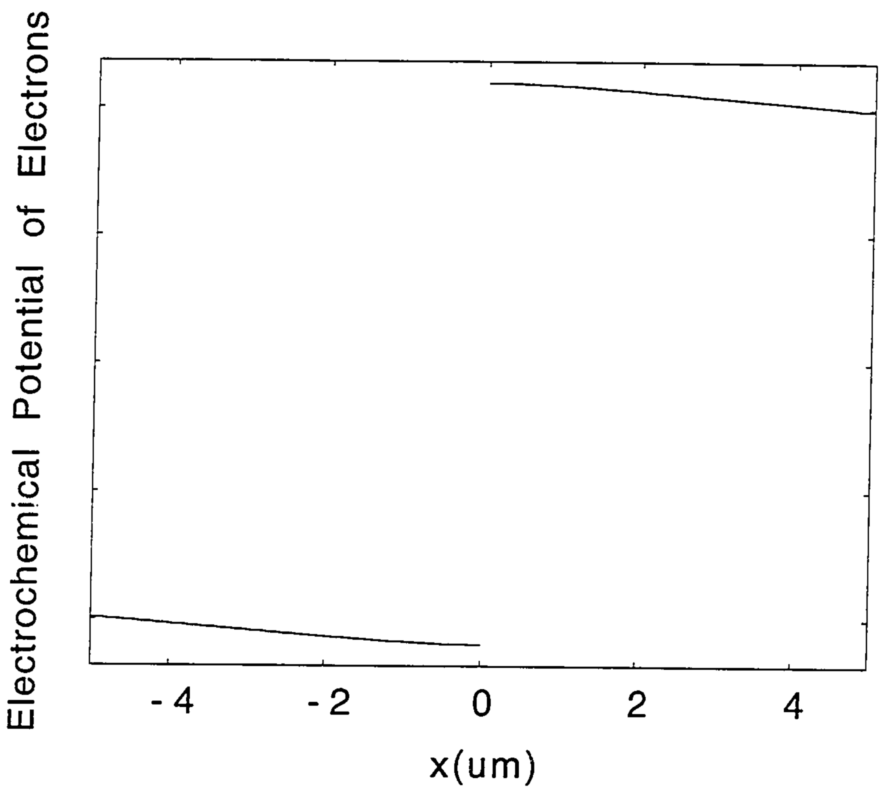

Figure 22

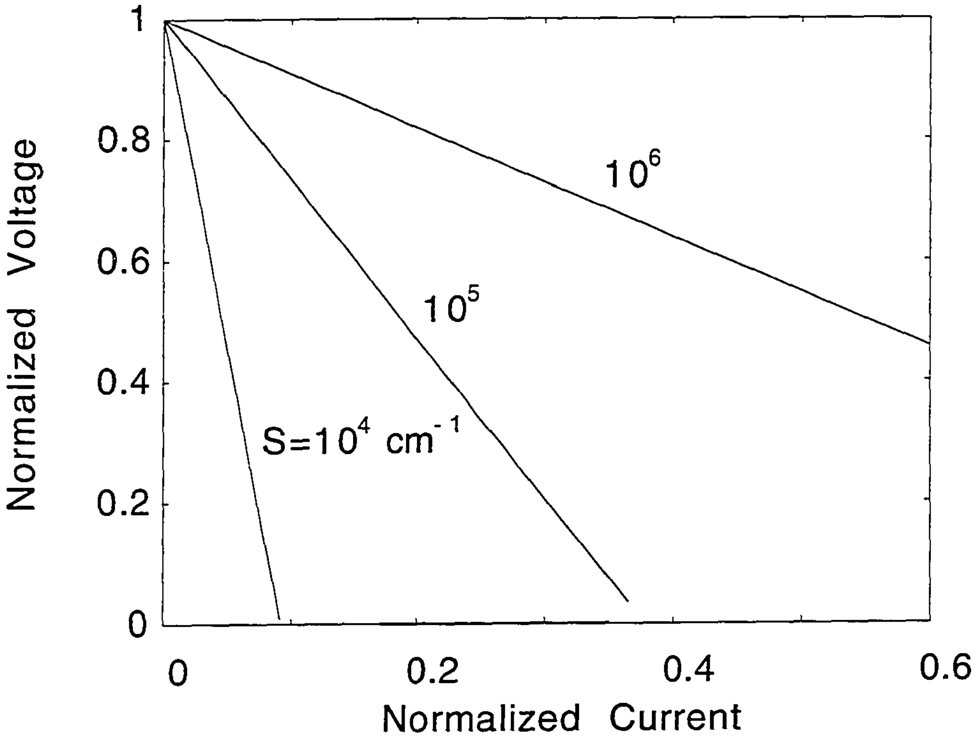
1
0.8
0.6
0.4
0.2
0
Normalized Voltage
0
0.2
0.4
0.6
Normalized Current
10^6
10^5
S=10^4 cm^{-1}

Figure 23

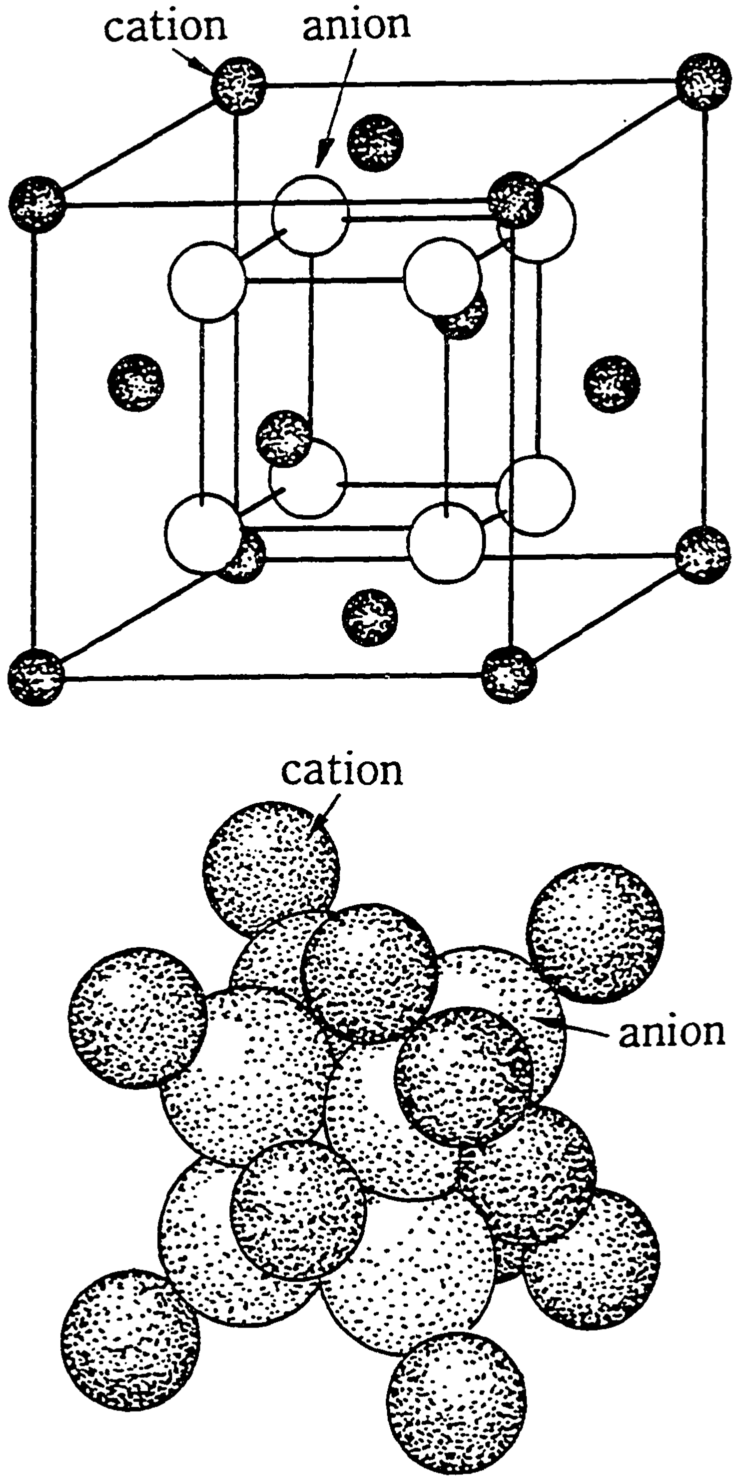

Figure 24

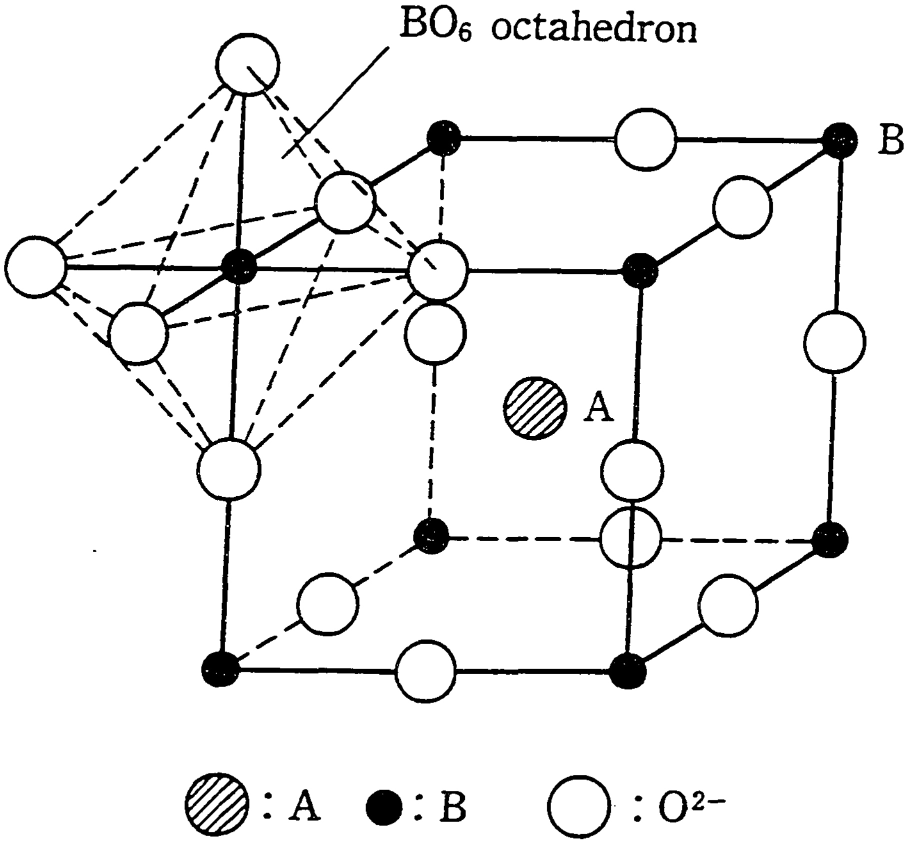

Figure 25

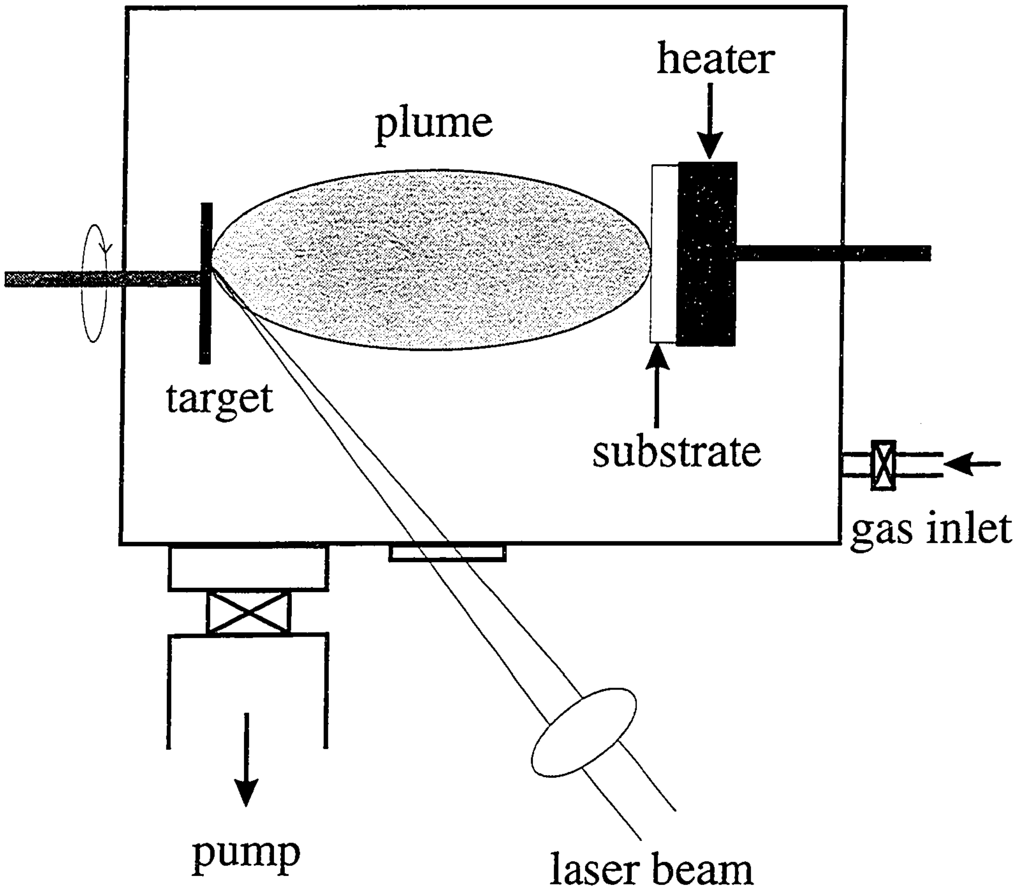

Figure 26

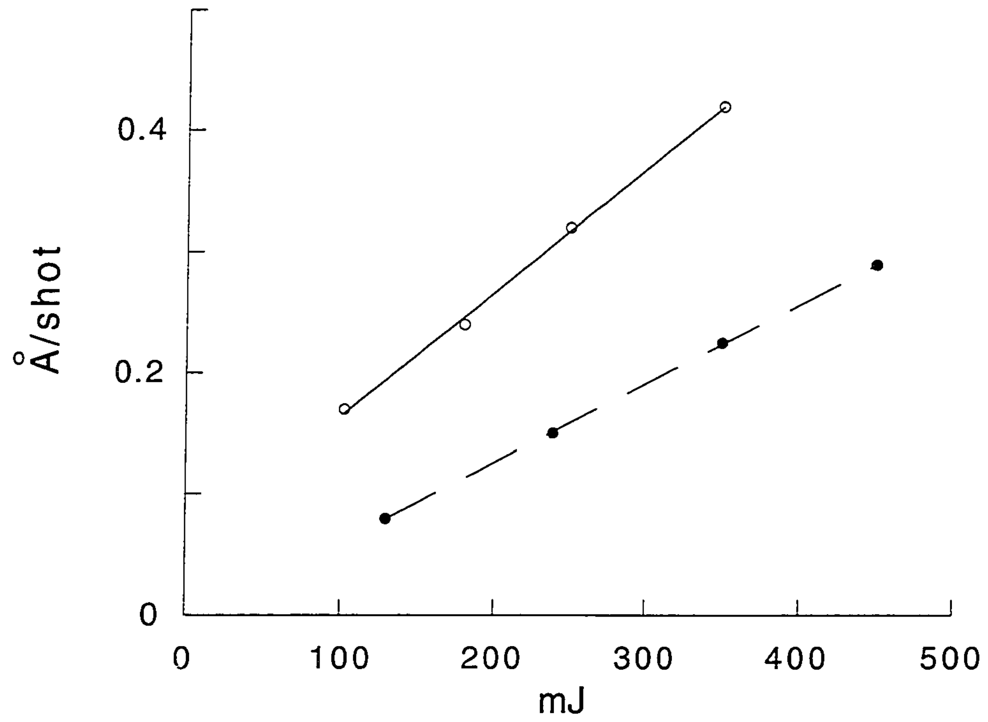

Figure 27

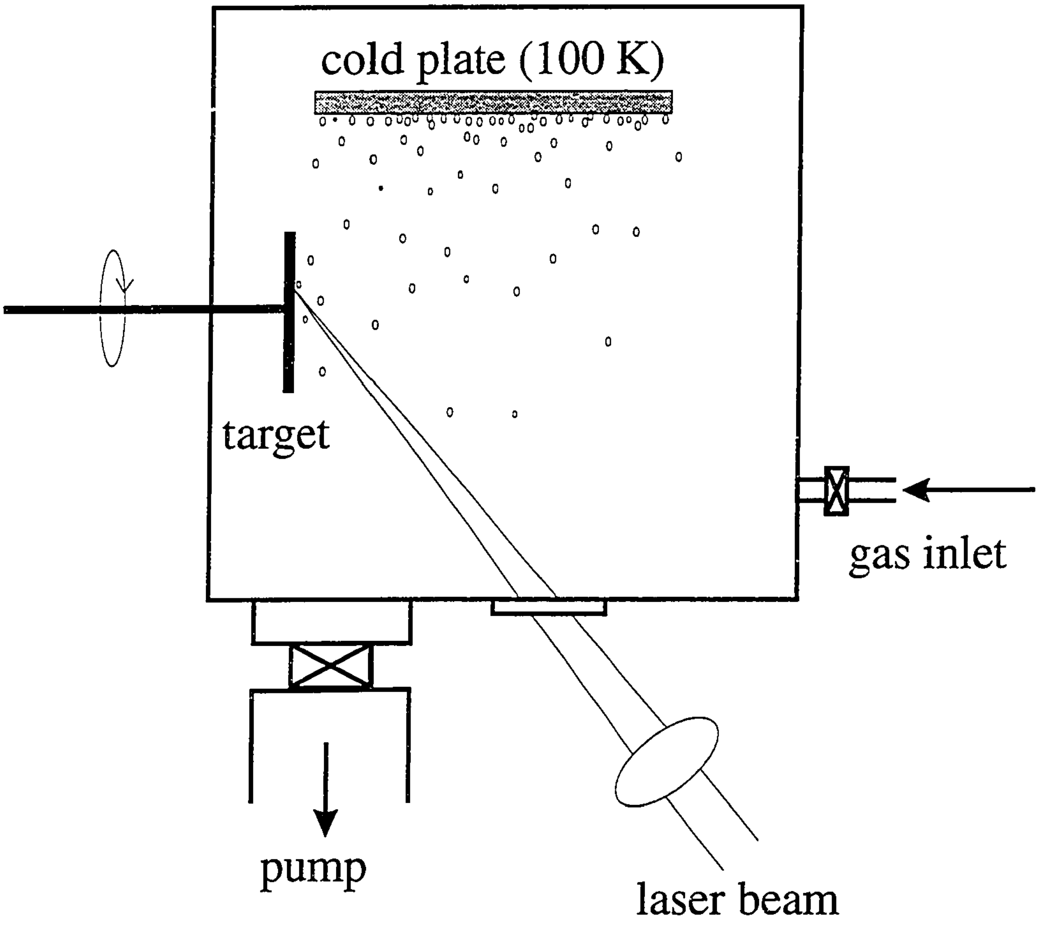

Figure 28

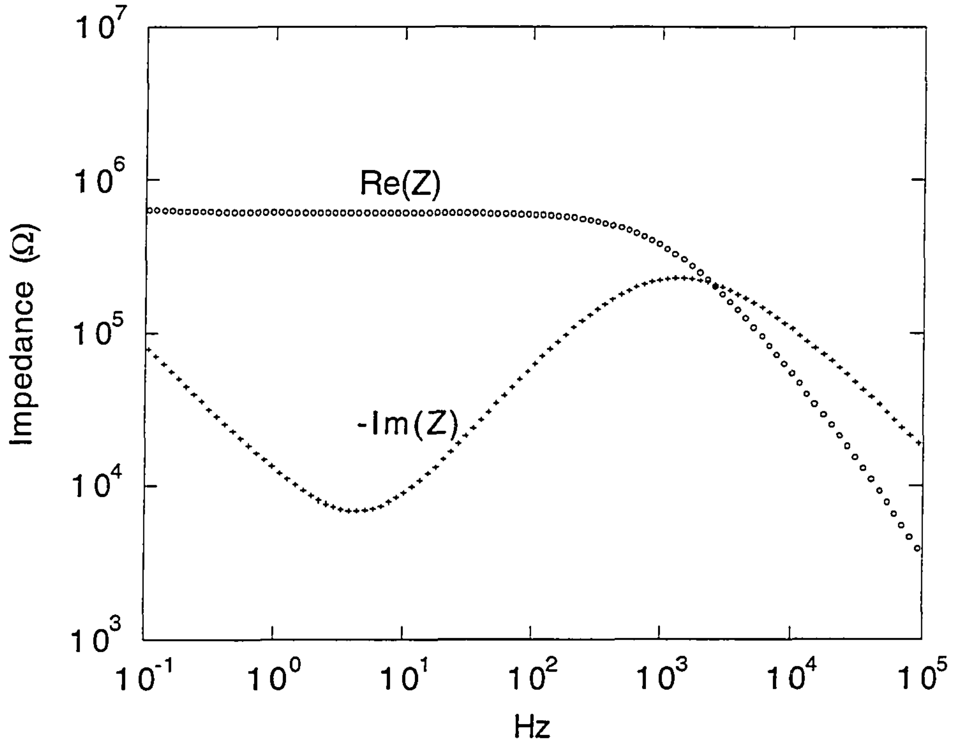
Impedance (Ω)
10^7
10^6
10^5
10^4
10^3
Re(Z)
-Im(Z)
10^{-1}
10^0
10^1
10^2
10^3
10^4
10^5
Hz

Figure 29

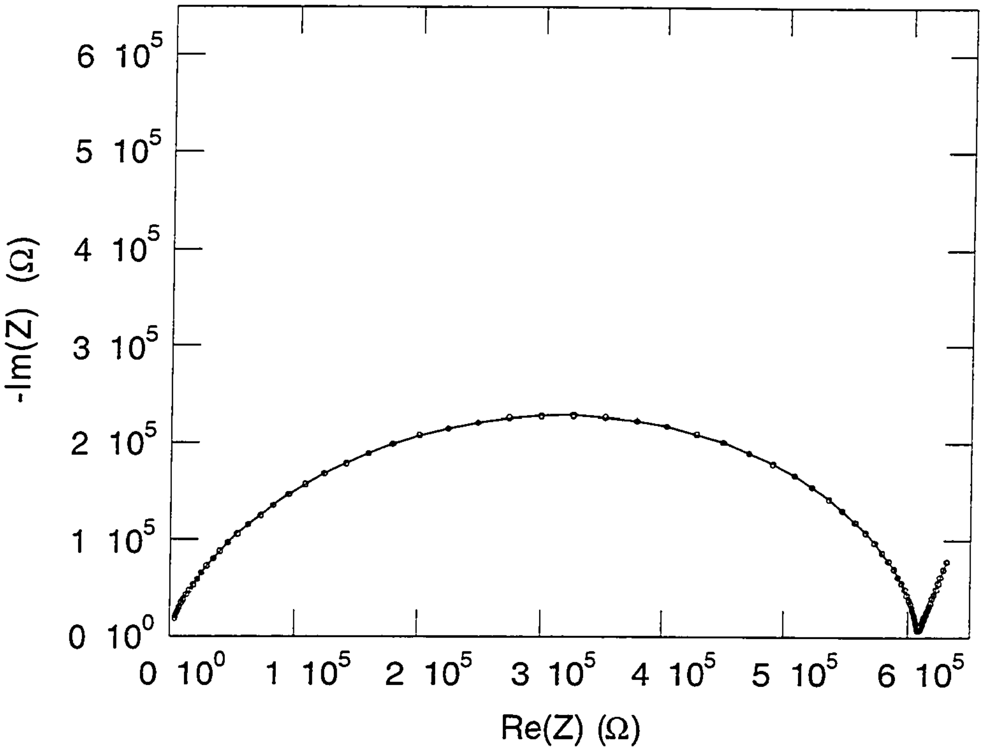
-Im(Z) (Ω)
6 10^5
5 10^5
4 10^5
3 10^5
2 10^5
1 10^5
0 10^0
0 10^0
1 10^5
2 10^5
3 10^5
4 10^5
5 10^5
6 10^5
Re(Z) (Ω)

Figure 30

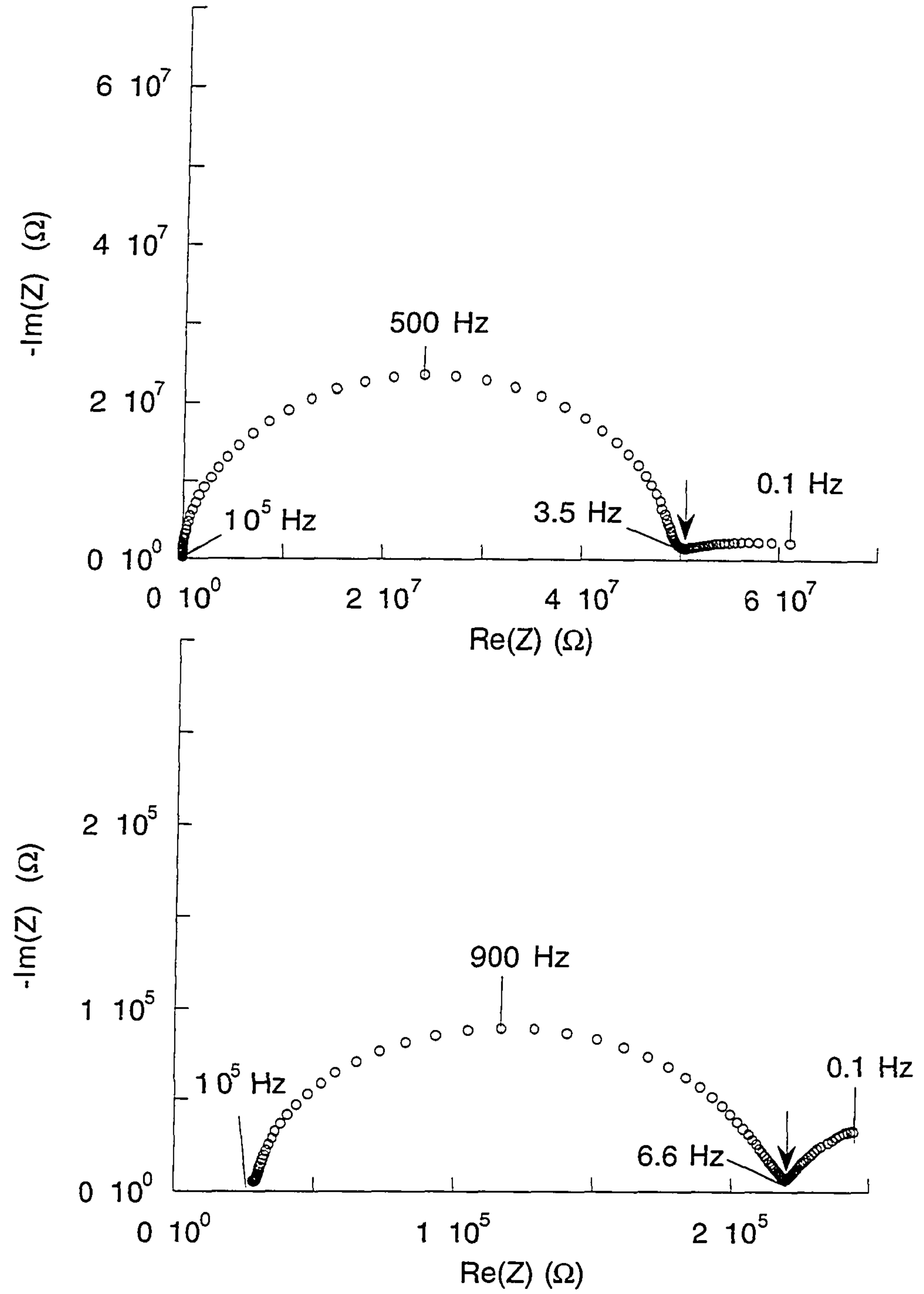
-Im(Z) (Ω)
6 10^7
4 10^7
2 10^7
0 10^0
500 Hz
10^5 Hz
3.5 Hz
0.1 Hz
0 10^0
2 10^7
4 10^7
6 10^7
Re(Z) (Ω)
-Im(Z) (Ω)
2 10^5
1 10^5
0 10^0
900 Hz
10^5 Hz
6.6 Hz
0.1 Hz
0 10^0
1 10^5
2 10^5
Re(Z) (Ω)

Figure 31

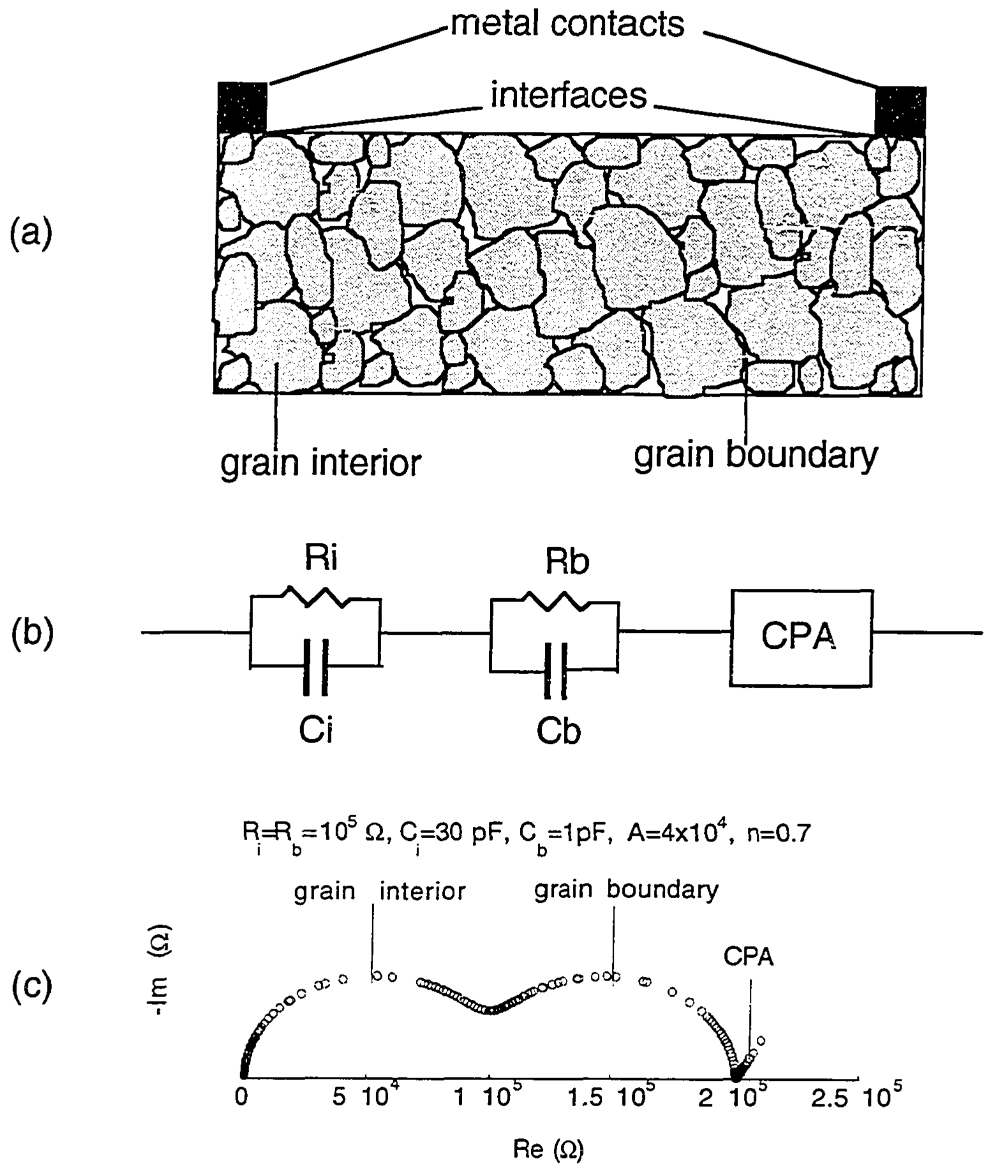
(a)
metal contacts
interfaces
grain interior
grain boundary
(b)
Ri
Rb
CPA
Ci
Cb
(c)
R_i=R_b=10^5 Ω, C_i=30 pF, C_b=1pF, A=4x10^4, n=0.7
grain interior
grain boundary
CPA
-Im (Ω)
Re (Ω)
0
5 10^4
1 10^5
1.5 10^5
2 10^5
2.5 10^5

Figure 32

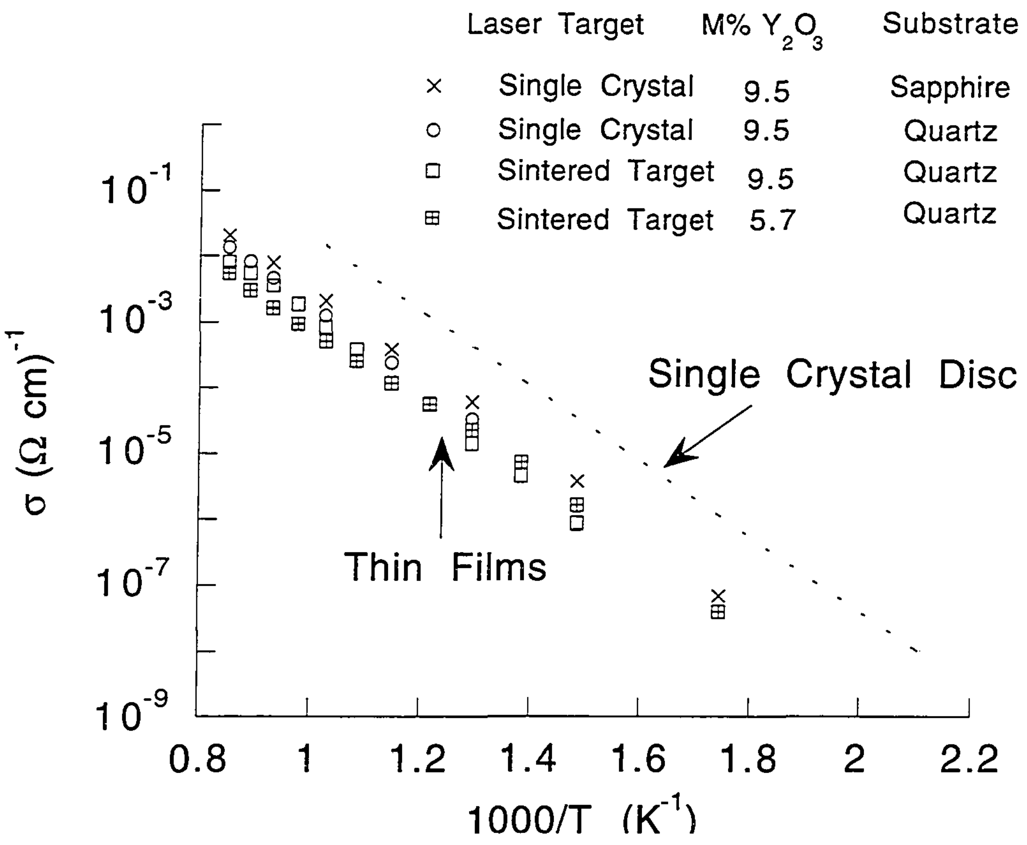
Laser Target
M% Y_2O_3
Substrate
× Single Crystal 9.5 Sapphire
○ Single Crystal 9.5 Quartz
□ Sintered Target 9.5 Quartz
⊞ Sintered Target 5.7 Quartz
Single Crystal Disc
Thin Films
$\sigma\ (\Omega\ \mathrm{cm})^{-1}$
10^{-1}
10^{-3}
10^{-5}
10^{-7}
10^{-9}
0.8
1
1.2
1.4
1.6
1.8
2
2.2
1000/T (K^{-1})

Figure 33

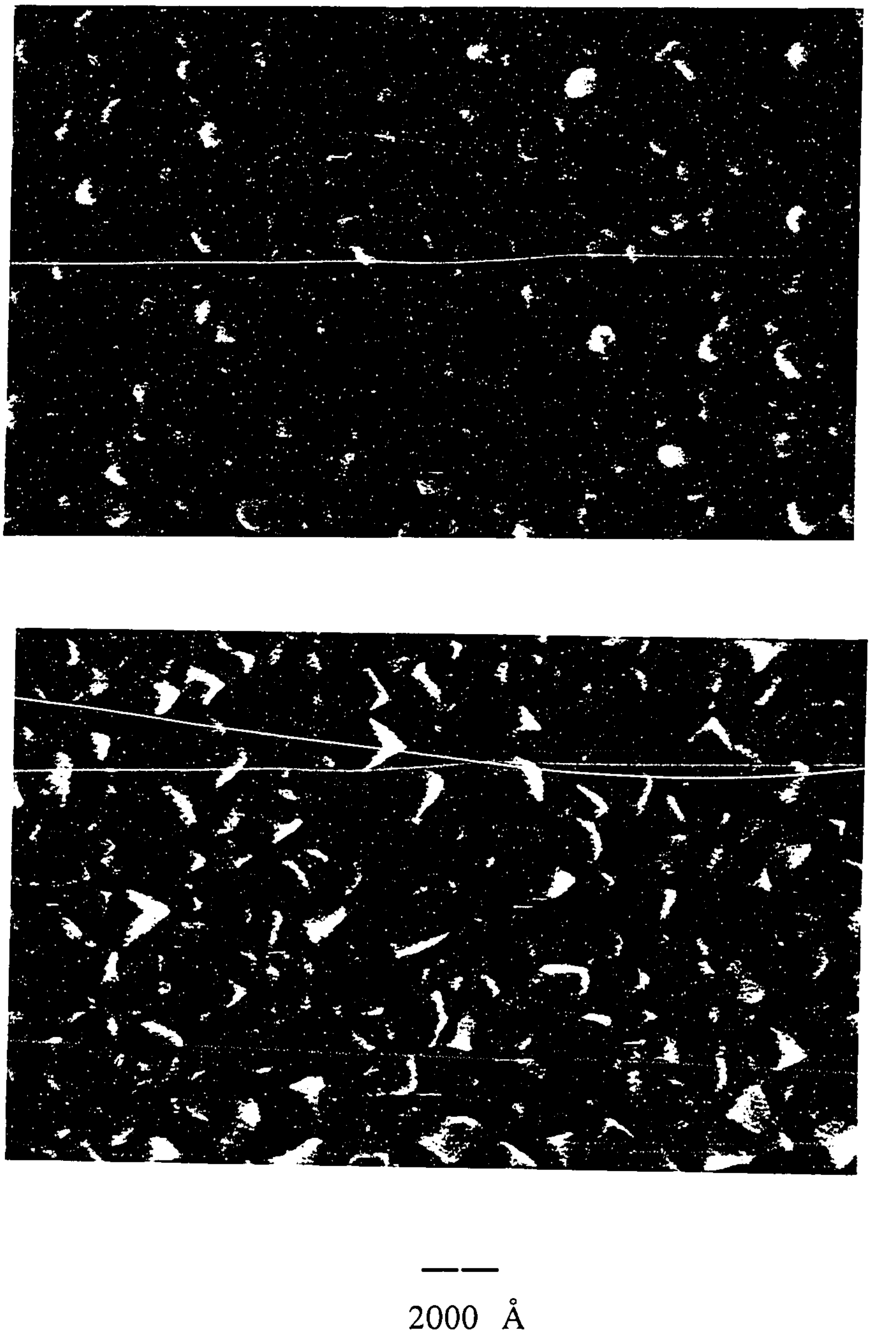

Figure 34

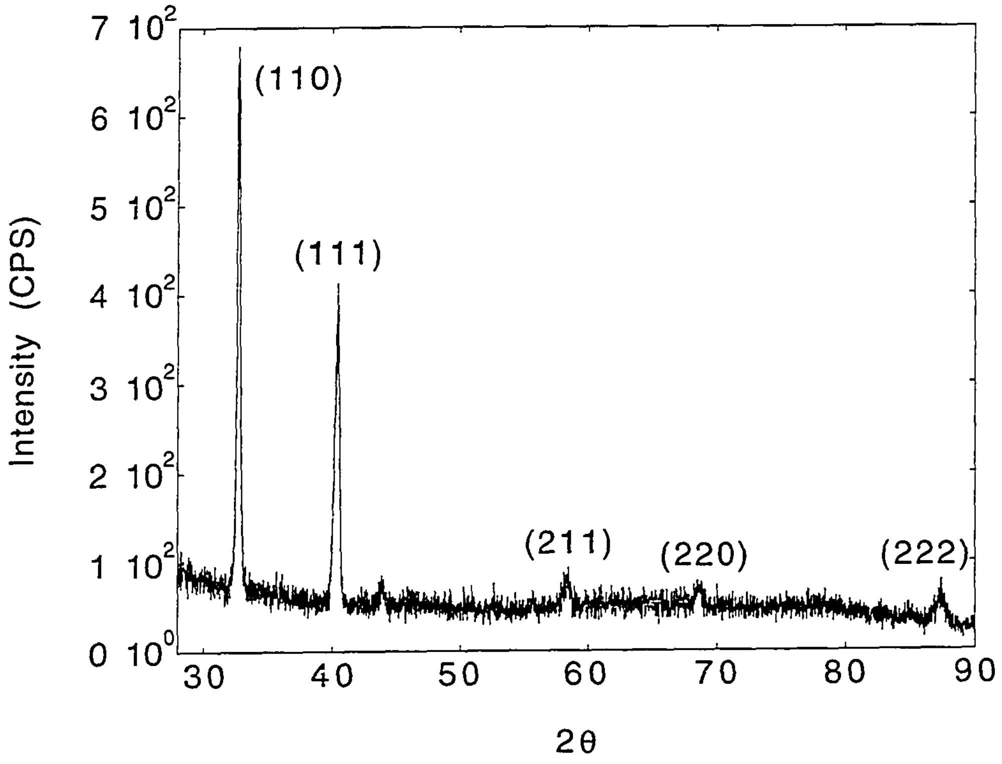
Intensity (CPS)
7 10^2
6 10^2
5 10^2
4 10^2
3 10^2
2 10^2
1 10^2
0 10^0
(110)
(111)
(211)
(220)
(222)
30
40
50
60
70
80
90
2θ

Figure 35

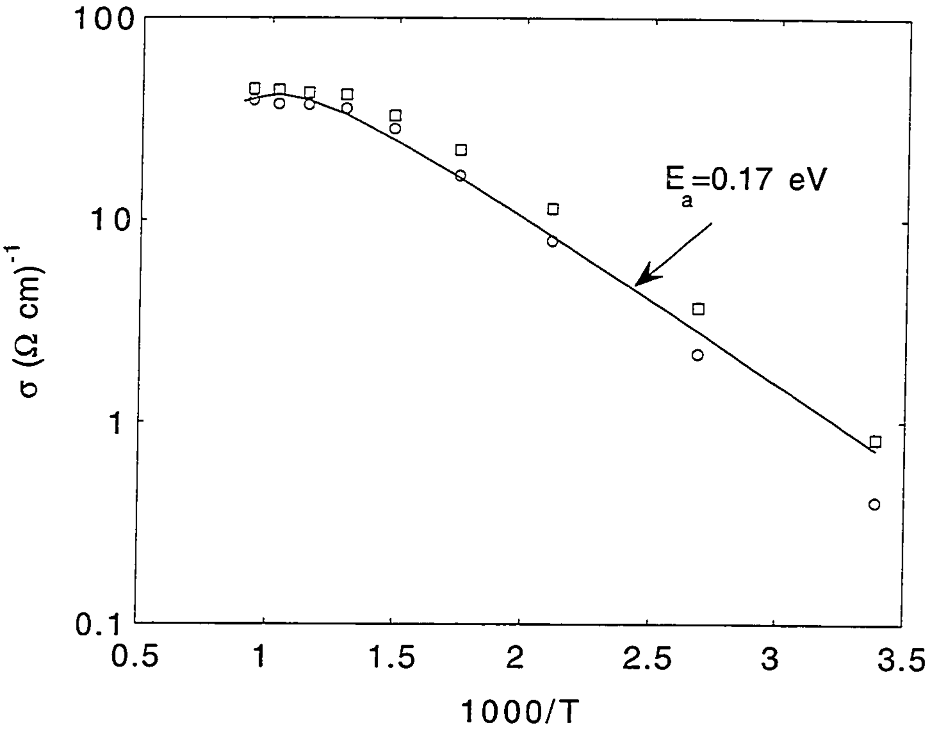
100
10
1
0.1
$\sigma\ (\Omega\ \mathrm{cm})^{-1}$
0.5
1
1.5
2
2.5
3
3.5
1000/T
E_a=0.17 eV

Figure 36

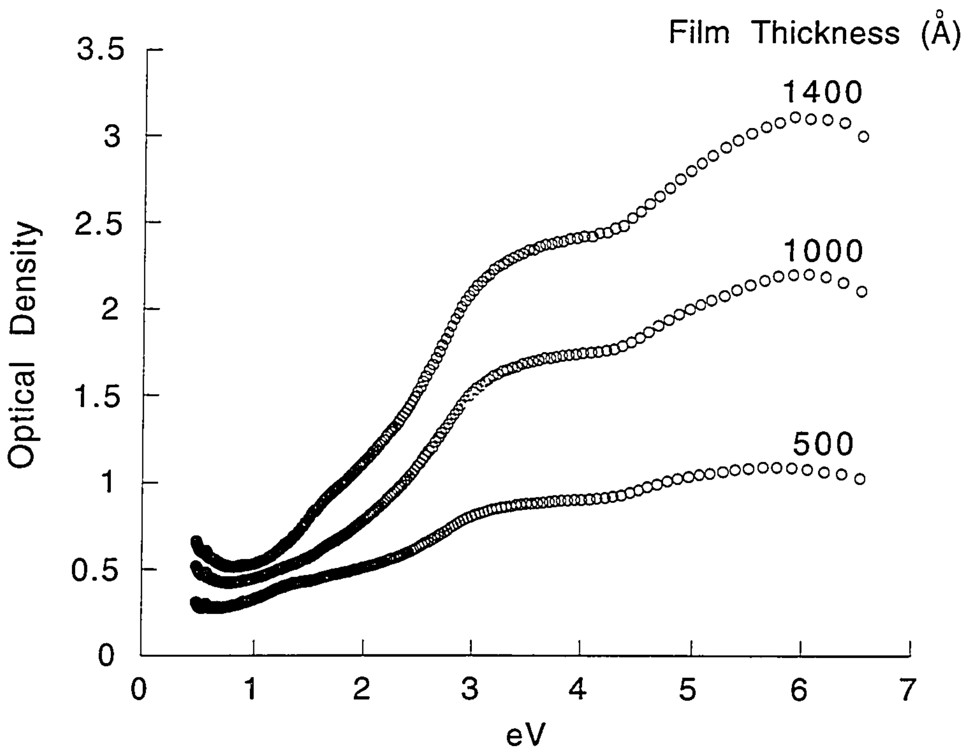
Film Thickness (Å)
1400
1000
500
Optical Density
3.5
3
2.5
2
1.5
1
0.5
0
0
1
2
3
4
5
6
7
eV

Figure 37

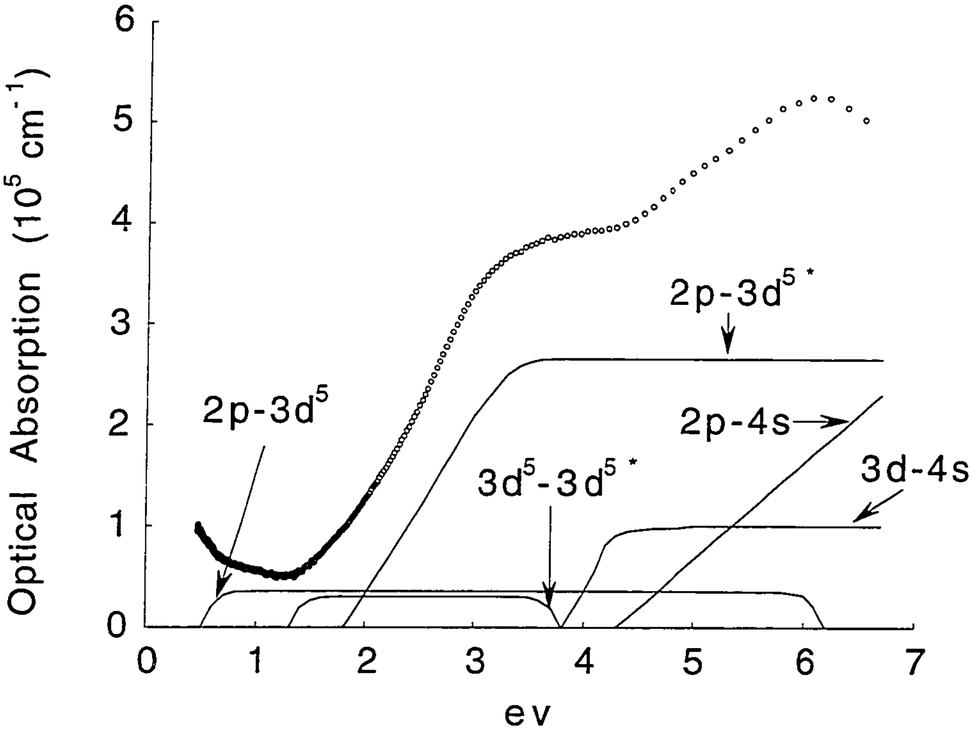
Optical Absorption (10^5 cm^{-1})
6
5
4
3
2
1
0
0
1
2
3
4
5
6
7
ev
2p-3d^5
2p-3d^{5*}
2p-4s
3d^5-3d^{5*}
3d-4s

Figure 38

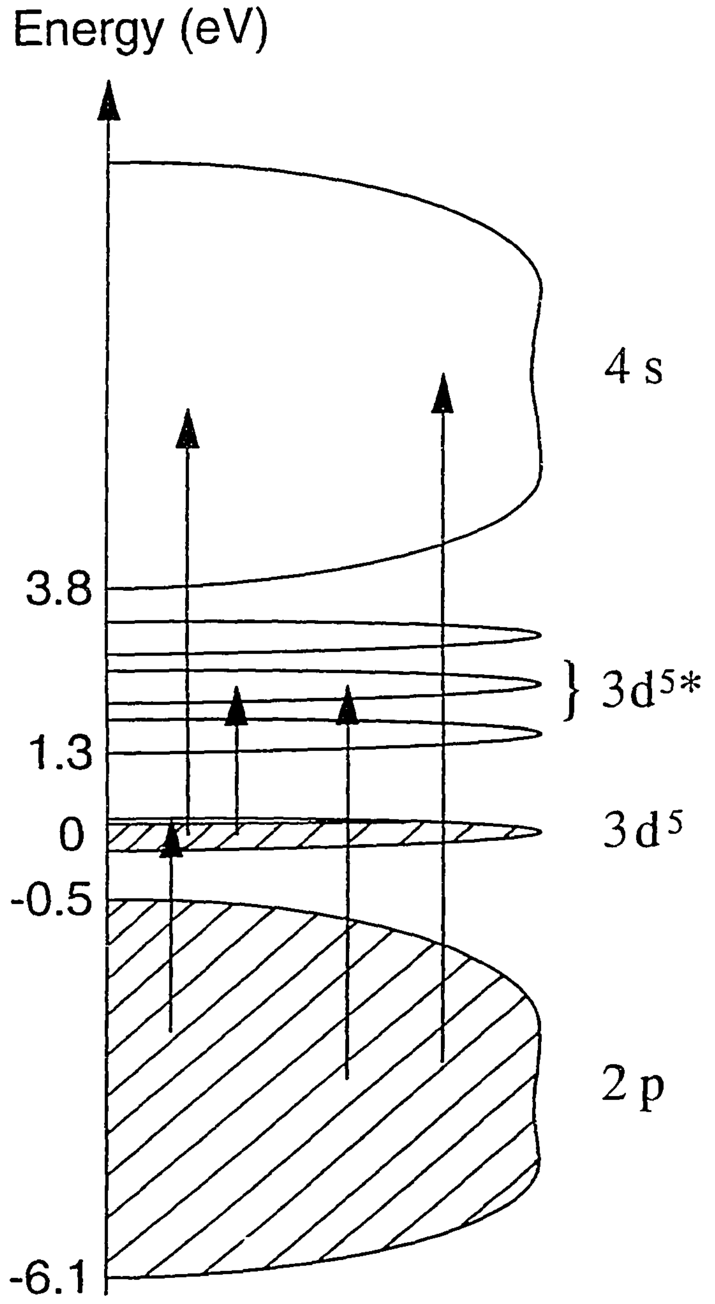

Figure 39

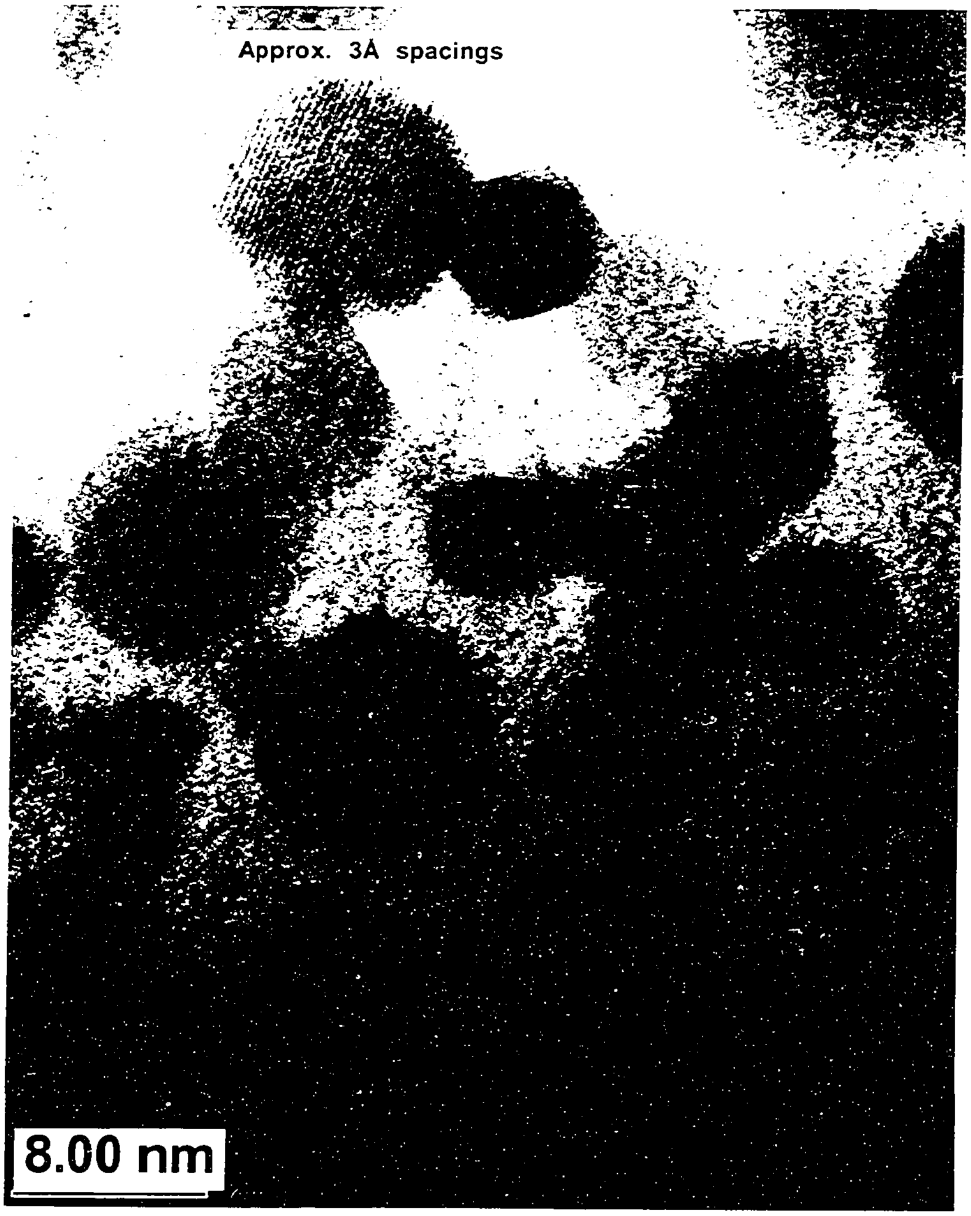

Figure 40

Figure 41

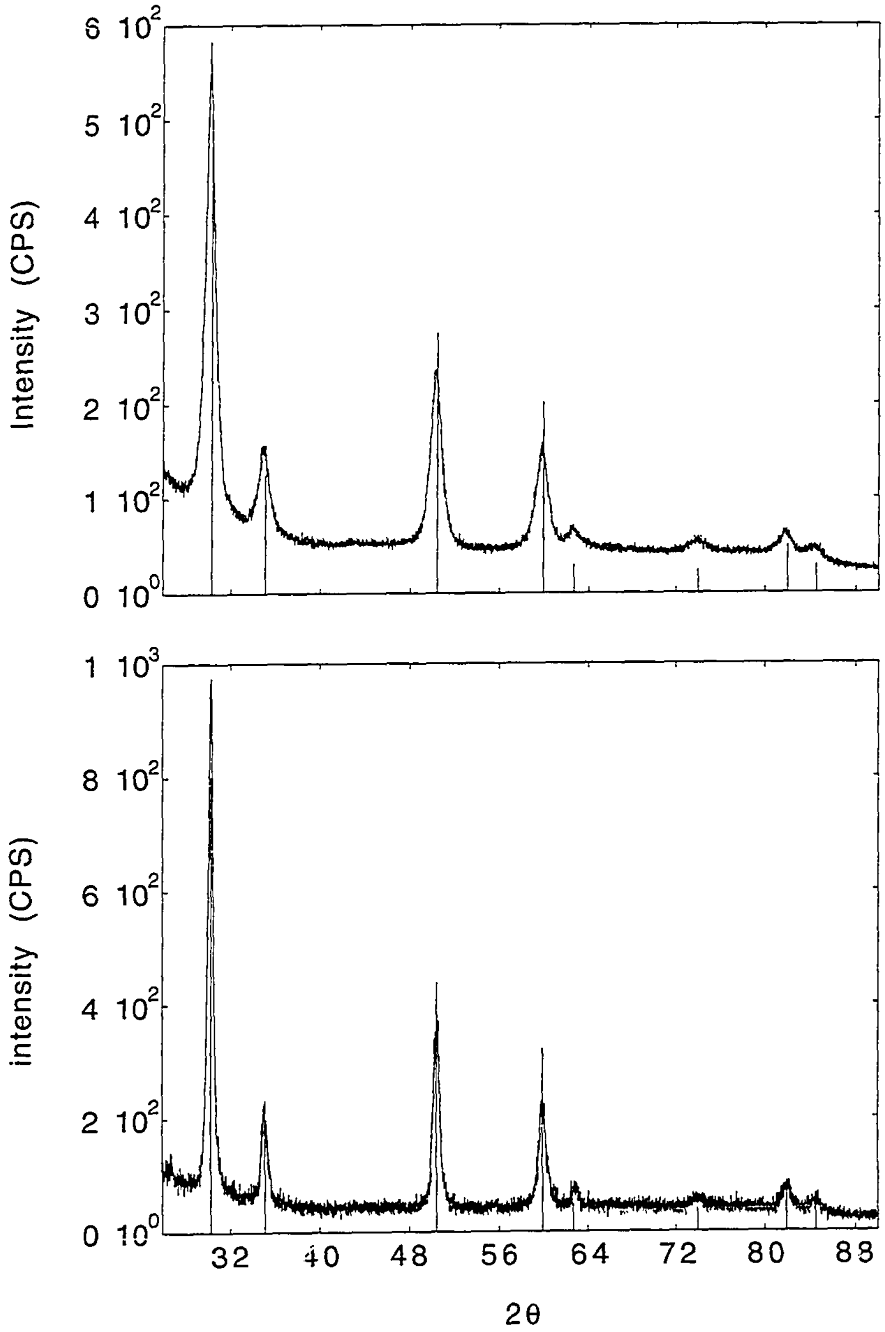
6 10^2
5 10^2
4 10^2
3 10^2
2 10^2
1 10^2
0 10^0
Intensity (CPS)
1 10^3
8 10^2
6 10^2
4 10^2
2 10^2
0 10^0
intensity (CPS)
32
40
48
56
64
72
80
88
2θ

Figure 42

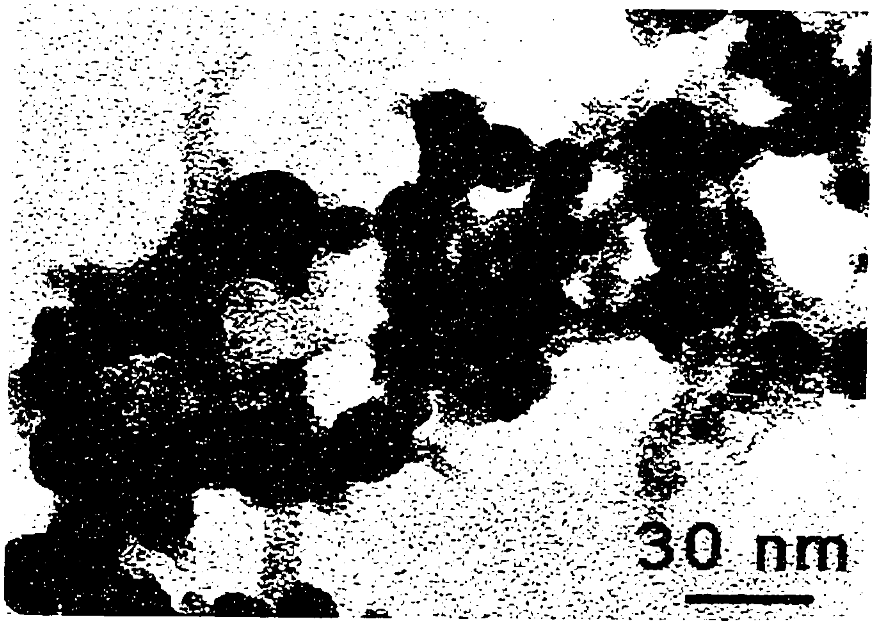

Figure 43

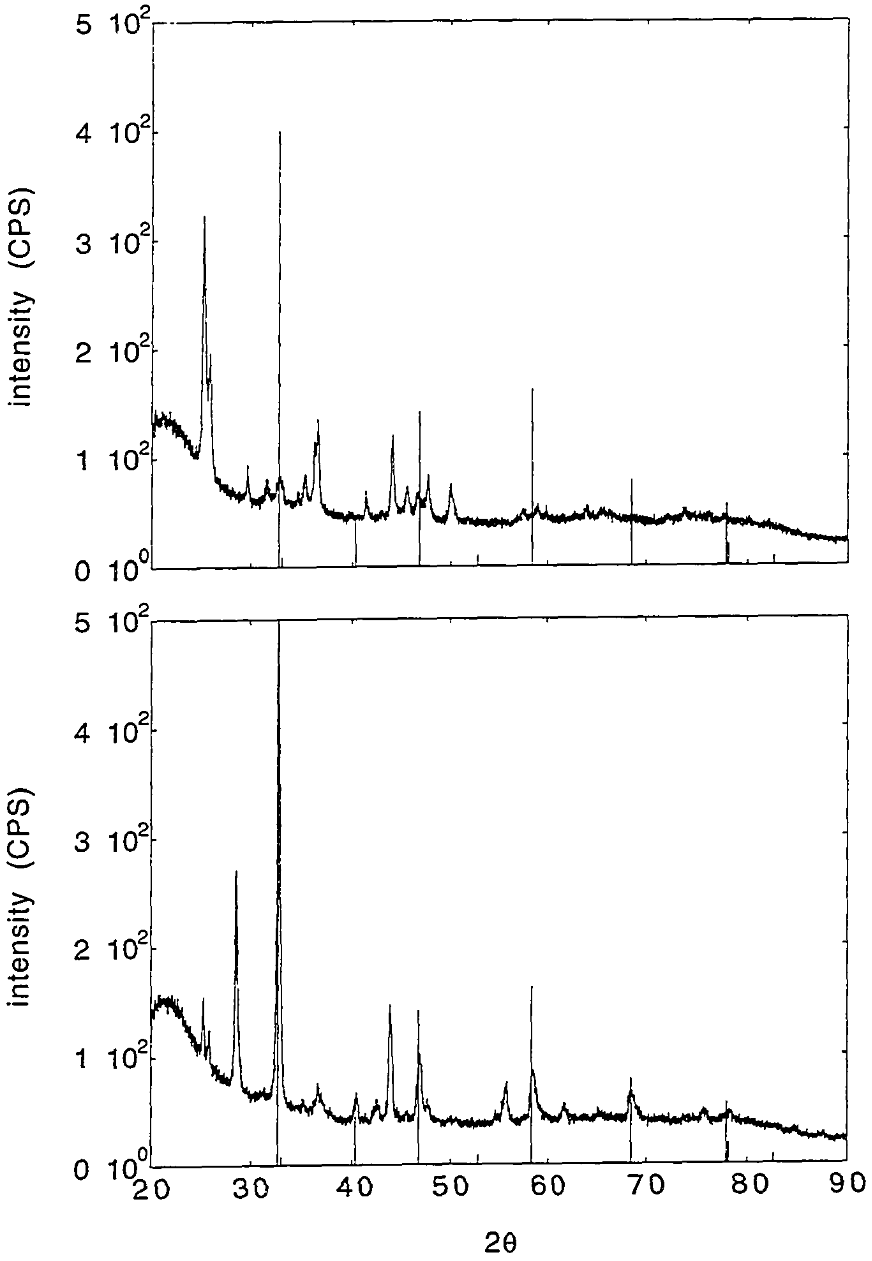
intensity (CPS)
5 10^2
4 10^2
3 10^2
2 10^2
1 10^2
0 10^0
intensity (CPS)
5 10^2
4 10^2
3 10^2
2 10^2
1 10^2
0 10^0
20
30
40
50
60
70
80
90
2θ

Figure 44

REFERENCES

[1] A. J. Burggraaf, H. J. M. Bouwmeester, B. A. Boukamp, R. J. R. Uhlhorn and V. Zaspalis, Science of Ceramic Interfaces, Elsevier Science Publishing Co., New York, 525 (1991)

[2] S. Geller, Solid Electrolytes, Springer-Verlag, New York, (1977)

[3] G. Saracco and V. Specchia, Catalysis Reviews Science and Engineering, **36**, 305 (1994)

[4] e.g. P. Kofstad, Nonstoichiometry, Diffusion and Conductivity in Binary Metal Oxides, John Wiley & Sons, New York, 101 (1972)

[5] S. Carter, A. Selcuk, R. J. Chater, J. Kajda, J. A. Kilner, B. C. H. Steele, Solid State Ionics, **53-56**, 597 (1992)

[6] H. J. M. Bouwmeester, H. Kruidhof and A. J. Burggraff, Solid State Ionics, **72**, 185 (1994)

[7] J. Giner and C. Hunter, J. Electrochem Soc., **116**, 1124 (1969)

[8] W. Vogel, J. Lundquist, P. Ross, and P. Stoneheart Electrochimica Acta, **20**, 79 (1975)

[9] R. Jackson, Transport in Porous Catalysts, Elsevier Scientific Publishing Co., New York, (1977)

[10] M. Zhou and P. Sheng, Phys. Rev. B, **39**, 12027 (1989)

[11] S. Kostek, L. M. Schwartz and D. L. Johnson, Phys. Rev. B, **45**, 186 (1992)

[12] W. van Roosbroeck, Phys. Rev., **91**, 282 (1953)

[13] T. Kudo and K. Fueki, Solid State Ionics, Kodansha Ltd., New York, (1990)

[14] C. Berger, Handbook of Fuel Cell Technology, Prentice-Hall INC., Englewood Cliffs, New Jersey, (1968)

[15] C. E. Pax, Fuel Cell, Fuel Cell Seminar, Tucson, Arizona, Nov.29-Dec.2 (1992)

[16] Y. Teraoka, H. M. Zhang, K. Okamoto and N. Yamazoe, Mat. Res. Bull., **23**, 51 (1988)

[17] L. M. Liu, T. H. Lee, L. Qiu, Y. L. Yang and A. J. Jacobson, will be published in Mat. Res. Bull., (1995)

[18] Y. Teraoka and H. M. Zhang, Chem. Lett., 1743 (1985)

[19] H. Kruidhof, H. J. M. Bouwmeester, R. H. E. v. Doorn and A. J. Burggraaf, Solid State Ionics, **63-65**, 816 (1993)

[20] D. C. Paine and J. C. Bravman, Materials Research Society, Symp. Proc., Pittsburgh, **191** (1990)

[21] D. B. Chrisey and G. K. Hubler, Pulsed Laser Deposition of Thin Films, John Wiley & Sons, New York, (1994)

[22] A. Q. Pham and A. J. Jacobson, Proceedings of MRS, Boston, Nov.28-Dec.2, 1994.

[23] H. Gleiter, Progress in Materials Science, **33**, 223 (1990)

[24] R. W. Siegel, Encyclopedia of Applied Physica, **11**, 173 (1994)

[25] A. K. Jonscher, J. Material Science, **13**, 553(1978)

[26] C. J. F. Bottcher and P. Bordewijk, Theory of dielectric polarization, **1 & 2**, Elsevier Scientific Publishing Co., New York, (1978)

[27] N. Yamazoe and Y. Teraoka, Catalysis Today, **8**, 175 (1990)

[28] R. C. Weast and M. J. Astle, CRC Handbook of Chem. & Phys., CRC Press, Inc., Boca Raton, Florida, E-69 (1981)

[29] J. B. Torrance, P. Lacorro, C. Asavaroengchai and R. M. Metzger, J. of Solid State Chemistry, **90**, 168 (1991)

[30] J. B. Goodenough, Magnetism and the Chemical Bond, Interscience, New York (1963)

[31] A. P. Bradford, G. Hass and M. McFarland, Applied Optics, **11**, 2242 (1972)